

2022

Journal of
JART
—English edition—

2022



The Japan Association of Radiological Technologists

CONTENTS

- 2 Overview of the Japan Association of Radiological Technologists/general principles
- Foreword**
- 3 Regarding Publication of the English Edition
UEDA Katsuhiko, President, The Japan Association of Radiological Technologists
- History**
- 4 History of The Japan Association of Radiological Technologists (JART)
- Arts and Sciences**
- 6 **original articles**
Radiological assessment of joint space width using different weight-bearing radiographic methods for knee osteoarthritis
YAMAGUCHI Masanori, KOSEKI Hironobu, ENGUCHI Kousei, IWANAGA Hitoshi, KYUMA Shunta, SHINDO Hiroyuki
- 13 **original articles**
New simple imaging method for short-axis view in cardiac MRI inferred from chest X-ray
FUJII Tomoki, USUI Hiromi, SATO Hisaya, KATO Kyoichi
- 25 **original articles**
Calculation of optimal TI associated with temperature changes of the water using Synthetic MRI assuming postmortem brain FLAIR imaging
OKAWA Ryuya, YASUI Go, KANAI Yoshihiro, MIHARA Ban, HAYASHI Norio
- 33 **original articles**
Trial of dose reduction of Digital Breast Tomosynthesis
HAYAKAWA Saki, SHINOHARA Norimitsu
- 40 **original articles**
Modification methods of radiographic conditions alternative to tube voltage coefficient chart
HATAKEYAMA Norihito
- 47 **material**
New challenges for SARS-CoV-2 -Infection control in Mobile X-ray-
MOCHIGI Kazuya, SHINAGAWA Kazuki
- 58 **material**
Portable chest X-ray examination procedures for COVID-19-positive patients: performance time necessary for radiological technologists
KOBAYASHI Tomoya, ISHIBASHI Tomomichi, SOMEYA Satoka, TASHIRO Kazuya, ITO Yoshiyuki, MIYAMOTO Katsumi, YOKOKAWA Hiroshi, SHIGAI Masanari, SHIOTANI Seiji
- 66 Regulations and Requirements for Submissions to the Journal of the Japan Association of Radiological Technologists

Overview of the Japan Association of Radiological Technologists

The Japan Association of Radiological Technologists, a public interest incorporated association under the jurisdiction of the Ministry of Health, Labour and Welfare, was established in 1947 with the purpose of contributing to the health of citizens through raising the professional ethics of members, improving and furthering the study of medical radiology and medical radiological technology, and enhancing public health.

In light of the startling progress being made in the fields of image diagnostics and radiation therapy where radiological technologists work, it is necessary to stay constantly aware of the latest know-how and technology. JART collaborates with other certification agencies to enhance the capacity of all radiological technologists in general through providing lifelong learning seminars, short courses, academic conferences and numerous other learning opportunities. We believe that such activities constitute our obligation as medical professionals to the general public.

As the only medical profession that has “radiological” in its name, we strive to limit medical exposure, to raise the standing of our profession, and to realize a profession of specialist technologists that can be advertised. And we are committed to promoting services with you all for the provision of safe and secure medical care.

general principles

We will render our services to those in need of health care.

We will act as individual members of a health care team.

We will perform our duties in our field of specialty.

We will continue to study for the benefit of mankind.

We will respect and practice the policy of informed consent.



Regarding Publication of the English Edition

UEDA Katsuhiko (President)



The journal of the JART English version issues every year. It has a favorable reception for we members of the world and general people. As well as this issue, 7 articles to be useful for radiological technologists are issued.

We will feature clinical, educational, and research-based achievements by radiological technologists in the monthly issues of the JART journal, and continually work to improve the magazine. I truly hope that this English edition will benefit radiological technicians worldwide.

To give our radiological technologists from across the globe an insight into our business, I will briefly explain the history of the JART. In March 1896, we succeeded in taking the first X-ray image in Japan. In 1897, Shimadzu Corporation released an X-ray generator for educational use. In 1925, there were approximately 1,500 X-ray technicians. In 1927, the first Shimadzu X-ray Technician Training Institute was established, and evidence-based education was put in place. The JART was founded in 1947 to make “radiological technologist” a national qualification. Since its establishment, we have worked towards broad acceptance of this national qualification, in collaboration with the government, the Diet, the Japanese Medical Association, and occupational military authorities.

As a result in June 1951, we were finally able to see the promulgation of the Radiology X-ray Technicians Act, Act No.226 of 1951. Since then, we have responded to the changing needs of the society, revising the original act to get the Radiology X-ray Technicians Act of 1968 passed, and partially revising that to get the Radiology Technicians Act and Radiology X-ray Technicians Act of 1983 passed, and finally getting the Radiology Technicians Act, which is in place currently, passed. Back then, the scope of work was limited to general X-ray testing, television X-ray testing, angiography, X-ray computed tomography scanning, RI scanning, and radiation therapy. In 1993, the Radiology Technicians Act was further revised, and MRI scanning, ultrasonic testing, and non-mydratic fundus camera examination were added to the list. In 2010, image interpretation assistance, radiation examination explanation, and consultation work were added. In April 2015, intravenous contrast agent injection using automated contrast injectors, needle removal and hemostasis, lower digestive tract examination (anal catheter insertion and administration of contrast medium), anal catheter insertion, and oxygen inhalation during radiation therapy were added as operations that could be performed by radiological technologists.

In October 2021, the needle insertion for examinations of contrasting of the examination for CT, MRI, Ultrasound and Radioisotope are added as the new operation that can be performed by radiological technologists.

The JART will continue to respond to the needs of the medical industry, and we hope to broaden the operational scope of radiological technologists based on our foundation in scientific evidence.

History of The Japan Association of Radiological Technologists (JART)



1947

- Establishment of JART (July 13)

1951

- Promulgation of the Act on Medical Radiographers (June 11)
- Authorization for Establishment of the Japan Association of Radiographers (June 13)

1954

- First national examination for Medical Radiographers (May 30)

1956

- Event to commemorate the 10th anniversary of founding, attended by Her Imperial Highness Princess Chichibunomiya

1962

- Event to commemorate the 15th anniversary of founding and 10th anniversary of enactment of the Act on Medical Radiographers, attended by Her Imperial Highness Princess Chichibunomiya

1968

- Promulgation of the Act to Partially Revise the Act on Medical Radiographers (establishment of two professions) (May 23)
- First national examination for radiological technologists

1969

- Renaming as the JART
- Staging of the 4th International Society of Radiographers & Radiological Technologist (ISRRT) World Congress at Tokyo Palace Hotel, attended by Her Imperial Highness Princess Chichibunomiya

1975

- Event to commemorate the 80th anniversary of the discovery of X-rays, attended by Her Imperial Highness Princess Chichibunomiya

1979

- Completion of the Education Center for JART

1983

- Partial revision of the Act on Medical Radiographers and the Act on Radiological Technologists (unification of the professions)

1985

- Event to commemorate the 90th anniversary of the discovery of X-rays, attended by Her Imperial Highness Princess Chichibunomiya
- Staging of the 1st Japan Conference of Radiological Technologists

1987

- General assembly resolution for establishment of the New Education Center and a four-year university

1989

- Completion of the New Education Center (Suzuka City)

1991

- Opening of Suzuka University of Medical Science

1993

- The Act to Partially Revise the Act on Radiological Technologists, and Ministerial Ordinance to Partially Revise the Enforcement Orders (April 28)

1994

- Appointment of the President of JART as the 11th President of ISRRT

1995

- Event to commemorate the 100th anniversary of the discovery of X-ray, attended by Her Imperial Highness Prince Akishinomiya

1996

- Start of the Medical Imaging and Radiologic Systems Manager certification system

1998

- Staging of the 11th ISRRT World Congress at Makuhari

1999

- Start of the Radiation Safety Manager certification system

2000	<ul style="list-style-type: none"> • “Presentation of the Medical Exposure Guidelines (Reduction Targets)” for patients 	
2001	<ul style="list-style-type: none"> • Start of the Radiological Technologists Liability Insurance System 	
2003	<ul style="list-style-type: none"> • Enactment of X-Ray Week 	
2004	<ul style="list-style-type: none"> • Relocation of offices to the World Trade Center Building in Tokyo 	
2005	<ul style="list-style-type: none"> • Start of the Medical Imaging Information Administrator certification system 	
2006	<ul style="list-style-type: none"> • Staging of a joint academic conference between Japan, South Korea, and Taiwan • Revision of the Medical Exposure Guidelines 	
2008	<ul style="list-style-type: none"> • Establishment of the committee on Autopsy imaging (Ai) 	
2009	<ul style="list-style-type: none"> • Revision to the national examination for radiological technologists • Launch of the Team Medicine Promotion Conference, with the President of JART as its representative • Appointment of the President of JART as chairperson of the Central Social Insurance Medical Council specialist committee 	
2010	<ul style="list-style-type: none"> • Health Policy Bureau Director’s notification concerning promotion of team medicine 	
2011	<ul style="list-style-type: none"> • Support activities following the Great East Japan Earthquake • Staging of an extraordinary general meeting concerning transition to a public interest incorporated association 	
2012	<ul style="list-style-type: none"> • Registration of transition to a public interest incorporated association (April 1) • Event to mark the 65th anniversary of founding and transition to a public interest incorporated association (June 2) • Renaming as public interest incorporated association JART 	
		<ul style="list-style-type: none"> • Launch of the Radiological Technologists Liability Insurance System with participation by all members
		2013
		<ul style="list-style-type: none"> • Signing of the Comprehensive Mutual Cooperation Agreement on Prevention of Radiation Exposure (September 21)
		2014
		<ul style="list-style-type: none"> • Consignment of work to measure personal exposure of residents • Revision of the Act on Radiological Technologists, Government Ordinance to Partially Revise the Enforcement Orders, and Revision of the Enforcement Regulations (June 25) • Launch of the radiation exposure advisor certification system
		2015
		<ul style="list-style-type: none"> • Event to commemorate the 120th anniversary of the discovery of X-rays
		2017
		<ul style="list-style-type: none"> • Event to mark the 70th anniversary of founding (June 2)
		2018
		<ul style="list-style-type: none"> • Notice from the Regional Medical Care Planning Division Director, Health Policy Bureau, Ministry of Health, Labour and Welfare, and Director of the Economic Affairs Division regarding Operational Considerations for Securing a System for Safety Management pertaining to Medical Equipment
		2019
		<ul style="list-style-type: none"> • Notice from the Health Policy Bureau on a Safety Management System for Medicinal Use of Radiation
		2020
		<ul style="list-style-type: none"> • Partial revision of the Ordinance on Prevention of Ionizing Radiation Hazards
		2021
		<ul style="list-style-type: none"> • Relocation of offices to the Mita Kokusai Building in Tokyo • Partial revision of the designation regulation for radiological technologist training school • Holding the 23th AACRT with 37th JCRT in Tokyo
		2022
		<ul style="list-style-type: none"> • Event to mark the 75th anniversary of founding (July 16)

Radiological assessment of joint space width using different weight-bearing radiographic methods for knee osteoarthritis

YAMAGUCHI Masanori¹⁾, KOSEKI Hironobu²⁾, ENGUCHI Kousei¹⁾, IWANAGA Hitoshi³⁾, KYUMA Shunta¹⁾, SHINDO Hiroyuki³⁾

1) Department of Radiology, Wajinkai Hospital

2) Department of Health Sciences, Nagasaki University Graduate School of Biomedical Sciences

3) Department of Orthopedic Surgery, Wajinkai Hospital

Note: This paper is secondary publication, the first paper was published in the JART, vol. 65 no. 783: 22-26, 2018.

Key words: Osteoarthritis, Knee, Joint space width, Radiograph

[Abstract]

Background. Although joint space width on weight-bearing radiographs of the knee is critical for early diagnosis and grading knee osteoarthritis, the optimal method with which to accurately measure this value remains controversial.

Materials and Methods. We compared plateau gaps and joint space widths on bilateral weight-bearing plain radiographs acquired using three different methods in 17 medial knee osteoarthritis patients (32 knee joints): standing with the knee extended (standard imaging method); SynaFlexer method; and modified Rosenberg method. Measured values were compared statistically, with values of $P < 0.05$ considered significant.

Results. Maximum plateau gap in the medial compartment was significantly lower with the SynaFlexer method (3.9 ± 1.3 mm) and modified Rosenberg method (2.9 ± 1.5 mm) than with standard imaging method (5.8 ± 2.0 mm; $P < 0.05$ each). Minimum width of the medial joint space was also significantly lower with the SynaFlexer method (3.6 ± 1.3 mm) and modified Rosenberg method (3.1 ± 2.1 mm) than with standard imaging method (4.6 ± 1.6 mm; $P < 0.05$ each).

Conclusion. With the SynaFlexer method and the modified Rosenberg method, the X-ray beam can pass parallel to the medial tibial plateau, and the area with the most thinning of femoral condylar cartilage can be observed. Therefore, we believe that the SynaFlexer and modified Rosenberg methods are useful for diagnosing early osteoarthritis and for the assessment of disease severity.

1. Background

Knee osteoarthritis (OA) is one of the most common musculoskeletal disorders, particularly among elderly persons. This is of major concern because the proportion of people in this age range is rapidly increasing, and a medical means to stop progression of knee OA is currently unavailable. The estimated prevalence of symptomatic and asymptomatic knee OA in Japan is about 8 and 25 million respectively¹⁾. In order to diagnose and evaluate the severity of knee OA, the precise measurement of articular cartilage thickness is essential²⁾.

Magnetic resonance imaging (MRI) can directly visualize joint cartilage and provide an accurate measure of cartilage volume, thick-

ness, and surface areas³⁾. However, investigations of articular cartilage using MRI have generally been limited to quantifying total cartilage plates or femoral sub-regions because the progression of cartilage loss occurs heterogeneously⁴⁾. Moreover, MRI requires a large accommodation space and specially dedicated technicians, and may cause distress for claustrophobic patients. Measuring joint space width (JSW) in weight-bearing radiographs can indirectly reflect articular cartilage thickness and it is currently accepted as the primary structural outcome measure for clinical studies of knee OA. X-ray equipment spreads widely in many institutions, and is relatively inexpensive. Although standard weight-bearing radiographic assessment of JSW is generally accepted as the

most relevant⁵⁾, it is associated with some problems. Multi-center trials have verified that JSW reproducibility on knee radiographs acquired in the traditional weight-bearing position with full knee extension is inadequate^{6, 7)}. Furthermore, visualizing both the anterior and posterior margins of the tibial plateau is often inadequate because most knee OA occurs in the medial compartment, the optimal alignment of which is usually inclined posteriorly⁸⁾. Moreover, the most obviously thinned region of articular cartilage is in the 30° ~ 60° posterior aspect of the femoral condyle, which cannot be reflected^{8, 9)}. Therefore, a critical need for accurate and precise radiographic quantitation has emerged.

The present study aimed to define differences in measured values derived from plain weight-bearing radiographs of the knee acquired using three different methods and to investigate the optimal usage to evaluate knee OA. This study was approved by the Ethical Review Board of Wajinkai hospital and the objectives of which were explained in detail in writing and verbally to all participants. Informed consent was obtained from each patient prior to enrollment.

2. Patients and Methods

Patients

17 patients (32 knee joints) with medial knee OA were qualified for inclusion based on clinical and radiographic evidence of chronic knee pain with Osteoarthritis Research Society International (OARSI) grades 1 or 2¹⁰⁾. Exclusion criteria included evidence of other types of arthritis, such as previous trauma, surgical intervention, or treatment with corticosteroids. Participants included 12 female patients (22 knee joints) and 5 male patients (10 knee joints), and the average age of was 64.7 years (range: 55 - 84 years) (Table 1). All patients were seronegative for rheumatoid factor and had erythrocyte sedimentation rates within the normal range.

Table 1 Physical characteristics of the study participants

Age	64.7 (55~84)
Hight (cm)	159.5 (148~176)
Body weight (kg)	65.0 (55~100.4)
BMI(Body Mass Index)(kg/m ²)	25.5 (19.7-32.4)

Experimental design

Bilateral femorotibial radiographs were taken using a high-voltage device (KXO-80G, Toshiba, Tokyo, Japan) and a beam-limiting device (TF-6TL-6, Toshiba) under conditions of 50 kV, 100 mA, 0.1 sec. and an image distance of 100 cm. All imaging was performed by one radiology technician under uniform conditions. Three different radiographic methods were adapted for imaging (Figures 1a-1c: standardized radiographic method (standard imaging group) and two semi-flexed techniques including SynaFlexer method (SynaFlexer group) and modified Rosenberg method (Rosenberg group). The standard imaging was proceeded with patients standing upright with their knees extended and their feet parallel position. The X-ray beam was focused directly over the mid-point of the femorotibial joint antero-posteriorly (Figure 1a). In the SynaFlexer group, semi-flexion posteroanterior (PA) radiographs were taken with the SynaFlexer™ (Synarc, Inc., San Francisco, CA, USA), which is a commercially available Plexiglass frame to standardize knee flexion and foot positioning^{11, 12)}. The frame allows convenient, reproducible positioning of the knee for serial examinations without a need for creation and storage of foot maps. The feet were externally rotated 10°, and the thighs touched the vertical platform anteriorly, resulting in a fixed knee flexion of approximately 20°. The X-ray beam was angled at 10° caudally (Figure 1b). In the Rosenberg group, PA radiographs were taken according to the original Rosenberg method basically⁸⁾. We

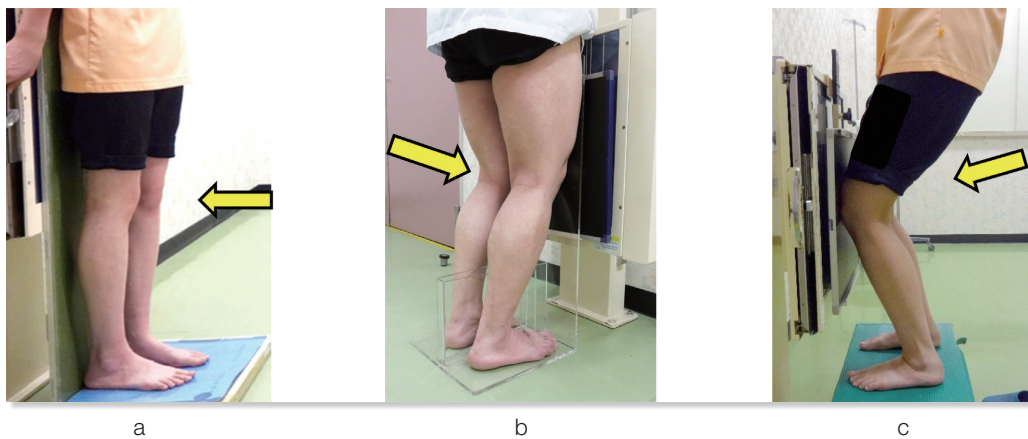


Figure 1 Acquisition of radiographs

Standing with knees extended (standard imaging method; a), SynaFlexer method (b) and modified Rosenberg method (c).

X-ray beam (arrow) was directed anteroposteriorly in standard imaging method, and posteroanteriorly in SynaFlexer and modified Rosenberg methods.

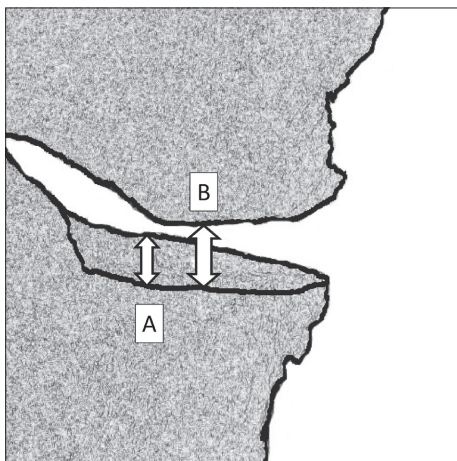


Figure 2 Methods of measuring plateau gap and joint space width.a

Maximum value of plateau gap (A)

Minimum value of joint space width (B)

Both values were measured parallel to tibial axis.

finely adjusted X-ray beam angles with reference to the angle between the axis of fibula and medial tibial plateau in lateral view of the knee (Figure 1c). The acquired images were assessed after conversion to DICOM format (L1750, HP Inc.) (17-inches' resolution, 1,280*1,024 pixels) and then, the plateau gap and JSW were measured through the image analyzing software (POP-Net Essential ver. 4.2C, imageONE Co., Ltd., Tokyo, Japan).

After the contours of the medial and lateral compartments of femur and tibial plateaus

were delineated, the maximum distance of plateau gap (between the anterior and posterior edges of tibial plateau) and the minimum JSW between opposing weight-bearing subchondral cortical surfaces was measured (Figure 2). Three observers evaluated radiographs from each patient twice at a minimal interval of two weeks. Intra-observer reliability was assessed based on evaluations by the first author, and inter-observer reliability was assessed based on evaluations between the first and second authors. The readers were blinded to the initial measurements, and mean values were taken as the measured values.

Statistical analysis

The reproducibility and intra-observer reliability of the measurement was assessed using kappa statistics. Parameters (plateau gap and JSW) were compared among the three methods using a one-way analysis of variance (ANOVA) and Tukey-Kramer and Bonferroni/Dunn *post hoc* multiple comparison tests. Significance was defined at $P < 0.05$.

3. Results

Test-retest reproducibility and intra-observer reliability did not significantly differ (kappa

values, 0.76 and 0.86, respectively). Table 2 shows the mean values and standard deviations of the plateau gap and JSW in each assessment method. The mean values of the plateau gap of medial compartment were significantly smaller for the SynaFlexer and Rosenberg group, than the standard imaging group (3.9 ± 1.3 and 2.9 ± 1.5 vs. 5.8 ± 2.0 , $P < 0.05$; Figure 3). The average JSW value of medial compartment was also significantly smaller for the SynaFlexer and Rosenberg group, than the standard imaging group (3.6 ± 1.3 and 3.1 ± 1.5 vs. 4.6 ± 1.6 , $P < 0.05$). On the other hand, no statistically difference of plateau gap and JSW were seen in lateral compartment of knee joint among the three groups ($P > 0.05$).

Table 2 Comparisons of plateau gap and joint space width among the three methods

		(mm)	Standard imaging	SynaFlexer	Rosenberg
Plateau gap	medial		5.8 ± 2.0	$3.9 \pm 1.3^*$	$2.9 \pm 1.5^*$
	lateral		3.0 ± 2.0	2.0 ± 1.4	1.8 ± 1.2
Joint space width	medial		4.6 ± 1.6	$3.6 \pm 1.3^*$	$3.1 \pm 1.5^*$
	lateral		5.6 ± 1.8	5.1 ± 1.4	5.6 ± 2.1

*: $P < 0.05$ compared to the standard imaging group

4. Discussion

For diagnosis of early knee OA or assessment of disease severity, accurate and precise articular cartilage thickness, which is reflected by optimal tibiofemoral JSW values derived from weight-bearing knee radiograph, is critical. A number of studies, however, verified that the reproducibility of JSW determined from traditional weight-bearing radiographs with full knee extension is inadequate^{7, 13)}, because of the insufficiency of anterior and posterior margins of the medial tibial plateau¹¹⁾. Moreover, a pathological study by Messieh et al.¹⁴⁾ indicated that most OA cartilage destruction occurs in a posterior site of the femoral condyle. Therefore, the JSW in patients with knee OA might be much smaller on radiographs acquired with the knee at various degrees of flexion^{14, 15)}. However, the accuracy of these views for JSW assessment has rarely been scientifically evaluated quantitatively.

The present study assessed femorotibial JSW in patients with knee OA and investigated discrepancies among three radiographic methods. The plateau gap and JSW were significantly smaller in the same patients with medial knee OA assessed using the SynaFlexer and Rosenberg methods, than the standard imaging



Figure 3 Representative X-rays of 62-year-old female patient acquired using three methods.

Standing with knee extension (standard imaging method; A): medial plateau gap and joint space width, 6.4 and 5.7 mm, respectively. SynaFlexer method (B): medial plateau gap and joint space width, 3.6 and 3.0 mm, respectively. Modified Rosenberg method (C): medial plateau gap and joint space width, 2.0 and 2.6 mm, respectively.

method. An increased plateau gap blurs the anterior and posterior margin of the tibial plateau, which leads to inaccurate JSW measurements⁶⁾. Therefore, consort of these two margins (small plateau gap) is indispensable for precise JSW measurements. Decrease of JSW in the knee flexion methods is consistent with arthroscopic findings, showing that OA cartilage destruction occurs at a posterior site of the femorotibial joint^{8, 9)}. Matsuda et al. reported that the medial tibial plateau in the Japanese population posteriorly inclines approximately 10°¹⁶⁾. In the present study, the value of plateau gap and JSW of medial compartment in Rosenberg group were statistically small compared to the standard imaging group. Piperno et al.⁷⁾ suggested that the schuss view, which is a variant of the Rosenberg method, can also visualize evidence of osteophytosis, which is helpful to diagnose early OA. From these reasons, images of a flexed knee such as in Rosenberg method, are currently considered more sensitive for screening knee OA compared to traditional weight-bearing radiographs^{7, 17)}. We devised fine adjustment way of X-ray beam angle with reference to the knee lateral view to minimize radiation exposure. However, there remains several problems. For example, some patients suffering from knee OA cannot flex their knees at 45° and if they can, pain often prevents them from maintaining the position long enough to take images¹⁸⁾. The plexiglass SynaFlexer frame, on the other hand, standardizes knee flexion and foot positioning. Charles and Kothari et al reported that SynaFlexer frame allows convenient, reproducible positioning of the knee and engagement of the most damaged femoral articular cartilage to produce images that are of similar quality to Rosenberg view^{11, 12)}. Patients only have to place their feet in the foot support and touch their thighs to the vertical platform anteriorly, which allows examinations of even elderly patients with joint contracture and pain. The plateau gap and JSW on SynaFlexer images in the

present study were statistically smaller than those on standard images that were not inferior to Rosenberg images. A small plateau gap means that the direction of the X-ray beam is almost parallel to the tibial plateau. The present findings indicate that the Rosenberg method is beneficial to diagnose early knee OA in relatively young and active patients, whereas the SynaFlexer method is more appropriate for assessing disease severity or progression in patients with painful intermediate to severe knee OA.

The present study has several limitations. A significant positive difference in the plateau gap and JSW of the lateral femorotibial joint was not identified. It is assumed that all patients included in this study had confirmed medial knee OA and that they had no evidence of cartilage damage or destructive changes in the lateral compartment of the knee. In addition, multiple regression analysis could not be performed for small number of patients. Large sample cohort study including lateral knee OA patients should be assessed in a future. Nonetheless, the present findings provide valuable information about measuring JSW using different imaging methods, which should impact clinical diagnoses and assessments of knee osteoarthritis severity.

5. Conclusions

We compared the plateau gap and joint space width of 32 knees with osteoarthritis on radiographs acquired using three different methods of bilateral weight-bearing radiographs (standard imaging, SynaFlexer, and modified Rosenberg method). The maximum value of the plateau gap and the minimum value of the joint space width of the medial compartment in images acquired were significantly higher using the standard imaging method, than the SynaFlexer and modified Rosenberg methods ($P < 0.05$). The SynaFlexer and modified Rosenberg methods might be useful for

diagnosing early osteoarthritis and for assessing disease severity in various populations, including elderly people.

6. Declarations

Funding

This work was supported by the Grants-in-Aid for Scientific Research of Japan Society for the Promotion of Science, Grant Number 232024000.

Conflict of interest / Competing interests

Masanori Yamaguchi, Hironobu Koseki, Kousei Enguchi, Hitoshi Iwanaga, Shunta Kyuma, Hiroyuki Shindo declare that they have no conflicts of interest nor competing interests. All authors have not and will not receive benefits or funding from any commercial party directly or indirectly related to the subject of this article.

Availability of data and material

The authors do not wish to share the data because the dataset is part of ongoing study protocols.

Code availability

Not applicable

Authors' contributions

All authors substantially contributed to this article. MY and HK conceived and designed the study. MY, HK, KE, HI, and SK participated in the experiments and gathered data. MY, HK, and HI analyzed and interpreted the data. MY initially drafted the manuscript, and MY and HS statistically analyzed and ensured the accuracy of the data. All authors have read and approved the final version of the manuscript and affirm that the work has not been submitted or published elsewhere in whole or in part.

Ethics approval

All procedures in studies involving human participants were performed in accordance

with the ethical standards of the institutional and/or national research committee and in line with the 1964 Declaration of Helsinki and its later amendments or comparable ethical standards. This study was approved by the ethics review board of the authors' affiliated institutions (approval code 2017-2301). The nature of the study was thoroughly explained to each patient, and all patients provided written, informed consent prior to participation.

Consent for publication

Not applicable.

References

- 1) Yoshimura N, et al.: Prevalence of knee osteoarthritis, lumbar spondylosis, and osteoporosis in Japanese men and women: the research on osteoarthritis/osteoporosis against disability study. *J Bone Miner Metab*, 27, 620-628, 2009.
- 2) Kellgren JH, Lawrence JS: Radiological assessment of osteoarthrosis. *Ann Rheum Dis*, 16, 494-502, 1957.
- 3) Eckstein F, et al.: Magnetic resonance imaging (MRI) of articular cartilage in knee osteoarthritis (OA): morphological assessment. *Osteoarthritis Cartilage*, 14, 46-75, 2006.
- 4) Wirth W, Eckstein F: A Technique for Regional Analysis of Femorotibial Cartilage Thickness Based on Quantitative Magnetic Resonance Imaging. *IEEE Trans Med Imaging*, 27, 737-744, 2008.
- 5) Lequesne M, et al.: Guidelines for testing slow acting drugs in osteoarthritis. *J Rheumatol Suppl*, 41, 65-71; discussion 72-63, 1994.
- 6) Buckland-Wright JC, et al.: Joint space width measures cartilage thickness in osteoarthritis of the knee: high resolution plain film and double contrast macro-radiographic investigation. *Ann Rheum Dis*, 54, 263-268, 1995.
- 7) Piperno M, et al.: Quantitative evaluation of joint space width in femorotibial osteoarthritis: comparison of three radiographic views. *Osteoarthritis Cartilage*, 6, 252-259, 1998.
- 8) Rosenberg TD, et al.: The forty-five-degree postero-anterior flexion weight-bearing radiograph of the knee. *J Bone Joint Surg Am*, 70, 1479-1483, 1988.
- 9) Davies AP, et al.: Plain radiography in the degenerate knee. A case for change. *J Bone Joint Surg Br*, 81, 632-635, 1999.

-
- 10) Altman RD, Gold G: Atlas of individual radiographic features in osteoarthritis, revised. *Osteoarthritis Cartilage*, 15, A1-A56, 2007.
 - 11) Charles HC, et al.: Optimization of the fixed-flexion knee radiograph. *Osteoarthritis Cartilage*, 15, 1221-1224, 2007.
 - 12) Kothari M, et al.: Fixed-flexion radiography of the knee provides reproducible joint space width measurements in osteoarthritis. *Eur Radiol*, 14, 1568-1573, 2004.
 - 13) Brandt KD, et al.: Radiographic grading of the severity of knee osteoarthritis: relation of the Kellgren and Lawrence grade to a grade based on joint space narrowing, and correlation with arthroscopic evidence of articular cartilage degeneration. *Arthritis Rheum*, 34, 1381-1386, 1991.
 - 14) Messieh S, et al.: Anteroposterior radiographs of the osteoarthritic knee. *J Bone Joint Surg Br*, 72, 639-640, 1990.
 - 15) Marklund T, Myrnerets R: Radiographic determination of cartilage height in the knee joint. *Acta Orthop Scand*, 45, 752-755, 1974.
 - 16) Matsuda S, et al.: Posterior tibial slope in the normal and varus knee. *Am J Knee Surg*, 12, 165-168, 1999.
 - 17) Vignon E, et al.: Advances in radiographic imaging of progression of hip and knee osteoarthritis. *J Rheumatol*, 32, 1143-1145, 2005.
 - 18) Inoue S, et al.: Anteroposterior weight-bearing radiography of the knee with both knees in semiflexion, using new equipment. *J Orthop Sci*, 6, 475-480, 2001.

New simple imaging method for short-axis view in cardiac MRI inferred from chest X-ray

FUJII Tomoki¹⁾, USUI Hiromi²⁾, SATO Hisaya^{1),3)}, KATO Kyoichi^{3),4)}

1) Showa University Hospital, Department of Radiological Technology

2) Showa University Northern Yokohama Hospital, Department of Radiological Technology

3) Showa University Graduate School of Health Sciences

4) Showa University Radiological Technology

Note: This paper is secondary publication, the first paper was published in the JART, vol. 68 no. 819: 20-29, 2021.

Key words: Cardiac Magnetic Resonance Imaging, Short Axis, Chest X-rays, Coronary Computed Tomography Angiography, New simple imaging method, Reliable imaging method

[Abstract]

Cardiac Magnetic Resonance Imaging (CMRI) is often performed under respiratory standstill. Vertical Long Axis imaging (VLA) and Horizontal Long Axis imaging (HLA) are used to acquire short-axis imaging (SA) although it requires patients to hold their breath for a long time. Therefore, in some patients, the image quality in SA may be affected by repeated breath-holds. This study aims to devise a new method to acquire SA without VLA and HLA.

Initially, 116 patients who underwent Coronary Computed Tomography Angiography (CCTA) and front and lateral chest X-rays were investigated to assess the relationship between the SA angle in the CCTA images and the angle of the cardiac shadow in the X-rays for application in the new method. Then, 20 subjects were randomly selected for assessment of inter- and intra-reproducibility studies. Finally, 10 participants underwent CMRI using the new and the conventional methods for visual and objective evaluations.

A strong relation was found between the SA angle and the cardiac shadow. The measurements of the SA angle and the cardiac shadow were excellently reproducible. Compared with the conventional method, the new method proposed in this study has improved the time of respiratory standstills. It is suggested that this new method has the potential to provide a high-quality image as obtained with the conventional method.

1. Introduction

Cardiac Magnetic Resonance Imaging (MRI) is an indispensable examination that can diagnose cardiac function and display morphological information. Cardiac MRI is also useful in evaluating the prognosis of patients with coronary artery disease^{1), 2)}. Cardiac delayed contrast MRI has been used for myocardial viability diagnosis of myocardial infarction and is reported to be effective in the detection of right ventricular infarction and asymptomatic infarction^{3), 4)}. In addition, stress tested myocardial perfusion MRI has higher spatial resolution than single-photon emission computed tomography (SPECT), and it has been reported to enable the visualization of subendocardial ischemia clearly⁵⁾.

Cardiac cine MRI can acquire a moving image in an arbitrary direction without

artifacts due to bone or air compared with ultrasonography. Currently, cardiac cine MRI is the gold standard of cardiac function diagnosis method because it can acquire left ventricular function accurately and quantitatively in most myocardial deformities and abnormalities⁶⁾. Furthermore, quantitative analysis of the left ventricular function using cardiac cine MRI is highly reproducible^{7), 8)}.

Cardiac cine MRI is performed under paused breathing. To obtain a short-axis cross-sectional image of the heart, the imaging section is commonly set by using the vertical long-axis section image (VLA) and horizontal long-axis section image (HLA). However, VLA and HLA imaging require the patient to stop respiration for several seconds. Therefore, the diagnosis of cardiac function analysis is affected in patients with difficulty in stopping respiration due to poor short-axis cross-

sectional images. In such patients, images can be acquired for cardiac MRI using synchronous respiration imaging along with synchronous electrocardiogram imaging. However, this method is tedious for the operator and patients, as it takes longer examination time for imaging. Moreover, the short-axis cross-sectional image is acquired by the operator subjectively based on a short axis defined as the perpendicular cross-sectional images connecting the apex and the base of the heart. This subjective position setting might differ from operator to operator, thereby causing an uncertainty in the position.

This study aims to suggest a new examination method for acquiring short-axis cross-sectional images without HLA and VLA by using the cardiac shadow of the chest X-ray.

2. Methods

2.1 Materials

SOMATOM Definition AS+ (SIEMENS Co., Ltd.) was used for the CT examination, BENEOL (FUJIFILM Co.) for the X-ray examination, and MAGNETOM AVANTO 1.5T (SIEMENS Co., Ltd.) for the cardiac MRI. ZIO Station2 (Amin Co.) was used as a medical image processing workstation for measuring the short-axis angle

of the cardiac CT image. Synapse (FUJIFILM Co.) was used for the measurement of the short-axis angle in the X-ray image. Statistical analysis was performed using JMP 13.0 (SAS Institute Inc.).

2.2 Measurement of short axis in cardiac X-ray and CT

2.2.1 Participants

The subjects in the study were 116 patients who had underwent coronary computed tomography angiography (CCTA) and front and lateral chest X-ray examinations from January 2012 to August 2013. No criteria were set for the time interval between the chest X-ray examination and the CCTA examination. Characteristic of the 116 participants was shown in Table 1. CCTA examination have been performed in various ways, and most patients who underwent CCTA were suspected of stable work angina. Two of the 116 patients underwent CCTA for morphological assessment of dilated cardiomyopathy or cardiac tumor. Also, 14 of the 116 patients (12%) have history of Cardiac hypertrophy.

As a result of CCTA, 51 participants were confirmed at least 50% stenosis at coronary artery (15 in one-branch, 11 in two-branch, and 25 in three-branch, respectively). Also,

Table 1 Characteristic of the 116 participants who underwent CCTA

Parameters	Studied Group (N=116)	Parameters	Studied Group (N=116)	Parameters	Studied Group (N=116)
Sex		Purpose of CCTA examination		Diagnosis for CCTA*	
Male	75 (64.7%)	Stable work angina	36	Coronary Disease	51
Female	41 (35.3%)	OMI	16	Single vessel disease	15
Age (years)		Chest pain	11	Double vessel disease	11
Mean \pm SD	66.4 \pm 13.7	Exertion angina	9	Triple vessel disease	25
Range	24 - 89	palpitation	6	Intact vessels	65
Height (cm)		Heart Failure	5	Kawasaki disease	1
Mean \pm SD	161.8 \pm 8.9	Back pain	4	Dilated cardiomyopathy	1
Range	140.0 - 180.0	Paroxysmal atrial fibrillation	4	Cardiac tumor	1
Weight (kg)		syncope	4	History of Cardiac Hypertrophy	14
Mean \pm SD	61.6 \pm 14.7	Vasospastic angina	4		
Range	28.0 - 162.0	Chronic atrial fibrillation	3		
Body Mass Index (kg/m ²)		PVC	3		
Mean \pm SD	23.4 \pm 4.43	AMI	2		
Range	10.0 - 50.0	Heart murmur	2		
		Screening for operation	2		
		Chest compression	2		
		Kawasaki disease	1		
		Dilated cardiomyopathy	1		
		Cardiac tumor	1		

Value are mean \pm SD.

* Multiple selections were possible in these parameters

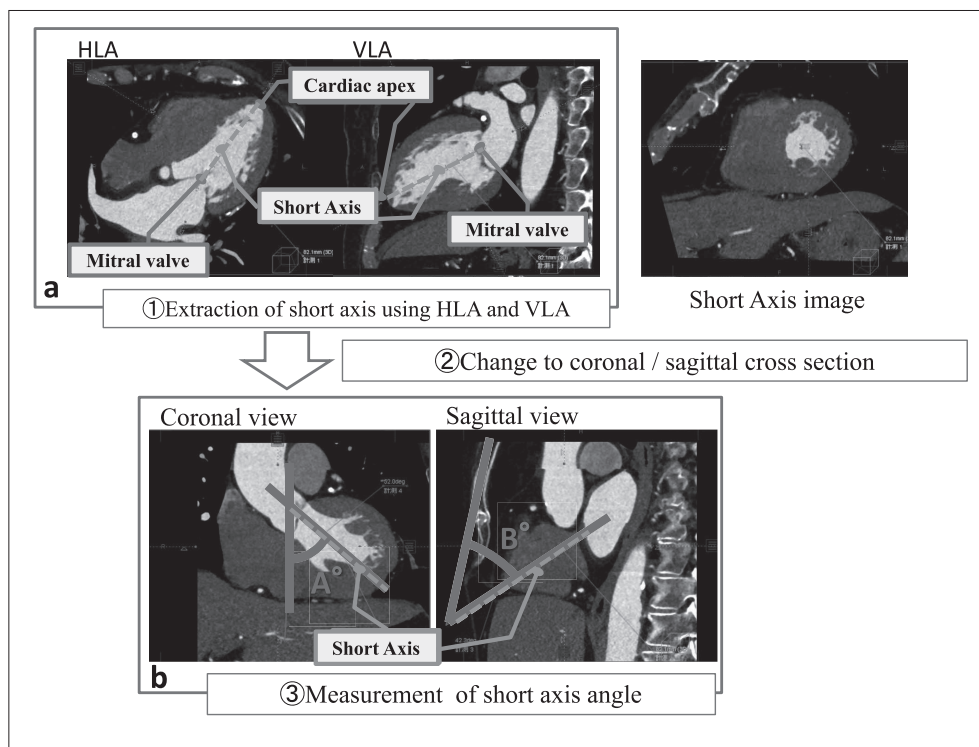


Fig.1 Extraction and measurement of cardiac short-axis angle in CT imaging

- a: HLA and VLA images were displayed using Multi-Planar Reconstruction (MPR) from the volume CT data. A line connecting the center of the mitral valve and the apex of the heart was defined as the "short axis", which was drawn using a 3D measurement tool.
- b: The coronal and sagittal section was displayed using the CT volume data. The angle "A" between the body axis and the short axis of the heart and the angle "B" between the sternum and the short axis of the heart were measured as the short axis angle.

few patients diagnosed with Kawasaki disease, dilated cardiomyopathy, and heart tumors were also included. This research was approved by the Ethics Committee at the Showa University School of Medicine.

2.2.2 Visualization of the cardiac short axis in CT

HLA and VLA images were displayed using Multi-Planar Reconstruction (MPR) from the volume CT data. A line connecting the center of the mitral valve and the apex of the heart was defined as the "short axis", which was drawn using a 3D measurement tool (Fig.1a).

2.2.3 Measurement of cardiac short-axis angle in CT imaging

The coronal section was displayed using the CT volume data. The angle "A" between the body axis and the short axis of the heart was measured. The body axis is based on the

spinous processes of the thoracic vertebrae, and when the deformity of the thoracic vertebra is significant, it is based on the axis of the sternum.

Next, the sagittal section was displayed using the same volume data. Following this, the angle "B" between the sternum and the short axis of the heart was measured. Lateral chest X-ray examination was performed in a standing position, and the body axis depicted on the image changes according to the examined position. To evaluate the anatomical angle, we measured the angle between the sternum and the short axis of the heart (Fig.1b).

2.2.4 Measurement of cardiac shadow in chest X-ray image

Using the cardinal shadow of the XP frontal image, a cardiac lateral edge corresponding to

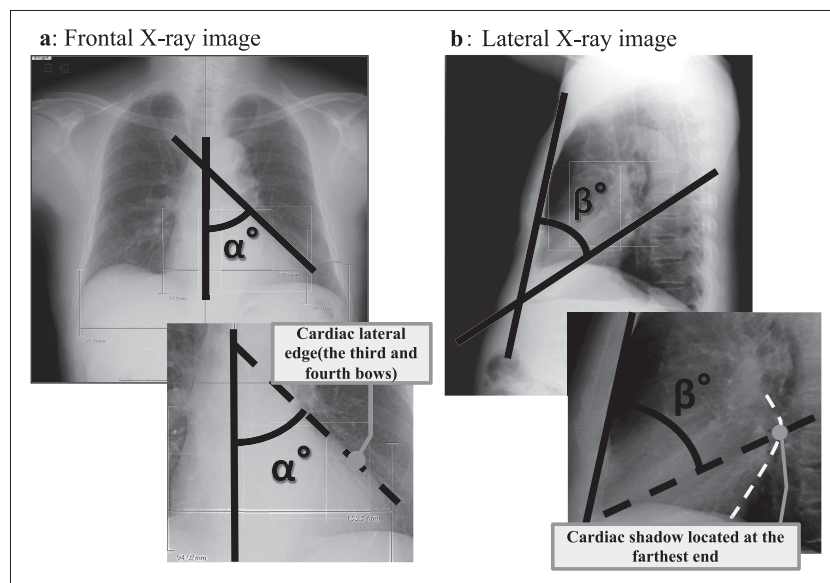


Fig.2 Measurement of cardiac shadow in chest X-ray image

- a: A cardiac lateral edge corresponding to the third and fourth bows were connected as the line for measurement of the angle α formed by this line and the median in the XP frontal image.
- b: The point of the cardiac shadow located at the farthest end and the apex of the heart were connected by a line using the XP lateral image. The angle β between this line and the sternum axis was measured.

the third and fourth bows representing the left atrium and the left ventricle were connected as the line for measurement of the angle α (expected short axis from the XP frontal image) formed by this line and the median (Fig.2a). The median is based on the spinous processes of the thoracic vertebrae; when the deformity of the thoracic vertebra is intense, it is based on the sternum axis.

Next, an XP lateral image was displayed on Synapse. From the anatomical structure, we noticed that the left atrium is the most dorsal side of the heart. Therefore, the point of the cardiac shadow located at the farthest end and the apex of the heart were connected by a line using the XP lateral image. The angle β between this line and the sternum axis (the expected short axis from the XP lateral image) was measured (Fig.2b).

2.2.5 Comparison of cardiac short axis in chest X-ray and CT

The relationship between the chest X-ray image described above and the minor axis angle of the CT was examined. We analyzed

the relevancies of the angle α of the cardiac shadow in the XP frontal view and the short-axis cardiac angle A in the coronal section as well as the angle β of the cardiac shadow in the XP lateral image and the cardiac short-axis angle B in the sagittal section using the cardiac CT. The analysis was performed using Pearson's correlation of the regression line. A linear approximation formula of the regression line of angle α and angle A, and that of angle β and angle B were calculated for angle consistency.

2.2.6 Verification of reproducibility of measurement method

Inter-observer and intra-observer reproducibility analyses were performed by two experienced observers in 20 cases randomly extracted from the cases selected for the study. As parameters of the reliability analysis, the intraclass correlation coefficient (ICC) and the difference between the measurements of both groups as the mean difference and standard deviation of the mean difference were measured. We evaluated the

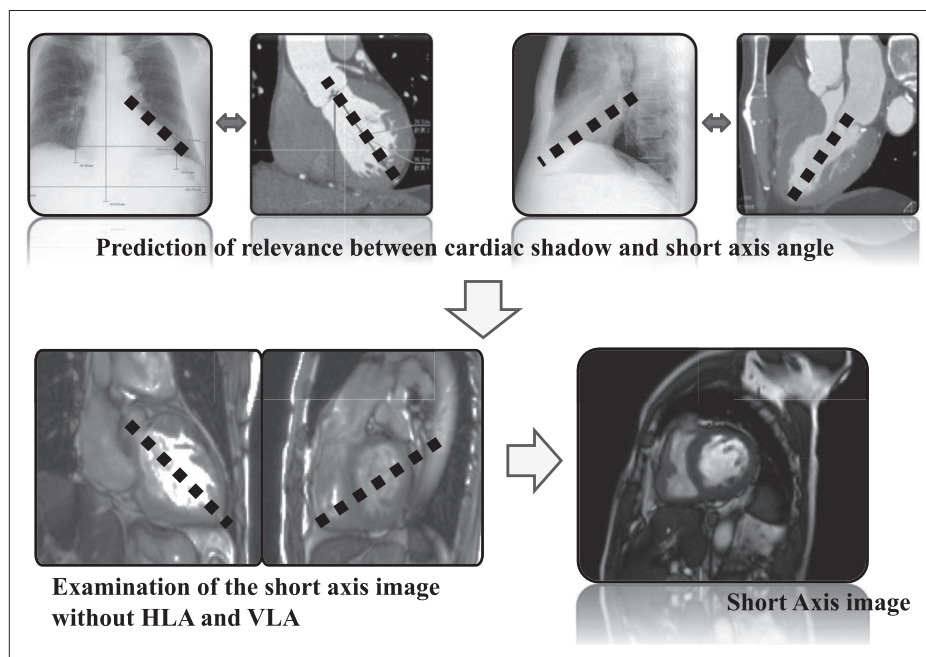


Fig.3 New imaging procedure of short axis imaging

ICC higher than 0.8 as “Excellent” and from 0.6 to 0.8 as “Moderate”. The interval in each intra-reliability analysis was more than two weeks. The inter-reliability analysis was performed using the above-described measurement method by a radiologic technologist with 5 or more years of experience in projectional radiography and CT examination. Each result was evaluated by comparing with the underlying analysis data.

2.3 Comparison between the new method and the conventional method

Cardiac cine magnetic resonance imaging was performed on a subject by using the result obtained from the relation between the cardiac shadow and the true short-axis angle.

2.3.1 Participants

The 10 participants were volunteers who agreed to perform cardiac cine MRI examination and agreed with the purpose of this study. The participants were randomly divided into two groups to compare the conventional and new methods.

2.3.2 Examination of cardiac cine MRI with short-axis angle obtained from cardiac shadow

A localized image was taken containing three directions corresponding to the transverse, coronal, and sagittal sections so that the position and morphology of the heart could be recognized. The localized image of the coronal section was taken from a cross section in which the margin of the heart was depicted. Similarly, the localized image of the sagittal section was imaged so that the apex of the heart and its dorsal side were visualized.

Next, using the localized images of the coronal and sagittal sections, the imaging angle was adjusted to the short-axis angle based on the relation between the cardiac shadow and the true short-axis angle, and cine imaging was performed in the range that included the entire left ventricle (Fig.3).

2.3.3 Reduction in imaging time of short-axis image by new method

Five radiologic technologists examined the short-axis image using the new method to find the time required to obtain the short-axis

Table 2 Rating criterion for the visual evaluation

Score	Rating criterion
5	No difference compared with the conventional method.
4	Acceptable on diagnosis although an angle may be difference compared with the conventional method.
3	Possibility to affect diagnosis due to a difference short axis angle compared with the conventional method.
2	Unacceptable on diagnosis
1	Not a short axis image

angle and determine whether the respiratory pause time of the subject could be shortened. The time to be considered is the time from the start of imaging of the localized image to the acquisition of the first short-axis image (the examination time) and the time for which breathing is withheld during the examination (the breath-hold time). The examination time was calculated from Synapse described on the DICOM image, and the breath-hold time was measured using a stopwatch during the examination. Wilcoxon’s signed-rank sum test was performed to assess the significant difference.

2.3.4 Comparison of short-axis images

We compared the short-axis image obtained by the conventional method and that captured by the new method. A visual evaluation was performed for comparison using confidence rating by the double blind method.

Two radiologic technologists with experience of 5 to 15 years and two cardiovascular physicians compared the short-axis images of the conventional and the new methods by the double blind method. Using confidence rating as a visual evaluation method, the conventional and new methods were scored based on the rating criterion shown in **Table 2**. A score was assigned in all cases, and significant difference

test was performed using a chi-square test.

3. Result

3.1 Measurement of cardiac short axis in chest X-ray and CT image

3.1.1 Measurement of short-axis angle of heart

In the measurement of the short-axis angle of the heart, the short-axis angle A for all cases was $46.0 \pm 11.1^\circ$. In addition, the short-axis supposed angle α for all cases was $42.6 \pm 10.1^\circ$ on average. The short-axis angle B for all cases was $47.6 \pm 7.2^\circ$, and the short-axis supposed angle β for all cases was $46.8 \pm 6.5^\circ$ (**Table 3**).

3.1.2 Relationship between the short-axis angle of the CT and the short-axis assumed angle of the chest X-ray

The relationship between the short-axis angle A and the short-axis supposed angle α is shown in **Fig.4**. The primary approximation formula was derived as $Y=0.94 X+6.13$ (Y: cardiac short-axis angle A in the coronal section in the CT image, X: short-axis supposed angle α in the XP front image) and Pearson’s correlation coefficient r was 0.85, suggesting a statistically strong correlation. The relationship between the short-axis angle B and the short-axis supposed angle β is shown in **Fig.5**. The primary approximation formula

Table 3 Measurement of cardiac short axis in chest X-ray and CT image

Measurement angle	Mean (SD)	Median [IQR]	Range
The short-axis angle A	46.0 (11.1)	46.4 [38.6 – 52.4]	21.4 – 72.4
The short-axis supposed angle α	42.6 (10.1)	42.0 [36.0 – 49.8]	18.0 – 69.0
The short-axis angle B	47.6 (7.2)	48.3 [44.0 – 51.8]	27.1 – 73.6
The short-axis supposed angle β	46.8 (6.5)	47.0 [42.5 – 51.0]	27.0 – 65.0

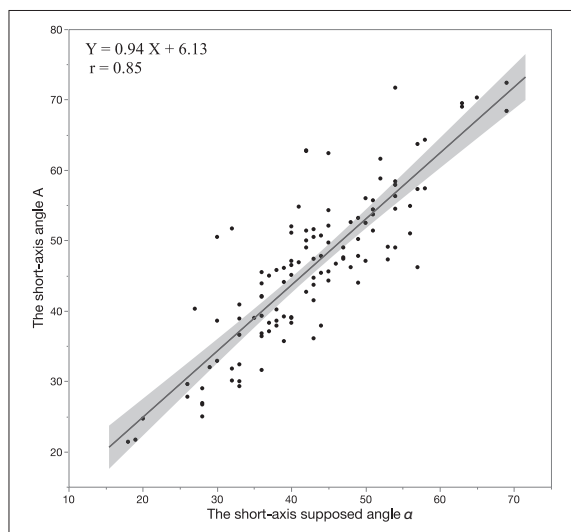


Fig.4 The relationship between the short-axis angle A and the short-axis supposed angle α

The primary approximation formula was derived as $Y=0.94 X+6.13$ (Y: cardiac short-axis angle A in the coronal section in the CT image, X: short-axis supposed angle α in the XP front image) and Pearson's correlation coefficient r was 0.85, suggesting a statistically strong correlation.

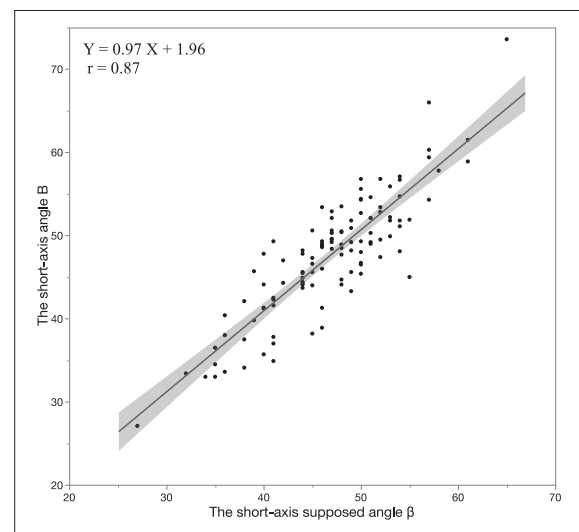


Fig.5 The relationship between the short-axis angle B and the short-axis supposed angle β

The primary approximation formula was derived as $Y=0.97 X+1.96$ (Y: cardiac short-axis angle B in the sagittal section in the CT image, X: short-axis supposed angle β in the XP lateral image) and Pearson's correlation coefficient r was 0.87, suggesting a statistically strong correlation.

Table 4 The assessment of reproducibility for the measurement of the short axis angle

Intra-observer reliability

Parameters	Analysis 1	Analysis 2	Mean Difference	ICC
The assumed short-axis angle α	43.4 ± 8.66	41.3 ± 9.41	-2.15 ± 2.63	0.91*
The assumed short-axis angle β	46.8 ± 6.58	45.9 ± 6.61	-0.90 ± 2.61	0.91*
The short-axis angle A	44.0 ± 9.71	43.7 ± 9.06	-0.32 ± 2.89	0.93*
The short-axis angle B	46.1 ± 7.11	45.0 ± 8.27	-1.03 ± 2.90	0.91*

Inter-observer reliability

Parameters	Observer 1	Observer 2	Mean Difference	ICC
The assumed short-axis angle α	43.4 ± 8.66	41.7 ± 8.27	-1.75 ± 3.85	0.82*
The assumed short-axis angle β	46.8 ± 6.58	47.0 ± 4.60	0.15 ± 2.97	0.83*
The short-axis angle A	44.0 ± 9.71	43.9 ± 9.35	-0.16 ± 4.54	0.87*
The short-axis angle B	46.1 ± 7.11	44.5 ± 6.05	-1.58 ± 2.92	0.87*

Value are Mean \pm SD, SD: standard deviation, ICC: intraclass correlation coefficient. * $p < 0.05$.

was derived as $Y=0.97 X+1.96$ (Y: cardiac short-axis angle B in the sagittal section in the CT image, X: short-axis supposed angle β in the XP lateral image) and Pearson's correlation coefficient r was 0.87, suggesting a statistically strong correlation.

3.1.3 Verification of reproducibility of measurement method

The results of the intra- and inter-

reproducibility are shown in Table 4. Regarding the intra-observer reliability of the chest X-ray, the mean difference at the assumed short-axis angle α was -2.15 ± 2.63 , and the ICC was 0.91. In addition, the mean difference at the assumed short-axis angle β was -0.90 ± 2.61 with ICC=0.91. Regarding the intra-observer reliability of the CT image, the mean difference at the short-axis angle A was -0.32 ± 2.89 , and the ICC was 0.93. The

mean difference at the short-axis angle B was -1.03 ± 2.90 with ICC=0.91.

In the inter-observer reliability test of the chest X-ray, the mean difference at the assumed short-axis angle α was -1.75 ± 3.85 , and the ICC was 0.82. In addition, the mean difference at the assumed short-axis angle β was 0.15 ± 2.97 with ICC=0.87. In the inter-observer reliability test of the CT, the mean difference at the short-axis angle A was -0.16 ± 4.54 , and the ICC was 0.87. In addition, the mean difference at the short-axis angle B was

-1.58 ± 2.92 with ICC=0.87.

3.2 Comparison of new and conventional methods

3.2.1 Comparison of imaging time of short-axis image

Comparison of the examination time in each method is shown in Fig.6 and the comparison of the breath-holding time is shown in Fig.7. The examination time in the conventional method was 619.4 ± 215.6 s and the breath-holding time was 122.0 ± 15.4 s. In

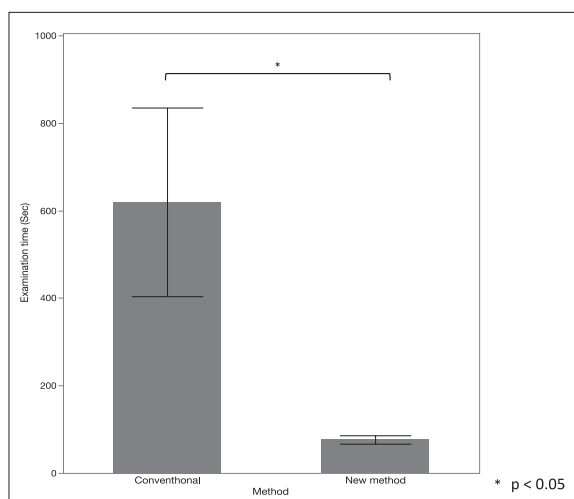


Fig.6 Comparison of the examination time in each method

The Boxes show the mean value, with whiskers indicate standard deviation. $*=p<0.05$.

The examination time in the new method was 76.4 ± 9.6 s although the conventional method was 619.4 ± 215.6 s ($p<0.05$).

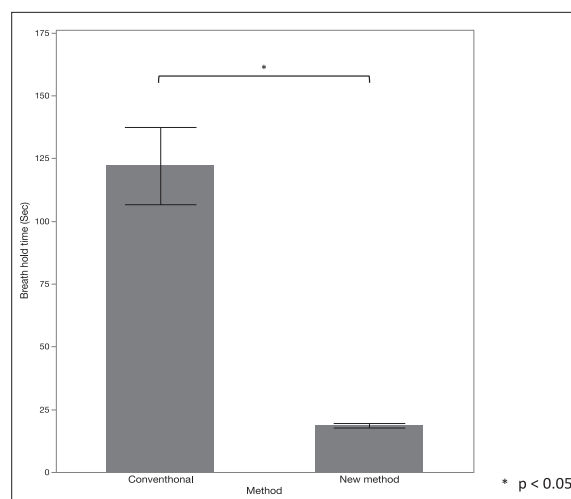


Fig.7 Comparison of the breath-holding time in each method

The Boxes show the mean value, with whiskers indicate standard deviation. $*=p<0.05$.

The examination time in the new method was 18.6 ± 0.9 s although the conventional method was 122.0 ± 15.4 s ($p<0.05$).

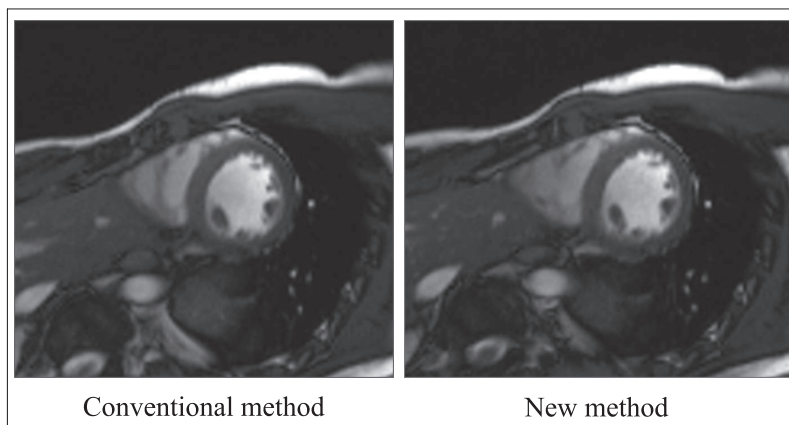


Fig.8 Examples of short-axis images with the conventional and the new methods

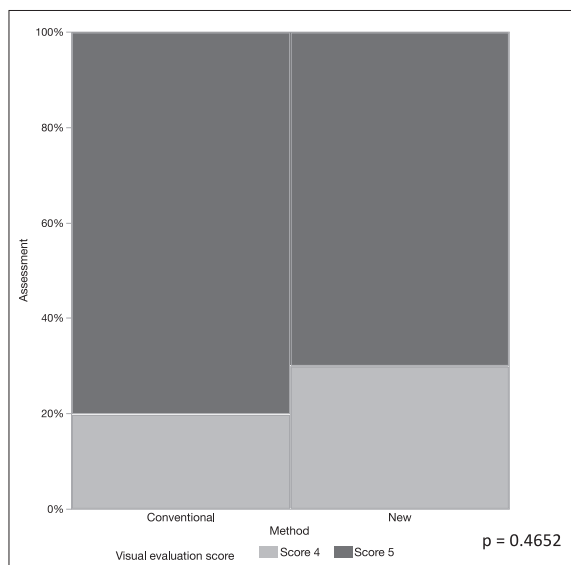


Fig.9 The results of the visual evaluations of the short-axis image by the conventional and the new methods

The average of the confidence rating method scores was 4.8 ± 0.4 points in the conventional method and 4.7 ± 0.4 points in the new method. No significant difference was observed between the conventional method and the new method in the chi-square test for visual evaluation ($p=0.4652$).

comparison, the examination time in the new method was 76.4 ± 9.6 s ($p < 0.05$ in comparison with the conventional method) and the breath-holding time was 18.6 ± 0.9 s ($p < 0.05$ in comparison with the conventional method).

3.2.2 Comparison of short-axis images

Examples of short-axis images with the conventional and the new methods are shown in Fig.8. Furthermore, the results of the visual evaluations of the short-axis image by the conventional and the new methods are shown in Fig.9. In the visual evaluation, the average of the confidence rating method scores was 4.8 ± 0.4 points in the conventional method and 4.7 ± 0.4 points in the new method. In the new method, one observer assigned 5 points to all cases, and the lowest score assigned by all observers was 4 points. In the result of the chi-square test for visual evaluation, no significant difference was observed between the conventional method and the new method ($p=0.47$).

4. Discussion

In this study, it was suggested that it is possible to estimate the cardiac short axis from the cardiac shadow by clarifying the relationship between the cardiac shadow of the chest X-ray image and the short axis of the heart. Presently, a standardization protocol for cardiac MRI examination has been published by the Society of Cardiovascular Magnetic Resonance (SCMR)⁹⁾. According to this protocol, the scout images of the body axis of the axial, coronal, and lateral views are first examined to assess the position of the heart. Thereafter, the image sections of the HLA and VLA are set by acquiring a cross-sectional image across the body axis covering the entire chest. This protocol consumes considerable examination and breath-hold time for obtaining the short-axis image, which can be painful for the patient. In this study, the angles of the outermost edges of the third and fourth bows of the cardiac shadow in the XP frontal view were used as the determining index of the angle of the left ventricle. The third bow of the cardiac shadow shows the left atrium from the anatomical positional relationship and the fourth bow of the cardiac shadow shows the left ventricle¹⁰⁾. Therefore, we could estimate the possibility of predicting the short axis of the heart from the cardiac shadow by estimating that the extracardiac lateral side is the angle formed by the left atrium and the left ventricle.

Several outliers are seen in the relation between the short-axis supposed angle α and the cardiac short-axis angle A. These cases corresponded to patients with dilated cardiomyopathy, cardiac tumor, and pericardial effusion, and they are believed to be due to the change in the cardiac shadow in the X-ray frontal image.

Furthermore, in the XP lateral image, the point at the back of the cardiac shadow is used as the indicator, which can be determined on the position of the left atrium and on the

image. This index can be measured without being affected by the cardiac shadow even in the above-mentioned case; therefore, it can be concluded that a very strong correlation was obtained.

We also evaluated the intra- and inter-reproducibility to assess the reliability of these analyses. We could confirm high measurement reliability in each analysis. The inter-observer reproducibility in the short-axis supposed angle α of the XP frontal image was less than the maximum reproducibility. This may be due to a slight mismatch between analysis of the starting point and ending point positions of the cardiac shadow in the third and fourth bows, which are the measurement indexes. However, the analysis method is considered very reliable because the mean difference between each observer was -1.75 ± 3.85 degrees and the ICC was 0.82 from the statistical evaluation. This is despite the fact that the definitions of the starting points of the third bow and the fourth bow were ambiguous, as the measurement part uses a clearly identifiable index as the outer side edge.

With the proposed method, it is possible to obtain a short-axis image without HLA and VLA imaging. Therefore, it is understood that it is possible to drastically reduce the examination time and number of breath-holds until the acquisition of the short-axis image. In the conventional method, the examination time until the acquisition of the short-axis image varied widely (Fig.6). This may be because of the necessity to examine the localizer multiple times and because of the variation in the operator settings. On the other hand, the operator-induced variation in the examination time in the new method remarkably decreased. Moreover, the duration from the imaging of the localizer until the imaging of the short-axis image is minimized, and the setting time for the short-axis image is reduced. Because the angle of the imaging section in the new method is derived by the

shape of the heart of the subject, almost no change in the imaging cross section occurs due to the difference in the operator. Therefore, even if a follow-up examination is required, it is possible to provide images with high repeatability of past short-axis cross sections of the heart. As an additional study, the differences in the imaging angle in the coronal and sagittal sections in cardiac MRI images with respect to the body axis when imaging with the new method and the conventional method were compared. The difference in the angle in the coronal section was $90.8 \pm 3.5^\circ$, and that in the sagittal section was $91.0 \pm 3.7^\circ$, which indicates that approximately the same angle was obtained in each method. The results of the visual evaluation suggested that there was no influence of this angle difference. In addition, the new method has the ability to image the VLA and HLA after obtaining the short-axis image. In the conventional method, the short-axis image is obtained after imaging the VLA and HLA. However, in this new method, it is possible to freely determine the imaging section after operating the localizer.

Several comparable research reports have reported techniques for detecting the short axis of the heart. Nitta, et al.¹¹⁾ published an application technology to detect the cardiac reference cross section using the body-axis transverse plane covering the entire heart. Clare E. Jackson, et al.¹²⁾ estimated the angle of the cardiac short axis using the threshold of the signal value of the image. However, these prior studies used special application software or algorithms, and have the disadvantage that it is difficult to easily adopt these techniques. Also, in recent years, compressed sensing technology has been noted as a high-speed MRI imaging technology¹³⁾.

Compressed sensing refers to a group of methods for accelerated MR data acquisition based on semi-random, incomplete sampling of k-space. A final image is created through an iterative optimization process using non-

Fourier transformation and thresholding of intermediately reconstructed images. Recently, some MRI devices can use compressed sensing technology and it has ability to reduce the imaging time significantly. However, it is still in the development stage and there are a lot of MRI devices without this technology. In this research, we established a method to estimate the short-axis cross section without special application software or complicated algorithms. This will encourage its adoption in more facilities.

We need to state the limitations of this research. First, because this is a cross-sectional study and does not have the concept of elapsed time, it does not consider the change in the medical condition over time. Therefore, the proposed method may be unusable if there is a sudden change in the medical condition during the period between cardiac MRI and chest X-ray imaging.

Next, a difference in the examination positions arises, as the chest X-ray is taken in the standing position whereas the cardiac CT is taken in the supine position. Although the relationships between these images were statistically strongly correlated in this study, it is necessary to pay attention to the difference in the examination positions, as it has been reported that a change in the examination position affects the visualization of the cardiac shadow in the chest X-ray image¹⁴). Nevertheless, the new method of imaging proposed in this study makes it possible to set a short-axis cross section by using the outermost edges of the heart at the time of cardiac MRI. Therefore, it would be unnecessary to consider the examination position.

At last, there is a difference of the type of participants between CCTA and MRI in this study. While CT scans often predominantly complained of coronary artery disease, MRI scans often targeted patients with cardiomyopathy or arrhythmias. Unfortunately,

all participants who underwent MRI in this study were normal volunteers. This must be considered as a limitation of this study. However, we believe that this can be useable for more cases in this new method because the present study indicate that the indices of the cardiac short axis and cardiac shadow are almost same unless affected by a cardiac tumor or the like.

5. Conclusion

In this study, we devised a method to image the cardiac short axis without VLA and HLA. It was demonstrated that the new method could shorten the examination and breath-hold time of the patient. In addition, it provides highly reproducible images irrespective of the operator-induced variation.

Acknowledgments

The authors are grateful to all staff of the Department of Radiological Technology, Showa University Hospital, for their cooperation in this study. This manuscript was partly supported by Akiyoshi Ohtsuka Fellowship of the Japanese Society of Radiological Technology for improvement in English expression of a draft version of the manuscript. We would like to thank Editage (www.editage.jp) for English language editing.

Funding: No funding was received for this study

Compliance with Ethical Standards: All procedures performed in the study that involved human participants were in accordance with the ethical standards of the Ethics Committee at the Showa University School of Medicine and with the 1964 Helsinki declaration and its later amendments or comparable ethical standards. As an animal rights disclosure statement, this article does not contain any studies with animals performed by

any of the authors.

Informed Consent: Informed consent was obtained from all individual participants included in the study.

Conflicts of Interest: The authors declare that they have no conflict of interest.

References

- 1) Kwong RY, et al.: Impact of unrecognized myocardial scar detected by cardiac magnetic resonance imaging on event-free survival in patients presenting with signs or symptoms of coronary artery disease. *Circulation*, 113: 2733-43, 2006.
- 2) Lund GK, et al.: Prediction of left ventricular remodeling and analysis of infarct resorption in patients with reperfused myocardial infarcts by using contrast-enhanced MR imaging. *Radiology*, 245: 95-102, 2007.
- 3) Larose E, et al.: Right ventricular dysfunction assessed by cardiovascular magnetic resonance imaging predicts poor prognosis late after myocardial infarction. *J. Am. Coll. Cardiol.*, 49: 855-62, 2007.
- 4) Ebeling Barbier C, et al.: Clinically unrecognized myocardial infarction detected at MR imaging may not be associated with atherosclerosis. *Radiology*, 245: 103-10, 2007.
- 5) Schwitter J, et al.: MR-IMPACT: comparison of perfusion-cardiac magnetic resonance with single-photon emission computed tomography for the detection of coronary artery disease in a multicentre, multivendor, randomized trial. *Eur. Heart J.*, 29: 480-9, 2008.
- 6) Niemann PS, et al.: Anatomically oriented right ventricular volume measurements with dynamic three-dimensional echocardiography validated by 3-Tesla magnetic resonance imaging. *J. Am. Coll. Cardiol.*, 50: 1668-76, 2007.
- 7) Sakuma H, et al.: Evaluation of left ventricular volume and mass with breath-hold cine MR imaging. *Radiology*, 188: 377-80, 1993.
- 8) Grothues F, et al.: Comparison of interstudy reproducibility of cardiovascular magnetic resonance with two-dimensional echocardiography in normal subjects and in patients with heart failure or left ventricular hypertrophy. *Am. J. Cardiol.*, 90: 29-34, 2002.
- 9) Kramer CM, et al.: Standardized cardiovascular magnetic resonance (CMR) protocols 2013 update. *J. Cardiovasc. Magn. Reson.*, 15: 91, 2013.
- 10) Anderson RH, et al.: Cardiac anatomy revisited. *J. Anat.*, 205: 159-77, 2004.
- 11) Nitta S, et al.: Automatic slice alignment method for cardiac magnetic resonance imaging. *MAGMA*, 26: 451-61, 2013.
- 12) Jackson CE, et al.: Computerized planning of the acquisition of cardiac MR images. *Comput. Med. Imaging Graph.*, 28: 411-8, 2004.
- 13) Lustig M, et al.: Compressed Sensing MRI. *IEEE Signal Processing Magazine*, 25: 72-82, 2008.
- 14) Funahiki T: Adaptation and limitation of simple X-ray examination. *Medicina*, 54: 626-9, 2017. (in Japanese)

Calculation of optimal TI associated with temperature changes of the water using Synthetic MRI assuming postmortem brain FLAIR imaging

OKAWA Ryuya^{1),2)}, YASUI Go¹⁾, KANAI Yoshihiro¹⁾, MIHARA Ban³⁾, HAYASHI Norio⁴⁾

1) Department of diagnostic imaging, Radiological Technologist, Mihara Memorial Hospital

2) Graduate School of Radiological Technology, Gunma Prefectural College of Health Sciences

3) Department of Neurology, Doctor, Mihara Memorial Hospital

4) Department of Radiological Technology, Associate Professor, Gunma Prefectural College of Health Sciences

Note: This paper is secondary publication, the first paper was published in the JART, vol. 68 no. 820: 33-39, 2021.

Key words: magnetic resonance imaging (MRI), Synthetic MRI, Autopsy imaging (Ai), fluid attenuated inversion recovery (FLAIR), Inversion Time (TI)

[Abstract]

In postmortem brain fluid-attenuated inversion recovery (FLAIR) imaging, we sometimes encounter failure of cerebrospinal fluid (CSF) signal suppression. The reason for this is because the T_1 value of CSF begins to fluctuate along with the decreases in the body temperature after death, which prevents one from setting the appropriate TI setting. Therefore, it is necessary to measure the T_1 value corresponding to the temperature change of CSF and calculate the optimal inversion time (TI). In this study, we conducted a phantom experiment to investigate the usefulness of synthetic magnetic resonance imaging (MRI) for calculating the optimal TI corresponding to CSF temperature change. Using the optimal TI setting enabled us to obtain FLAIR images with sufficient water signal suppression. We considered that synthetic MRI is a useful method for measuring T_1 values and calculating the optimal TI corresponding to change in water temperature.

Introduction

The brain fluid attenuated inversion recovery (FLAIR) imaging method suppresses cerebrospinal fluid (CSF) signals using the inversion recovery (IR) pulse and adjusts the inversion time (TI) parameter¹⁾. In a spin-echo (SE)-based sequence, if a 180-degree inverted pulse is irradiated first before irradiating a 90-degree pulse, and a long TI is set, then CSF signals will continue to pass through their null point even though T_1 of signals from the brain and other normal tissues have adequately recovered; therefore, if signals are collected at this point, images can be taken using suppressed CSF signals^{2,3)}. Hence, the brain FLAIR imaging method has high sensitivity to signal changes in a wide variety of lesions, such as around the ventricle in demyelinating and inflammatory diseases, and it is an indispensable imaging sequence for MRI examination of the brain⁴⁻⁶⁾.

However, during clinical imaging—especially “Autopsy imaging (Ai)” —the brain FLAIR imaging method may fail to suppress CSF signals. This is because the temperature of CSF falls owing to the changes that occur in the body after death, causing the T_1 value to fluctuate and preventing the appropriate TI from being set⁷⁻¹¹⁾.

On the other hand, a new relaxation time measurement method has emerged in recent years called synthetic MRI. In it, a pulse sequence called “quantification of relaxation times and proton density by multi-echo acquisition of saturation recovery using turbo spin-echo readout” (QRAPMASTER) is used. Using multi-delay, multi-echo data collection, eight types of data are collected from each slice, comprising four types of saturation delay and two types of echo time (TE). The T_1 relaxation curve is then estimated from the image of the four kinds of saturation delay, and the T_1 value

and proton density (PD) are calculated for each pixel. Similarly, the T_2 value is calculated for each pixel from the image of the two kinds of TE, and multiple contrast images are created under arbitrary conditions from the obtained quantitative value¹²⁻¹⁵). Furthermore, by using a dedicated application and setting the region of interest (ROI) at any part of the selected slice section, it is possible to gauge the quantitative value of relaxation time. This has drawn attention as an effective technology for TI calculation, because the T_1 value can be easily obtained^{16, 17}).

In this study, we focused on the capabilities of the synthetic MRI, which can measure relaxation time quickly and easily at any location. Using these capabilities, we explored the efficacy of the synthetic MRI in suppressing CSF signals for postmortem brain FLAIR imaging by calculating the optimal TI for the temperature change and comparing the FLAIR images—captured using the clinical TI—to images captured using the optimal TI.

1. Methods

1-1 Equipment used and fabrication of the phantom

The MR device we used was the Discovery MR750W 3.0 Tesla scanner (General Electric Healthcare Medical Systems Corporation, Milwaukee, Wisconsin, USA); the receiver coil was an Anterior Array coil; and the synthetic MRI software application was Magnetic Resonance Image Compilation (MAGiC), which came with the equipment. The image analysis software we used was ImageJ (National Institutes of Health, Bethesda, MD, USA, <http://rsb.info.nih.gov/ij/>). To fabricate the phantom, we used an MRI imaging container (MRI phantom 90-401 type, Nikko Fines Industry Corporation, Japan), a plastic bottle for MRI measurement (inner diameter 19 mm), and pure water (Super Desaliner, Organo Corporation, Japan). For visual evaluation, we used a display monitor

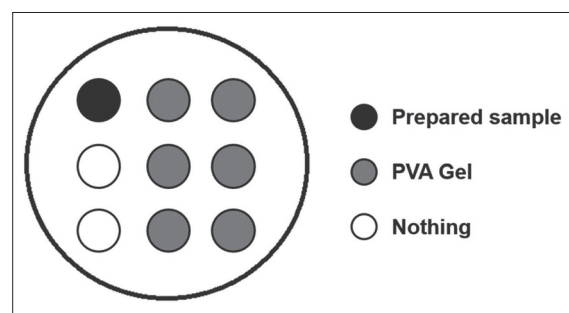


Fig.1 Placement of prepared sample on MRI phantom.

for medical image display (Exa Vision PLUS, Zio Soft Corporation, Tokyo, Japan); the statistical analysis software we used was Easy R (EZR).

Six samples simulating CSF were prepared by changing the temperature of pure water from 10°C to 35°C in 5°C increments, and enclosing it in a plastic bottle for MRI measurement. The temperature of pure water was measured with a digital thermometer (A&D Corporation, Japan) and adjusted so that it was the target temperature. In addition, for each imaging session, one of the prepared samples was placed in the upper left pocket of the MRI phantom (Fig.1).

1-2 Obtaining FLAIR images

1-2-1 T_1 value measurement by Synthetic MRI

Synthetic MRI imaging was carried out for each prepared sample, and the T_1 value was gauged using the dedicated software application. The synthetic MRI imaging conditions were as follows: repetition time (TR)=4,430 ms, echo time (TE)=21.4/106.8 ms, band width (BW)=22.73 kHz, matrix=320×224, slice thickness=5 mm, number of signals averaged (NSA)=1, field of view (FOV)=230 mm, RFOV=100%, echo train length (ETL)=16, asset factor=2, number of slices=23, TI=12.26 ms (only the shortest value is displayed due to device function limitations), scan time=4 m 34 s. To account for the influence of temperature changes due to the time elapsed during imaging and the heat absorption rate (specific ab-

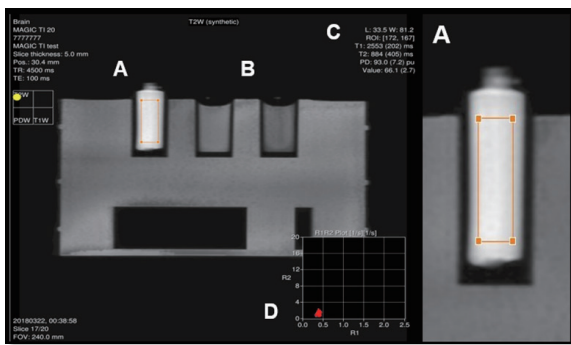


Fig.2 Console screen with application of Synthetic MRI expanded.

- (A) Prepared sample
- (B) PVA gel built into the Phantom
- (C) Quantitative value of relaxation for prepared sample
- (D) R₁ and R₂ maps for prepared sample

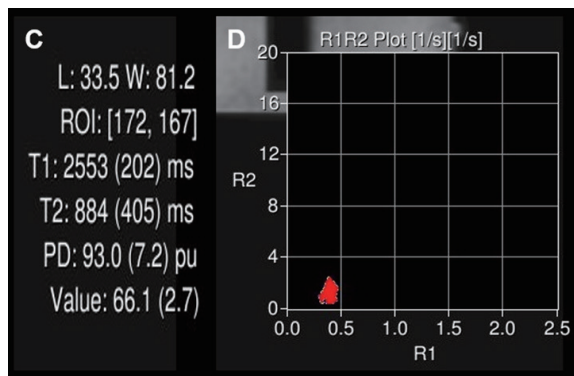


Fig.3 This figure is an enlarged view of parts (C) and (D) in the Figure 2.

sorption rate=SAR), the temperature of each prepared sample was measured after synthetic MRI imaging. Fig.2 shows the imaged MRI phantom image expanded on a console screen using the synthetic MRI application. By setting a rectangular ROI of any size in the center of the sample, quantitative values of relaxation time (T₁, T₂) and R₁ and R₂ maps were obtained in real time corresponding to the position where the ROI was set (Fig.3).

1-2-2 Calculating the optimal TI

The T₁ value of each prepared sample, measured using a synthetic MRI function, was substituted into a simple formula (1), and the appropriate TI was calculated. The optimal TI computed for each prepared sample is a value within the change between the set temperature

of the sample and the temperature measured after synthetic MRI imaging.

$$TI = T_1 \text{ Value} \times 0.693 \dots\dots\dots (1)$$

1-2-3 FLAIR imaging

In order to confirm whether the T₁ value of each sample—measured using a synthetic MRI function—was a quantitative value corresponding to temperature change, two types of phantom images were taken: a FLAIR image with clinical TI (2,700 ms) and a FLAIR image with optimal TI. The imaging conditions for the FLAIR images were as follows: TR=12,000 ms, TE=140 ms, BW=35.71 kHz, matrix=320×224, slice thickness=5 mm, NSA=1, FOV=230 mm, RFOV=100%, flip angle=160°, ETL=21, asset factor=2, number of slices=20, TI=1,600, 1,710, 1,800, 1,990, 2,160 ms (scan time=3 m 49 s), 2,400, 2,700 ms (scan time=2 m 36 s).

1-3 Evaluation of the FLAIR images

1-3-1 Visual evaluation

Visual evaluation was carried out to compare the degree of signal suppression in the FLAIR images of the sample portions between those imaged with the TI set to the clinical value and those imaged with the TI set to the optimal value. The observers were eight radiological technologists with between 3 and 40 years of clinical experience working with MRI testing (male to female ratio=6:2, mean age=36.6 years). We obtained written informed consent to publish the results obtained through visual evaluation. The evaluation method involved randomly displaying on the monitor the 12 FLAIR images of the samples one at a time, with the imaging parameters hidden, and the observers giving each image a score on the following 5-point scale:

- 5: the signal has been suppressed
- 4: the signal has been almost suppressed
- 3: neither / unable to discern
- 2: the signal has hardly been suppressed
- 1: the signal is not suppressed

Reference images were presented to the observers in advance, and the scoring method of evaluation was sufficiently explained and practiced. The average and standard deviation (SD) of the 12 FLAIR images were calculated from the scores assigned by 8 observers. To compare whether there was a difference between the average score values of the two types of FLAIR images, those with clinical TI and those with optimal TI, statistical analysis was carried out at a significance level of 5% using Wilcoxon's signed rank sum test to compare the two corresponding groups¹⁸⁾.

1-3-2 Physical evaluation

Signal intensity (SI) and SD were measured for each FLAIR image captured with the TI set to the clinical value and the TI set to the optimal value. The measurement points were set to the sample and a 14 mm diameter ROI at the center of the nearest adjacent the polyvinyl alcohol (PVA) gel built into the MRI phantom (Fig.4). Based on the measured SI and SD, the signal-to-noise ratio (SNR) of each prepared sample, and the contrast-to-noise ratio (CNR) between the prepared sample and the PVA gel, were calculated with equations (2) and (3). It has previously been reported that when calculating SNR, the difference method is the most correlated with the theoretical value¹⁹⁾. How-

ever, in this study, due to the temperature control of the specimens, it was not possible to take two consecutive images under completely identical environmental conditions. Therefore, we used the same region of interest method instead of the difference method¹⁹⁻²¹⁾. For the CNR calculation, we employed the EU proposed method²²⁾. Here, SIa and SIb are the average signal values in the circular ROIs set in the prepared sample and PVA gel, and SDa and SDb are standard deviations in ROI, set the same way as SIa and SIb .

$$SNR = SIa/SDa \dots\dots\dots (2)$$

$$CNR = |(SIa - SIb)|/(SDa^2 + SDb^2)^{\frac{1}{2}} \dots\dots (3)$$

2. Results

2-1 T₁ value and the optimal TI of each sample

Table 1, Fig.5, and Fig.6 show the T₁ value and calculated optimal TI of each sample, as well as the relationship to temperature, determined using synthetic MRI. The T₁ value and calculated optimal TI of each sample is a value within the change between the set temperature of the sample and the temperature measured after synthetic MRI imaging. The T₁ value of each sample measured via synthetic MRI declined as the temperature falls below 35°C, which is close to body temperature. Like the T₁ value, the calculated optimal TI also showed smaller values as the temperature dropped.

2-2 Visual evaluation of the FLAIR images

Fig.7 depicts the FLAIR images of each sample, captured with the IT set to the clinical value and to the optimal value. For all images, window width (WW) and window level (WL) are constant. In the FLAIR images with the TI set to the clinical value, the water signals were suppressed at temperatures close to the temperature of a living body, but the lower the temperature, the more defects in suppression

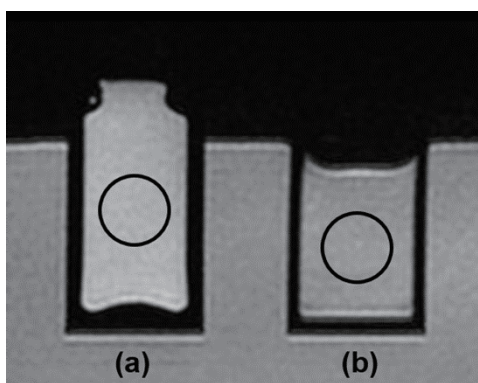


Fig.4 Placement of ROI in physical evaluation.

- (a) Prepared sample
- (b) PVA gel (water content rate: 80%, gadolinium concentration: 0.3 mmol)

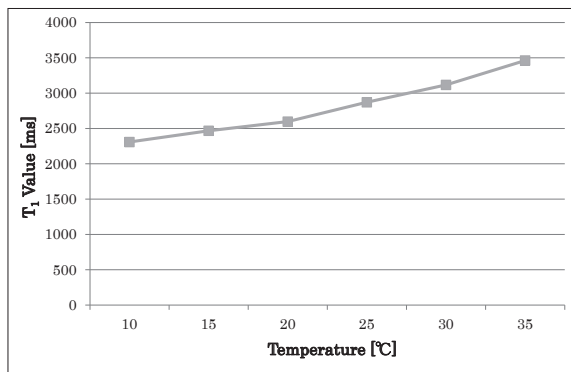


Fig.5 Relationship between T₁ value that measured using the function of Synthetic MRI and temperature of each prepared sample.

The T₁ value for each sample has smaller values in cases where temperatures were lower, and higher values in the case of higher temperatures.

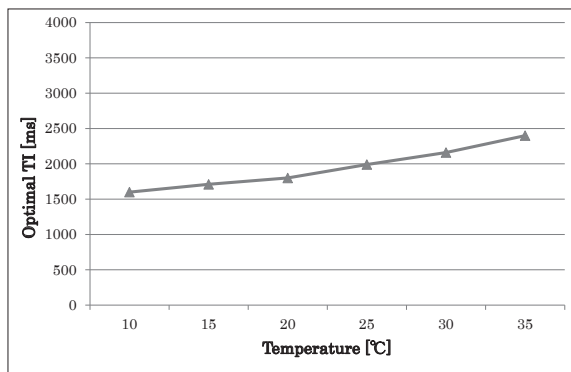


Fig.6 Relationship between optimal TI that calculated from measured T₁ value and temperature of each prepared sample.

The optimal TI for each sample has smaller values in cases where temperatures were lower, and higher values in the case of higher temperatures.

occurred. On the other hand, in the FLAIR images with the TI set to the optimal value, water signals were suppressed in all samples. Table 2 portrays the means and SD of the visual evaluation scores, the differences in the mean scores, and the test results. The average score for FLAIR images with the TI set to the clinical value was 2 or less at all temperatures, whereas the average score for FLAIR images with the TI set to the optimal value was 4 or higher. The difference between the average scores for the two TI values was 3 or higher at all temperatures, and a significant difference was observed

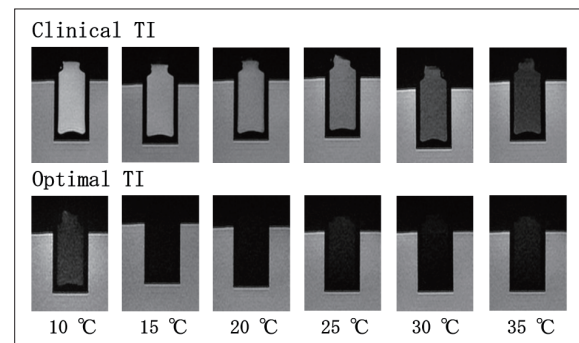


Fig.7 The two types of FLAIR image for each prepared sample.

In the upper half, the FLAIR images obtained with the clinical TI setting demonstrate failure of water signal suppression. In the bottom half, the FLAIR images obtained with the optimal TI setting show decreased signal intensity for all samples, and there is sufficient water signal suppression.

Table 1 Relationship between the temperature of each prepared sample after imaging and the measured T₁ value and the calculated optimal TI

Preset temperature [°C]	10	15	20	25	30	35
Temperature after imaging [°C]	12.6	16.2	20.7	24.7	28.6	33.2
T ₁ value [ms]	2,309	2,468	2,597	2,872	3,117	3,463
Optimal TI [ms]	1,600	1,710	1,800	1,990	2,160	2,400

Table 2 Average score and standard deviation of visual evaluation results of clinical TI and optimal TI with the average score differences

Temperature [°C]	10	15	20	25	30	35
Clinical TI	1.00 ± 0.00	1.13 ± 0.33	1.13 ± 0.33	1.00 ± 0.00	1.00 ± 0.00	1.38 ± 0.48
Optimal TI	4.13 ± 0.33	5.00 ± 0.00	5.00 ± 0.00	4.63 ± 0.48	4.88 ± 0.33	4.38 ± 0.48
Differences	3.13	3.87	3.87	3.63	3.88	3.00
Wilcoxon rank sum test	*	*	*	*	*	*

* : p<0.05

due to statistical analysis ($p < 0.05$).

2-3 Physical evaluation of the FLAIR images

Table 3 and Fig.8 display the SNR calculation outcomes of the FLAIR images of each sample, captured with the TI set to the clinical value and to the optimal value. In the FLAIR images with the TI set to the clinical value, the SNR of each sample exhibits higher values when the temperature is lower, whereas in the optimal TI FLAIR images, the SNR of each sample indicates constant values regardless of temperature change. Also, comparing the SNR values of both denotes that for all samples, setting the TI to the optimal value produces lower values, and the difference increases as the temperature falls.

Table 4 and Fig.9 present the findings of CNR

calculation between the sample and the PVA gel at each temperature. The CNR of each sample in the FLAIR images with optimal TI revealed a large value, regardless of the change in temperature. Moreover, compared with the CNR of each sample in the FLAIR images with clinical TI, setting the optimal TI demonstrated a higher value at all temperatures.

3. Discussion

Previous studies indicate that fluid T_1 and T_2 values are temperature dependent, the idea being that the magnetic relaxation phenomenon is a transition in which the dipole-dipole interaction is shaken by molecular motion^{7, 23}. Therefore, the postmortem FLAIR imaging occurs the failure of CSF signal suppression be-

Table 3 The results of SNR calculations for the two types of FLAIR images

Temperature [°C]	SNR	
	Clinical TI	Optimal TI
10	48.5	8.15
15	38.3	5.47
20	33.2	4.81
25	25.6	4.61
30	16.2	5.01
35	11.8	4.90

Table 4 The results of CNR calculations for the two types of FLAIR images

Temperature [°C]	CNR	
	Clinical TI	Optimal TI
10	4.38	27.6
15	1.30	28.2
20	2.76	30.8
25	7.92	27.4
30	13.1	31.0
35	16.7	28.6

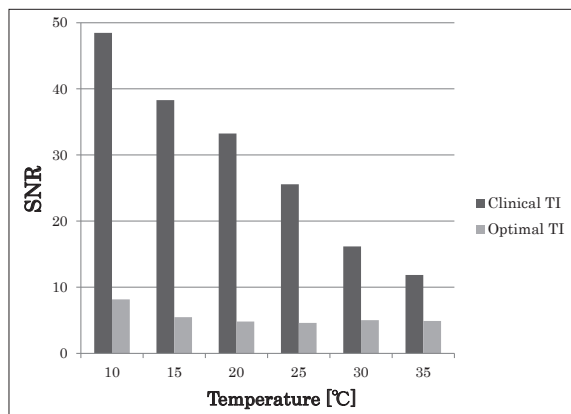


Fig.8 The results of SNR calculations for the two types of FLAIR images.

The SNR values were smaller for the FLAIR images obtained with optimal TI setting than for those obtained with the clinical TI setting, for all temperatures.

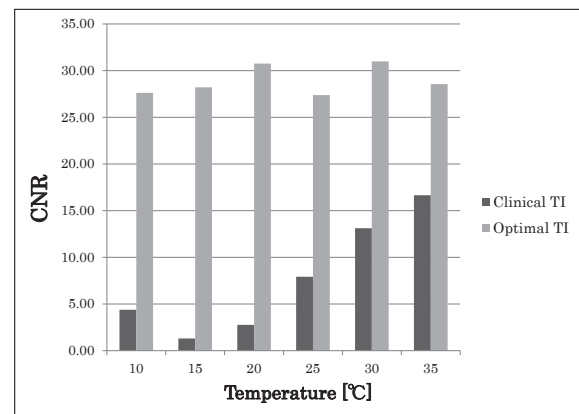


Fig.9 The results of CNR calculations for the two types of FLAIR images.

The CNR values were higher for the FLAIR images obtained with optimal TI setting than for those obtained with the clinical TI setting, for all temperatures.

cause the temperature of the CSF decreases as the body temperature decreases after death, and the T_1 of the CSF shortens. Tofs et al. refer to these images as cold FLAIR and highlight the importance of setting an optimal TI for post-mortem FLAIR imaging of the brain ¹¹). The present study has also confirmed similar information to previous findings regarding the temperature dependence of fluid T_1 values. Results 2-1 denote that the T_1 value of water at 35°C, near biological body temperature, is about 3,500 ms, and because this falls by about 500 ms for every 10 degrees drop in temperature, the T_1 value of water is greatly affected by temperature changes. In addition, since the T_1 value of water is lower at lower temperatures, T_1 levels in CSF can be predicted to decline in the brain of a cadaver as well due to a decrease in body temperature after death. Furthermore, the difference between the optimal TI, when the temperature of water is 35°C, and the optimal TI at 10°C, is 800ms, and since the TI set during postmortem FLAIR imaging of the brain will decrease with the decline in T_1 value, it is crucial to calculate the optimal TI for temperature changes in CSF.

In visual evaluation, the average score for FLAIR imaging with the TI set to the optimal value was 4 or higher, and the difference in the average score for FLAIR images with the TI set to the clinical value compared to those with the TI set to the optimal value was 3 or higher at all temperatures. The SNR in FLAIR images with the TI set to the optimal value was also lower in all samples compared to FLAIR images with the TI set to the clinical value; the CNR values were also high, suggesting that the water signals were suppressed properly by setting the appropriate TI and that clear FLAIR images were obtained. In other words, using the synthetic MRI function makes it possible to quantify fluctuations in the T_1 value due to the temperature change of water and to calculate the optimal TI, and is an effective technique for improving defects in the suppression of CSF

signals arising in postmortem FLAIR imaging of the brain. Conventionally and in recent years, the IR method has often been used to measure T_1 values. However, measuring the T_1 value of water by the IR method requires a very long TR setting, which leads to the problems of inaccurate quantification due to the temperature change of CSF during imaging and a significant extension of the imaging time ²⁴). Therefore, the IR method was unrealistic when quantifying substances with long T_1 values such as CSF. The above suggests that synthetic MRI is effective at measuring T_1 values corresponding to changes in the temperature of CSF and calculating optimal TI.

In this study, we focused on synthetic MRI functions that can measure relaxation time quickly and easily at any location, and through phantom experiments, we examined the efficacy of synthetic MRI in calculating the optimal TI with the temperature change of water. The results confirmed that it is possible to use synthetic MRI to measure T_1 values easily and appropriately and to calculate optimal TI. Previous studies indicate that the measurement value of relaxation time in CSF varies depending on imaging conditions ²⁵). Hence, it is necessary to examine whether synthetic MRI imaging conditions affect T_1 value measurements carried out for TI calculation, and to research the optimal imaging protocol. In the future, it will be necessary to perform postmortem brain MRI imaging on cadavers using the Synthetic MRI to obtain results similar to those obtained in this study and to investigate whether it is possible to optimize the FLAIR imaging method under the influence of postmortem temperature decrease.

4. Conclusion

In this study, we have clarified the efficacy of synthetic MRI in the measurement of T_1 values with changes to temperature of water and in the calculation of optimal TI. Moreover, we

suggest that this may improve defects in the suppression of CSF signals that occur in post-mortem brain FLAIR imaging.

Acknowledgments

I would like to express my heartfelt gratitude for the guidance and cooperation of many people in this research. A part of this paper was presented at the 34th Japan Conference of Japanese Radiological Technologists in Shimonoseki, Japan, in 2018.

References

- 1) Joseph V. Hajnal, David J. Bryant, et al.: Use of Fluid-Attenuated Inversion Recovery (FLAIR) Pulse Sequences in MRI of the Brain. *Journal of Computer Assisted Tomography*, 16(6), 841-844, 1992.
- 2) Aoki S, et al.: A Key to Brain MRI Interpretation. 17-21, Gakken Medical Shujunsha Co.,Ltd, 1998.
- 3) Kasai T, et al.: Imaging Technology for Magnetic Resonance. 136-137, Ohmsha Co.,Ltd, 2001.
- 4) Beatrice De Coene, Joseph V. Hajnal, et al.: MR of the Brain Using Fluid-Attenuated Inversion Recovery (FLAIR) Pulse Sequences. *American Journal of Neuroradiology*, 13(6), 1555-1564, 1992.
- 5) Susan J. white, Joseph V. Hajnal, et al.: Use of Fluid-Attenuated Inversion Recovery Pulse Sequences for Imaging the Spinal Cord. *Magn Reson Med*, 28, 153-162, 1992.
- 6) Valerie L. Stevenson, et al.: Imaging of the spinal cord and brain in multiple sclerosis: a comparative study between fast flair and fast spin echo. *Journal of Neurology*, 224, 119-124, 1997.
- 7) Kobayashi T, Isobe T, et al.: Special Edition on MRI No.2 Understanding AI - Signal Changes in MRI. *Journal of JART*, 58, 40-47, 2011.
- 8) Kobayashi T.: Optimization of inversion time for post-mortem short-tau inversion recovery (STIR) MR imaging. Ph.D. Dissertation, Ibaraki Prefectural University of Health Sciences, 8-10, 51-54, 2014.
- 9) Kobayashi T, Shiotani S, et al.: Characteristic signal intensity changes on postmortem magnetic resonance imaging of the brain. *Jpn J Radiol*, 28, 8-14, 2010.
- 10) Kobayashi T, Isobe T, et al.: Postmortem magnetic resonance imaging dealing with low temperature objects. *Magn Reson Med*, 9, 101-108, 2010.
- 11) Tofts PS, Jackson JS, et al.: Imaging cadavers: cold FLAIR and noninvasive brain thermometry using CSF diffusion. *Magn Reson Med*, 59, 190-195, 2008.
- 12) Warntjes JB, Leinhard OD, et al.: Rapid magnetic resonance quantification on the brain: optimization for clinical usage, *Magn Reson Med*, 60(2), 320-329, 2008.
- 13) Hagiwara A, Hori M, et al.: Clinical Applications and Future Prospects of Synthetic MRI. *INNERVISION*, 31(9), 13-15, 2016.
- 14) Blystad I, Warntjes JB, et al.: Synthetic MRI of the brain in a clinical setting. *Acta Radiol*, 53(10), 1158-1163, 2012.
- 15) Asano K.: MAGiC technology and its potential. *A Monthly Journal of Medical Imaging and Information*, 47(14), 142-147, 2015.
- 16) Krauss W, Gunnarsson M, et al.: Accuracy and reproducibility of a quantitative magnetic resonance imaging method for concurrent measurements of tissue relaxation times and proton density. *Magn Reson Imaging*, 33(5), 584-591, 2015.
- 17) Horita M, Hagiwara A, et al.: Quantitative of Synthetic MRI. *INNERVISION*, 32(9), 5-7, 2017.
- 18) Kanda Y.: Investigation of the freely available easy-to-use software 'EZR' for medical statistics. *Bone Marrow Transplantation*, 48, 452-458, 2013.
- 19) Ogura A, Miyai A, et al.: Accuracy of Signal-to-noise Ratio Measurement Method for Magnetic Resonance Images. *Journal of JSRT*, 59(4), 508-513, 2003.
- 20) Ogura A, Miyai T, et al.: Method of SNR Determination Using Clinical Images. *Journal of JSRT*, 63(9), 1099-1104, 2007.
- 21) Wada Y.: Examination about the relationship between image scan sequence and SNR measuring method. *Journal of JART*, 64, 24-29, 2017.
- 22) Wada Y, Hara T, et al.: Basic Assessment of the CNR Measurement Method of MRI System in Phantom - Suggestion for Improvement in the CNR Evaluation Method -. *Journal of JSRT*, 64(2), 268-276, 2008.
- 23) Bloembergen N, et al.: Relaxation effects in nuclear magnetic resonance absorption. *Phys Rev*, 73, 679-712, 1948.
- 24) Hayashi N, Ujita K, et al.: Development of an Optimizing Program of Scanning Parameters for Double Inversion Recovery MRI. *Journal of JSRT*, 71(6), 512-519, 2015.
- 25) Konta N, Shibukawa S, et al.: The Effect of Scan Parameters on the Synthetic MRI. *Journal of JSRT*, 74(2), 117-123, 2018.

Trial of dose reduction of Digital Breast Tomosynthesis

HAYAKAWA Saki^{1), 2)}, SHINOHARA Norimitsu^{1), 2)}

1) Department of Radiological Technology, Faculty of Health Sciences, Gifu University of Medical Science

2) Master Course of Health and Medicine, Graduate School of Health and Medicine, Gifu University of Medical Science

Note: This paper is secondary publication, the first paper was published in the JART, vol. 68 no. 821: 17-22, 2021.

Key words: Digital Breast Tomosynthesis, Imaging Dose Reduction, Breast Cancer, Quality Control

[Abstract]

In recent years, mammography devices with digital breast tomosynthesis (DBT) technology have become widespread. In this study, which focuses on the overall image quality characteristics of DBT, we examined the possibility of dose reduction in slice images of reconstructed data (proc data). Low-contrast resolution and signal difference-to-noise ratio (SDNR) were measured based on EUREF (European Reference Organisation for Quality Assured Breast Screening and Diagnostic Services). The mAs value was based on 90 mAs close to the AEC auto mode. The SDNR limiting value was calculated by reducing the mAs value. The projection data did not achieve the required SDNR due to lower mAs value. Therefore, the auto mode setting was confirmed as 'good'. The proc data achieved the standard at 80 mAs, and it was considered possible to reduce the dose. It is necessary to confirm that the analysis software supports proc data.

1. Introduction

In recent years, mammography devices with digital breast tomosynthesis (DBT) technology have become widespread. DBT continuously or pulses X-rays to the breast from different angles in a single photograph, and multiple cross-sections can be obtained by reconstructing the image after shooting¹⁾.

In breast cancer screening in Japan, mammography examinations in which the breasts are pressed and pushed out are recommended. Mammography tests can depict fine lesions such as calcification with high resolution; however, there is a risk that the lesions will be hidden in the mammary glands²⁾. DBT has the advantage of reducing the influence of mammary gland overlap because multiple cross-sections can be obtained, and it is expected to be a useful technique for diagnosis³⁾. However, DBT is currently photographed in addition to mammography, with no insurance listing or establishment of essential scenes⁴⁾.

According to the classification of the Interna-

tional Commission on Radiological Protection (ICRP), the tissue weighting coefficient of the mammary gland is highest at 0.12, and it is an organ with high radiosensitivity⁵⁾. Normally, the diagnostic reference level (DRL) of mammography is as little as 2.4 mGy or less per direction photograph⁶⁾, and there is no need to worry about the definite effect if it is a normal dose or inspection frequency⁷⁾. However, DBT does not have a reference value for dose, and since it is left to the judgment of manufacturers and facilities⁴⁾, the establishment of performance evaluation standards and quality control procedures is urgently needed⁸⁾. In this study, we focus on the overall image quality characteristics of DBT, and examine the possibility of dose reduction in slice images of reconstructed data (proc data).

2. Method

In this study, *Peru ru™ La Plus*, manufactured by Canon Medical Systems Co., Ltd., was used as the DBT device. **Table 1** lists the speci-

Table 1 Specifications and reconfiguration of DBT equipment

item	specification
Conversion method · FPD	Direct conversion a-Se/TFT W/Ag, Al, Rh
Output pixel size (DBT)	85 μ m
Tomosynthesis oscillation angle	$\pm 7.5^\circ$
Tomosynthesis Shooting Time	—
Reconstruction method	Sequential approximation
X-Ray Tube Motion	Continuous
Tomosynthesis Number of Shots	17 shots

fications and reconfiguration methods for DBT equipment. Basic parts of the experiment, such as phantom placement and measurement position, were carried out based on the Protocol for the Quality Control of the Physical and Technical Aspects of Digital Breast Tomosynthesis Systems ver 1.03⁹⁾ (Protocol DBT) method published by EUREF (European Reference Organisation for Quality Assured Breast Screening and Diagnostic Services). The data used for analysis is measured using projection data (prj data) in Protocol DBT. However, in order to measure overall characteristics, the data is measured by sliced images (proc data) in this study. Moreover, prj data was also measured at the same time in order to verify the accuracy of the measurement.

This study consisted of two experiments. In Experiment 1, the signal difference to noise ratio (SDNR) was measured by the difference in sliced surfaces, as in a previous experiment. This reveals the effect of protocol DBT and aluminum arrangement on measured values. In Experiment 2, we attempted to reduce the dose using CDMAM phantom and SDNR.

2.1 Pre-experiment effect of slice plane differences on SDNR

First, the shooting conditions were determined. A 50 mm thick polymethylmethacrylate (PMMA) was placed on the breast support table, and the position of the compression pad-

Table 2 Shooting conditions on each slice surface

Target/Filter	Tube voltage (kV)	mAs
W/Ag	29	63
W/Ag	29	71
W/Ag	29	80
W/Ag	29	90

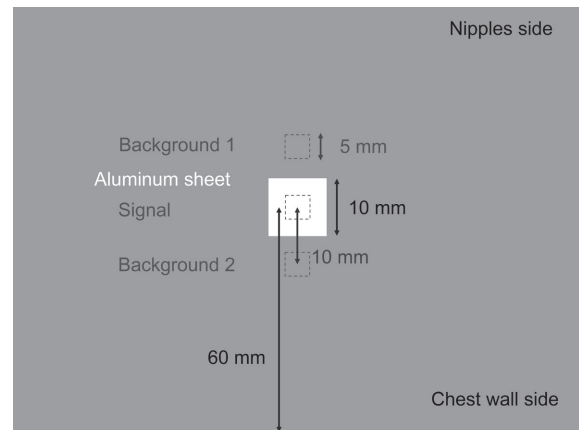


Fig.1 Aluminum sheet placement and measurement ROI for SDNR measurement

dle was set to 60 mm. Using the most commonly used auto-mode in clinical practice, the AEC was activated, and X-rays were irradiated. The shooting conditions obtained at that time were target W (tungsten), filter Ag (silver), tube voltage 29 kV, and mAs value of 87.7 mAs. The irradiation mode was set to manual, and the target filter and tube voltage were set in the same manner as in auto mode. The mAs value was 90 mAs, which is the closest mAs value exceeding the condition of auto mode. In this study, the mAs values were set to 63 mAs, 71 mAs, and 80 mAs based on the shooting conditions of the auto mode (Table 2), to try and reduce the dose.

SDNR aluminum sheet placement is shown in Fig.1. Aluminum sheets of 10 mm \times 10 mm were placed on PMMA at a position 60 mm from the chest wall side in the left and right centers. The PMMA thickness was constant at 50 mm, and the height (slice surface) of the aluminum sheet was changed from the breast support table in six stages: 5, 10, 15, 25, 35, and 45 mm. The pressure plate was placed at a position of 60 mm and photographed on each

slice surface under the conditions listed in **Table 2**.

The photographed image was measured using ImageJ_1.52a by setting an ROI of 5 mm × 5 mm. The pixel value (PV) and standard deviation (SD) were obtained from Equation 1, and the SDNR was calculated. PV (signal) is the average pixel value in the aluminum sheet, and PV (background) and SD (background) are the average values of the background pixels and standard deviation in the two ROIs.

$$SDNR = \frac{PV(signal) - PV(background)}{SD(background)} \quad \dots \text{Equation 1}$$

$$SD(\text{background}) = \frac{\sum_1^2 SD(ROI_n)}{2}$$

$$PV(\text{background}) = \frac{\sum_1^2 PV(ROI_n)}{2}$$

The images to be analyzed used prj data and proc data, and SDNR was calculated from each image.

2.2.1 Experiment Low contrast resolution measurement

CDMAM 3.4 phantoms were used to measure low-contrast resolution. It was attached to a grid-like square similar to a burger phantom. The signal is a gold disk whose diameter and thickness change logarithmically, and one is arranged in the center and four corners of the square separated area (**Fig.2**). The CDMAM phantom was placed at the center of the PMMA (thickness of 40 mm) according to Protocol DBT (**Fig.3**), and the pressure plate was placed at a position of 60 mm. **Table 2** was used as the shooting conditions, and 16 measurements were taken each time.

After shooting, CDMAM 3.4 Analyser 2.3.3 (Artinis) was used to calculate the values from each image before and after image processing.

The IQF_{inv} (inverse image quality figure) of each mAs value was obtained from Equation 2. Since IQF_{inv} increases with the improvement of image quality, it can be said that the higher the value of IQF_{inv} , the better the low-contrast res-

olution¹⁰.

$$IQF_{inv} = \frac{n}{\sum_{i=1}^n C_i \times D_{i,min}} \quad \dots \text{Equation 2}$$

C_i : gold disc thickness (μm)

$D_{i,min}$: the smallest diameter perceived in the column corresponding to a gold thickness C_i (mm)

n : Number of columns in the contrast field that can be identified

2.2.2 Experiment Measuring SDNR

As in the experiment in 2.1, SDNR was used to place a 10 mm × 10 mm aluminum sheet on PMMA at a position 60 mm from the chest wall side in the left and right centers. Protocol DBT places aluminum sheets at a height of 10 mm from the breast support table. However, in this study, aluminum sheets were placed at a height of 25 mm, which is the same position as the CDMAM phantom. The pressure plate was placed at 60 mm. **Table 2** was used as the shooting condition, and the average of the measured values was taken three times each as

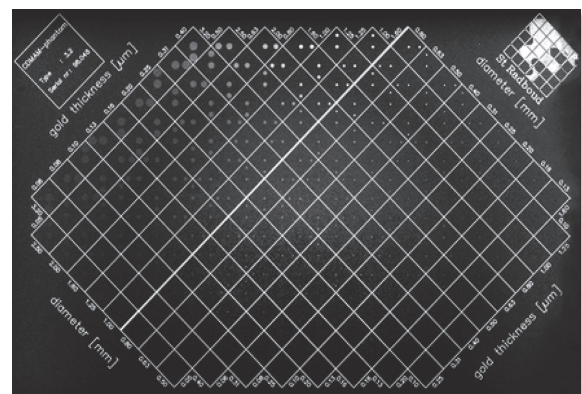


Fig.2 Overview of CDMAM 3.4 Phantom

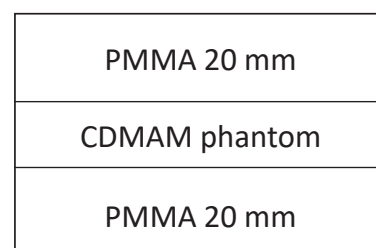


Fig.3 Geometric arrangement of CDMAM phantom (cross-sectional view)

SDNR. The analysis was carried out on prj and proc data images.

3. Results

3.1 Pre-experiment effect of slice plane differences on SDNR

Table 3 lists the measurement results of SDNR on each slice surface of the prj data. The farther away the slice surface is from the breast support stand, the lower the SDNR, and a drop of up to 5.9% was observed. However, there was no significant change in the SD or contrast.

Table 4 shows the measurement results of SDNR on each slice surface of proc data. At 5, 10, and 15 mm, the SDNR decreased slightly as it separated from the breast support table, and at 25, 35, and 45 mm, there was no significant change in SDNR due to the slice surface. SD increased as it was separated from the breast support table. The contrast decreased as it separated from the breast support table at 5, 10, and 15 mm, and there was no significant differ-

Table 3 SDNR (90 mAs) on each slice surface of prj data

Height (mm)	SD (bg)	contrast	SDNR	Difference (%)
5	13.6	28.8	2.12	100.5
10	13.2	27.9	2.12	100.0
15	13.6	27.9	2.05	96.7
25	13.2	27.3	2.06	97.5
35	13.5	27.1	2.01	94.8
45	13.6	27.0	1.99	94.1

Table 4 SDNR (90 mAs) on each slice surface of proc data

Height (mm)	SD (bg)	contrast	SDNR	Difference (%)
5	189.3	653.5	3.45	108.9
10	193.1	608.6	3.17	100.0
15	197.0	568.9	2.89	91.1
25	200.3	498.8	2.49	78.5
35	200.3	514.9	2.57	81.1
45	200.9	532.7	2.65	83.6

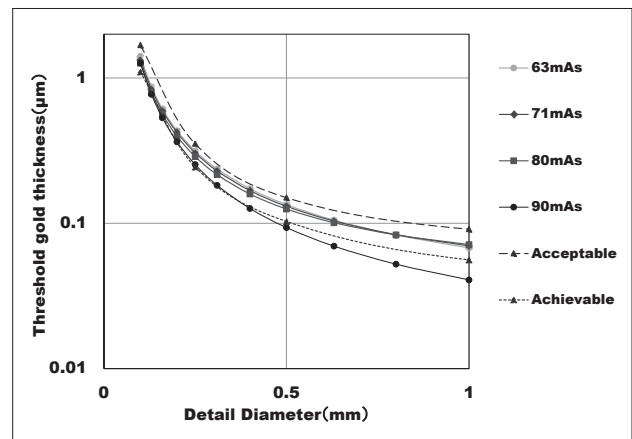


Fig.4 Relationship between mAs value and low contrast resolution in prj data

Table 5 IQF_{inv} for prj data

mAs	IQF _{inv}	IQF _{inv 0.16}
63	106.8	173.7
71	110.9	180.5
80	114.1	181.2
90	127.2	211.2

ence in contrast at 25, 35, and 45 mm.

3.2.1 Experiment low-contrast resolution

Fig.4 shows the result of low-contrast resolution of the prj data. EUREF publishes guidelines for a quality system for breast cancer screening, and the fourth edition (MMG guidelines) is used as an accuracy management manual for digital mammography¹¹⁾. In the MMG guidelines, acceptable and achievable levels are shown as thresholds to be achieved when digital mammography is used clinically. However, Protocol DBT does not show a threshold in DBT. Therefore, the acceptable and achievable levels of Fig.4 are thresholds in digital mammography. The prj data had a lower dose per sheet than that of digital mammography, but all mAs values satisfied the acceptable level. At 90 mAs, the same low-contrast resolution was obtained as the achievable level.

The IQF_{inv} at each mAs value is shown in Table 5. Since the pixel size of the detector of the DBT device used this time is 85 µm, IQF_{inv0.16} up to 0.16 mm, which is the disk diameter closest to 0.17 mm per period, was also calculated.

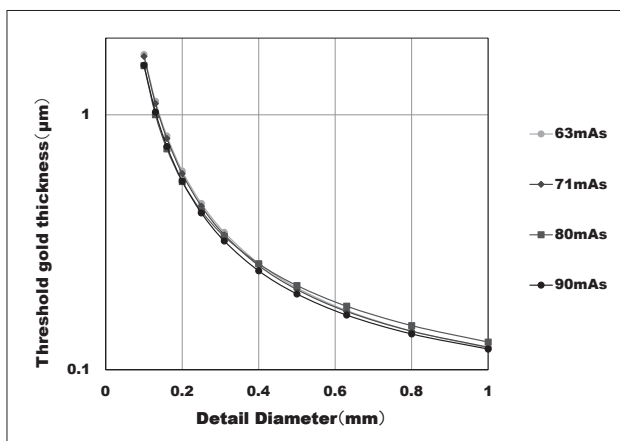


Fig.5 Relationship between mAs value and low contrast resolution in proc data

Table 6 IQF_{inv} for proc data

mAs	IQF _{inv}	IQF _{inv 0.16}
63	74.33	85.40
71	75.60	86.71
80	77.42	88.04
90	79.81	91.20

In the prj data, the IQF_{inv} increased in conjunction with the mAs value.

Fig.5 shows the result of low contrast resolution of proc data. The low-contrast resolution of the proc data satisfies the achievable level at all mAs values.

IQF_{inv} at each mAs value is shown in Table 6. As with prj data, the higher the mAs value, the better the IQF_{inv}.

IQF_{inv} and IQF_{inv0.16} showed similar trends. Therefore, IQF_{inv0.16} is used for the analysis of the following CDMAM considering the pixel size of the detector of the DBT device.

3.2.2 Experiment SDNR

The results of SDNR are shown in Table 7. In the prj and proc data, the SDNR improved as the mAs value was increased.

4. Considerations

4.1 Pre-experiment effect of slice plane differences on SDNR

In the prj data, the SDNR decreased as the

Table 7 SDNR at each mAs value

mAs	SDNR	
	prj data	proc data
63	1.68	2.14
71	1.78	2.20
80	1.89	2.29
90	2.06	2.49

slice surface separated from the breast support stand, but there was no significant change in the SD or contrast. Therefore, the effect of the slice surface on SDNR was small in the prj data.

In the proc data, the change in SDNR due to the difference in the slice surface was not significant. Therefore, there was a change of SDNR by the slice surface in proc data compared with prj data.

4.2.1 Experiment low-contrast resolution

In the prj data, the low-contrast resolution improved because IQF_{inv} increased in conjunction with the mAs value.

In proc data, IQF_{inv} improved as the mAs value was increased, similar to the prj data.

4.2.2 Experiment SDNR

In prj and proc data, the SDNR improved in conjunction with the mAs value.

4.3 Overall judgment

In the MMG guidelines, threshold contrast (Threshold contrast limiting value) by CDMAM is shown. To use digital mammography clinically, the measured SDNR (SDNR_{measured}) needs to exceed the SDNR_{limiting value} calculated using Equation 3.

$$\text{SDNR}_{\text{limiting value}} = (\text{Threshold contrast}_{\text{measured}} / \text{Threshold contrast}_{\text{limiting value}}) \times \text{SDNR}_{\text{measured}} \quad \dots \text{Equation 3}$$

However, since the threshold contrast limiting value in DBT is not presented, it can't be evaluated by dose reduction. In this study, we calculated the SDNR_{limiting value} at each mAs value

Table 8 Calculation result of prj data

mAs	CDMAM _{0.16}	SDNR _{measured}	SDNR _{limiting value}
63	0.61	1.68	1.93
71	0.60	1.78	1.99
80	0.56	1.89	2.00
90	0.53	2.05	

Table 9 Calculation result of proc data

mAs	CDMAM _{0.16}	SDNR _{measured}	SDNR _{limiting value}
63	0.83	2.14	2.37
71	0.81	2.20	2.38
80	0.74	2.29	2.26
90	0.75	2.49	

from Equation 4 based on 90 mAs.

$$\text{SDNR}_{\text{limiting value}} = \frac{\text{Threshold contrast}_{\text{measured}}}{\text{Threshold contrast}_{90\text{mAs}}} \times \text{SDNR}_{\text{measured}}$$

…Equation 4

SDNR_{measured} : SDNR measurements at PMMA 50 mm

Threshold contrast_{measured} : Detectable disc thickness at 0.16 mm diameter

Threshold contrast_{90mAs} : Limit of disk thickness of 0.16 mm in disc diameter at 90 mAs

The calculation results of the prj data are shown in Table 8. In the prj data, SDNR_{measured} was 1.68 at 63 mAs, 1.78 at 71 mAs, and 1.89 at 80 mAs, and the SDNR_{limiting value} could not be met. Therefore, the auto-mode setting is currently the best option.

Next, the calculation results for proc data are shown in Table 9. The SDNR_{measured} was 2.14 at 63 mAs, 2.20 at 71 mAs, and 2.29 at 80 mAs, and the SDNR_{limiting value} could not be met at 60 mAs and 71 mAs. However, at 80 mAs, it was equivalent to the SDNR_{limiting value}. Therefore, the mAs value could be reduced to 80 mAs. Since the shooting dose was 1.83 mGy at 90 mAs and 1.65 mGy at 80 mAs, if the mAs value is reduced from 90 mAs to 80 mAs, the shooting dose can be reduced by 0.18 mGy.

5. The limits of this study and future issues

The analysis software used in this study needs to use prj data for IQF_{inv}, and verification is necessary for the accuracy of the analysis results of proc data. In addition, it is necessary to examine not only physical evaluation but also use visual evaluation to check consistency.

In addition, the detector, target/filter, vibration angle, reconstruction method, number of photographs, etc., differ depending on the device, but this study has the results for a unique device. Therefore, it is necessary to examine dose reduction by this method in each type of equipment while ensuring image quality.

6. Conclusion

In this study, overall image quality characteristics were examined using CDMAM phantom and SDNR. In the image of proc data, the possibility of dose reduction was indicated.

References

- 1) T Shiomi: The Principle and Clinical Application of Tomosynthesis. Medical Imaging and Information Sciences, 24 (2), 22-27, 2007.
- 2) Japan Association of Breast Cancer Screening, et al.: Recommendations for dealing with the dense breast problem in Organisation screening for breast cancer. 2017.
- 3) N Uchiyama, et al.: Diagnostic Performance of combined Full Field Digital Mammography (FFDM) and Digital Breast Tomosynthesis (DBT) in Comparison with Full Field Digital Mammography (FFDM). RSNA, 2010.
- 4) T Uematsu: Expectations and Challenges for Mammography Screening Using Breast Tomosynthesis. Journal of Japan Association of Breast Cancer Screening, 23 (2), 270-278, 2014.
- 5) The 2007 Recommendations of the International Commission on Radiological Protection. Annals of the ICRP. ICRP Publication 103, 37 (2-4), 182, 2007.
- 6) Japan Network for Research and Information on Medical Exposure, et al.: Diagnostic reference levels based

- on latest surveys in Japan –Japan DRLs 2015–. 20, 2015.
- 7) I Isomoto: The Harm Due to Radiation Exposure in Screening Mammography. Japanese Journal of Breast Cancer, 30 (1), 29-35, 2015.
 - 8) N Shinohara: Trial of the Quality Control in Digital Breast Tomosynthesis System. Bulletin of Gifu University of Medical Science, 12, 1-4, 2018.
 - 9) European Reference Organisation for Quality Assured Breast Screening and Diagnostic Services: Protocol for the Quality Control of the Physical and Technical Aspects of Digital Breast Tomosynthesis Systems version 1.03.
 - 10) T Okabe, et al.: Shin-iyohousyassenkagakukouza iyougazoujouhoukougaku. 208. ISHIYAKU Publishers, Inc., 2018.
 - 11) European Reference Organisation for Quality Assured Breast Screening and Diagnostic Services: European Guidelines for Quality Assurance in Breast Cancer Screening and Diagnosis 4th edition.

Modification methods of radiographic conditions alternative to tube voltage coefficient chart

HATAKEYAMA Norihito

Osaka Roudouisei Center Daiichi Hospital, Radiology Department, Radiological Technologist

Note: This paper is secondary publication, the first paper was published in the JART, vol. 68 no. 821: 23-28, 2021.

Key words: Radiographic condition, exposure index, tube voltage coefficient, computer simulation, inverse square law

[Abstract]

This study aimed to improve the conventional method of imaging, using the tube voltage coefficient chart. Accordingly, the MAS coefficient was introduced as the new, alternative coefficient to the tube voltage coefficient, and its chart was prepared. Using the approximate function obtained by measuring the exposure index (EI), we calculated the radiographic conditions for correction. The difference between the measured EI and target EI was below ± 0.1 . Hence, our corrections eliminated some error factors associated with the conventional method.

1. Introduction

Uchida et al.¹⁻²⁾ proposed a conventional imaging method using a tube voltage coefficient chart for correcting the radiographic conditions designed for a standard body type, while Asahi et al.³⁻⁴⁾ and Morikawa et al.⁵⁾ proposed an imaging method using a correction coefficient. The conventional method was theoretically simplified for use in clinical radiological examinations; however, its precision was compromised. The conventional method has several issues that include elements associated with radiography, the decrease in the elements that exhibit differences in the radiation quality, and the power n that constitutes the exponential function of a tube voltage which expresses the radiation quality, does not have clear criteria for calculation. The standard for approximation in the calculation of n was unclear. In this instance, the term “unclear” signifies the generation of the tube voltage coefficient by a radiological technologist for a hospital on the basis of the considered tolerable error range generated by the clinical radiological examinations and set arbitrarily.

Our proposed method resolved some of the issues associated with the conventional meth-

od. Specifically, our proposed method used a computer to correct the radiographic conditions to avoid any reading errors associated with the tube voltage coefficient chart.

2. Materials and methods

For the conventional and proposed methods, the standard radiographic conditions (standard condition) with modifications were considered as the primary modified radiographic conditions (primary condition), and the primary conditions with modifications were considered as the secondary modified radiographic conditions (secondary condition). The issues associated with the conventional method for which improvements were made in the proposed method are indicated by “()” with the letter A and a number from 1 to 7.

2.1 Experimental devices

The following devices were used for the experiments.

X-ray tube: 0.6/1.2 P323 DK-85 SHIMADZU Corporation (Kyoto, Japan)

X-ray apparatus for general radiography: RAD speed Pro SHIMADZU Corporation (Kyoto, Japan)

High voltage generator: UD150L-40 SHIMADZU Corporation (Kyoto, Japan)

X-ray detector: SKR3000 (AeroDR3 1417HD) KONICA MINOLTA (Tokyo, Japan)

Phantom: a few 1 cm polymethyl methacrylate boards (PMMA)

2.2 Modification of the standard conditions and setting of the primary conditions

Each X-ray system of each clinical radiological examination room programs the standard condition into the memory of the X-ray system by using the paired comparisons⁶⁾ and/or the ranking method⁷⁾ or considering the width of the dynamic range of the digital system and energy characteristics of the detector⁸⁾. If a subject possesses phantom thickness, object motion and the magnification ratio based on the geometrical positional relationship for an object in a standard body shape (a subject), appropriate images can be obtained by using the standard condition. When the thickness and fleshiness of the subject differ from the standard body shape, the conventional method is applied. Equation (1) is an empirical formula used by the Japanese radiological technologists as it includes the elements necessary for radiography.

$$E = K \frac{V^n i t s f Z}{r^2 B G} e^{-\mu d} \quad \dots\dots\dots (1)$$

Where E denotes a finite radiographic effect on the film (photographic density), K is a constant used for adjusting the photographic effect, V represents a tube voltage (kV), n represents the power of an exponential function that describes a characteristics of radiation quality, i is a tube current (mA), t is imaging time (second: s), s is the magnifying power of an intensifying screen, f represents film sensitivity, Z represents the atomic number of a focal spot substance, μ and d represent the attenuation factor and thickness (cm) of an examinee's body, respectively, r is the distance

between a focal spot and an image (Source-Image Distance [SID], cm), B is a Bucky factor (exposure magnifying factor), and G is the factor with respect to the area of an irradiation field (cm²).

Applying the logarithm operator to Equation (1) yields Equation (2).

$$\ln(q) = \mu d + L \quad \dots\dots\dots (2)$$

Where q is the mAs, a current time product, obtained by multiplying i (mA) and t (s), μ is the slope of a linear equation, and L is a compiled set of intercepts and constants, including the values arbitrarily determined.

In other words, if the slope and intercept of a linear equation can be obtained empirically, the mAs necessary for a phantom image with a thickness of d can be obtained.

These equations can be simultaneously solved by using two different phantom thicknesses and the tube voltage under standard conditions, and by taking images with an equivalent photographic effect (A1: specification of radiation quality). Therefore, the mAs is calculated to obtain an image of a subject with the same photographic effect as the standard condition.

However, the thickness and fleshiness of the subject must be converted to the phantom thickness.

2.3 Setting the secondary conditions by modifying the primary conditions

However, sometimes radiological technologists prefer to change the tube voltage without changing the mAs. Equation (3) is derived using Equation (1) when the primary condition is modified to the secondary condition with the equivalent exposure index (EI) to the primary condition.

$$K \frac{V1^{n1} i1 t1 F1 Z1}{(r1)^2 B1 G} e^{-\mu1 d} = K \frac{V2^{n2} i2 t2 F2 Z2}{(r2)^2 B2 G} e^{-\mu2 d} \quad \dots\dots\dots (3)$$

The variables listed with the index of one indicate the primary condition, whereas the variables listed with the index of two indicate the secondary condition.

However, s and f in Equation (1) were substituted by F . F is the sensitivity of flat panel detector (FPD). Furthermore, E is considered as EI.

Equation (3) can be converted to Equation (4).

$$\frac{V1^{n1} F1 Z1 B2 e^{-\mu1 d}}{V2^{n2} F2 Z2 B1 e^{-\mu2 d}} = \frac{i2 t2 (r1)^2}{(r2)^2 i1 t1} \dots\dots\dots (4)$$

Equation (4) in the conventional method is simplified to Equation (5) by assuming a minor radiation quality impact.

$$\frac{V1^{n1}}{V2^{n2}} = \frac{i2 t2 (r1)^2}{(r2)^2 i1 t1} \dots\dots\dots (5)$$

The left side of Equation (5) is the tube voltage coefficient, and the right can be obtained experimentally. The tube voltage coefficient is approximately calculated as $n1 = n2$.

The right side of Equation (4) is named as "the MAS coefficient" in the proposed method by us. The MAS coefficient is defined as a coefficient that is obtained by normalizing a new mAs per unit surface area that is used when generating X-rays are emitted from a given center in the secondary condition, on basis of a mAs per unit surface area that is used when generating X-rays are emitted from a given center in the primary condition (A2: Equation (4) is not simplified to Equation (5), A3: We avoided calculation of n).

Furthermore, we prepared approximate function for the MAS coefficient.

$$\frac{i2 t2 (r1)^2}{(r2)^2 i1 t1} = Q \dots\dots\dots (6)$$

$$Q = Y(V2) \dots\dots\dots (7)$$

Where Q is the MAS coefficient, $V2$ is the modified tube voltage (kVp) which is also a variable, $Y - (V2)$ is an approximate function when variable $V2$ is on the horizontal axis and the MAS coefficient is on the vertical axis.

2.4 Preparation of the approximate function

When $V2 \leq V1$ or $Q \geq 1$, for example, we use Equation (8) with $Y - (V2)$.

$$Y(V2) = \frac{e^{(k2)}}{(V2)^{k1}} \dots\dots\dots (8)$$

When $V2 > V1$ or $Q < 1$, for example, we used Equation (9) with $Y - (V2)$.

$$Y(V2) = e^{-(V2)^{k3+k4}} + k5 \dots\dots\dots (9)$$

Where $k1$, $k2$, $k3$, $k4$, and $k5$ are values that constitute the approximate function. These are set for each phantom thickness.

Given that we followed the conventional method in setting the primary condition, we omitted the demonstration experiment to modify the standard condition, and assumed the following as the primary condition: tube voltage of 50 kVp, tube current of 200 mA, imaging time of 18 ms, irradiation field of 20×20 cm on the FPD, an SID of 120 cm and phantom thickness of 8 cm PMMA. The imaging protocol used was "TEST QC S value" of KONICAMINOLTA CS-7. The conditions associated with this protocol produced an EI of approximately 250. Several secondary conditions were prepared in an experiment with an SID 120 cm to achieve the EI before and after 250, as linear interpolation was performed between them.

Table 1 lists the linear interpolation outcomes of the radiographic conditions that were required to achieve an EI of 250 and the calculated MAS coefficient Q .

Figure 1 shows Q from Table 1 plotted on the vertical axis as a function of $V2$ on the horizontal axis. Figure 2 shows the approximate function of the MAS coefficient chart expressed by

Equations (8) and (9), with Q on the vertical axis and V2 on the horizontal axis. This approximate function was prepared based on k1, k2, k3, k4, and k5, which were calculated to have the following values: 5.74091, 22.47204, 0.55992, 8.87683, and 0.07114, respectively, with a pass-point limit Q = 1.0 using Excel (Microsoft Office 2013, Microsoft Corp., Redmond, WA, USA). Q = 1.0 was used as a calculation constraint to resolve the problem of the tube voltage coefficient not always passing the value of 1.0 in the chart, although it should during

the modified condition calculation without changing the tube voltage (A4: resolving the passing point issue).

2.5 Demonstration experiment

We left imaging time as blank and set the secondary condition using the approximate function. Then, the secondary condition taps (tic marks of the X-ray system) were set by applying the radiographic condition taps by setting their values so that they fell within the practical range of our hospital, and the values

Table 1 Interpolated radiographic conditions and the MAS coefficient Q with an EI of 250

kVp	mAs	coefficient Q
46	29.45	1.61
48	23.14	1.27
50	18.24	1.00
56	10.52	0.58
63	6.11	0.34
72	3.56	0.20
78	2.60	0.14

Table 2 Secondary conditions generated by the approximate functions when imaging time was assumed as blanks

Condition No.	kVp	mA	cm SID	ms
8 cm, No.1	45	160	115	38.87
8 cm, No.2	45	200	115	31.09
8 cm, No.3	56	250	125	9.41
8 cm, No.4	73	80	75	3.30
8 cm, No.5	51	200	75	6.57
8 cm, No.6	73	100	115	6.20
8 cm, No.7	62	80	85	8.48
8 cm, No.8	68	100	75	3.51
8 cm, No.9	45	80	125	91.84
8 cm, No.10	68	320	105	2.15

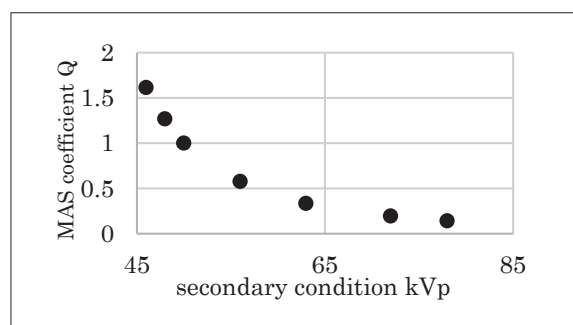


Fig.1 Plot of Q as a function of V2

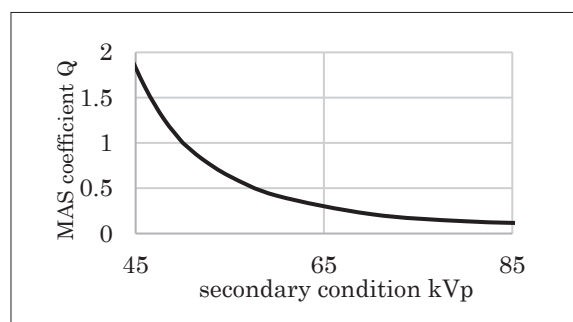


Fig.2 Q chart of the MAS coefficient using Equations (8) and (9) (45–85 kVp)

Table 3 Secondary conditions recalculated by the approximate functions when we assumed a tube voltage of blank by setting of 5 ms or more, the measured EI by the secondary conditions, and the relative errors between the measured EI and the target EI

Condition No.	kVp	mA	cm SID	ms	measured EI	relative error
8 cm, No.1	45	160	115	40.0	264.14	0.057
8 cm, No.2	45	200	115	32.0	262.96	0.052
8 cm, No.3	56	250	125	9.0	245.80	-0.017
8 cm, No.4	62	80	75	6.3	246.36	-0.015
8 cm, No.5	51	200	75	6.3	232.89	-0.068
8 cm, No.6	73	100	115	6.3	257.11	0.028
8 cm, No.7	62	80	85	8.0	245.25	-0.019
8 cm, No.8	62	100	75	5.0	237.12	-0.052
8 cm, No.9	45	80	125	90.0	260.02	0.040
8 cm, No.10	56	320	105	5.0	245.25	-0.019

were determined randomly by rolling dice thrice. The three rolls of the dice yielded the following values: 45, 51, 56, 62, 68, and 73 for tube voltage (kVp), 80, 100, 160, 200, 250, and 320 for tube current (mA), and 75, 85, 95, 105, 115, and 125 for SID (cm).

Table 2 shows the secondary condition calculated by using the approximate function with imaging time as blank. However, at our hospital, considering the reliability of the linearity of the timer, we did not use imaging times < 5 ms. Thus, when the imaging time was less than 5 ms, we set it to ≥ 5 ms, left the tube voltage as blank, and recalculated the secondary condition using the approximate function. Table 3 lists the secondary condition recalculated with the approximate function (A5: we did not read the values from the chart). However, all the secondary conditions were prepared with taps that can be set for the X-ray system. In other words, we selected the nearest taps for the set imaging time and the tube voltage calculated by the approximation function. Table 3 shows the relative difference between the measured EI and target EI of 250 for the secondary condition.

3. Results

In the demonstration experiment that used 8 cm PMMA, the measured EI under the secondary condition prepared with the approximate function of the MAS coefficient Q was within the relative error of ± 0.1 of the target EI. In addition, we changed PMMA to 1, 5, 11, and 15 cm and performed the same demonstration ex-

Table 4 Demonstration experimental outcomes with relative errors $> \pm 0.1$

Condition No.	kVp	mA	cm SID	ms	measured EI	relative error
1 cm, No.9	45	80	125	22	276.29	0.11
15 cm, No.6	73	100	115	18	221.15	-0.12
15 cm, No.7	62	80	85	32	281.94	0.13

periment. The results that did not fall within the relative error of ± 0.1 are listed in Table 4.

4. Discussion

The developmental objective of the conventional method was to maintain a relative error of ± 0.25 with the target photographic density. The aim was to avoid reacquiring an analog image even if there were shades. The proposed method aimed to maintain the relative error with the target EI within ± 0.1 (A6: specification of the developmental objective).

In the initial experiment, there was an error in the solution of the simultaneous equations at Equation (2), which did not achieve the developmental objective. Specifically, to set the primary condition, we assumed that the phantom thicknesses ranged from 1 to 15 cm for the demonstration experiment and grid-less imaging of four limb, and measured the mAs with the PMMA phantom as 1, 4, 7, 10, 13, and 15 cm to achieve an EI of 250. We then performed a regression analysis (Figure 3). However, with this regression line, we were unable to express the actual value that yielded a slight convex downward, thus leading to residual difference. Coupled with the error of the secondary condition, we were unable to achieve the developmental objective. Thus, we performed another regression analysis by dividing the entire range

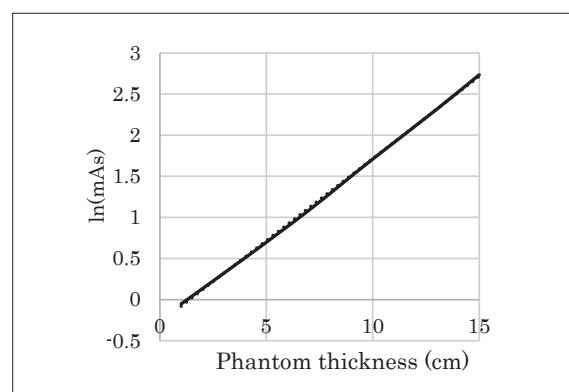


Fig.3 Plot of Equation (2). The solid line denotes the data. The dotted line is the regression line (1–15 cm: $y = 0.1996x - 0.2794$; $R^2 = 0.9996$).

into 1–7 cm and 7–15 cm segments, and used a regression line with a coefficient of determination $R^2 = 0.9999$ to perform a demonstration experiment for a phantom thickness of 8 cm (Figure 4). In this manner, we achieved the developmental objective.

Similarly, we performed more demonstration experiments by changing the phantom thickness to 1, 5, 11, and 15 cm. Some results that did not meet the developmental objectives are listed in Table 4. However, these results were attributed to the calculation result of the imag-

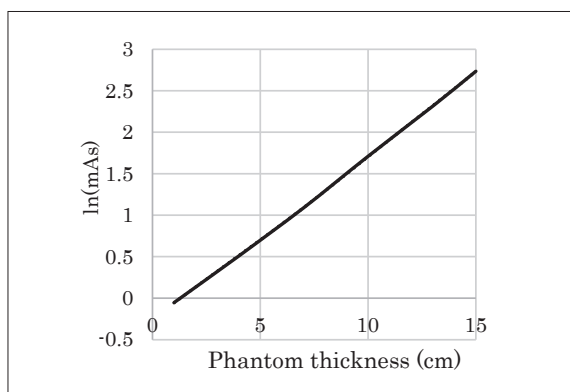


Fig.4 Plot of Equation (2). The solid line denotes the data. The dotted line is the regression line (1–7 cm: $y = 0.1899x - 0.2448$; $R^2 = 0.9999$, 7–15 cm: $y = 0.2053x - 0.3481$; $R^2 = 0.9999$).

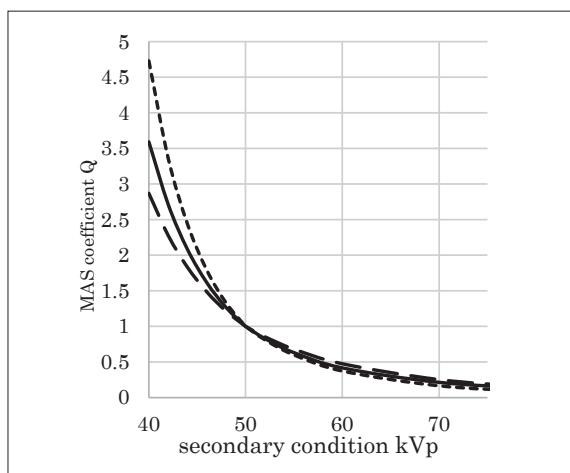


Fig.5 Q chart of the mAs coefficient (40–75 kVp) for the demonstration experiment. The solid line is the approximate function for 8 cm PMMA. The broken line is the approximate function for 1 cm PMMA. The dotted line is the approximate function for 15 cm PMMA.

ing time with the approximate function with the closest taps as follows: 21.11 ms being either equal to 20 or 22 ms, 18.97 ms being either equal to 18 or 20 ms, and 30.06 ms being either equal to 28 or 32 ms.

Figure 5 shows the approximate function of the MAS coefficient used for calculation with the phantom thicknesses of 1, 8, and 15 cm. For example, if we want the MAS coefficient Q for a radiographic condition of 50 kVp to be 0.5, even in the same system, modifications must be implemented with a difference of 59.3 kVp for the thickness of 1 cm, 57.8 kVp for 8 cm, and 56.9 kVp for 15 cm.

5. Conclusions

We eliminated several causes of errors associated with the conventional method and introduced a method to modify radiographic conditions with fast calculations. However, the database of the approximate function of the MAS coefficient Q for each structure of an X-ray system, imaged part, and the phantom thickness must be prepared ahead of time (A7: specification of notes). The proposed method required setting radiographic conditions that were modified for each subject. Specifically, there was an EI that was equivalent to the EI obtained in the standard condition. X-ray system vendors should release X-ray systems that allow for more fine-tuned settings of imaging time for setting of appropriate radiographic conditions.

In actual X-ray examination, radiological technologists often acquire images using an automatic exposure control, as it is not easy to convert the subject to phantom thickness. However, as the foundation of radiological techniques, we must identify ways to modify the radiographic conditions. When discussing a method to select one radiographic condition from multiple ones with the same EI, it will become clear why radiological technologists must have a priori knowledge of the modula-

tion transfer function and the noise power spectrum. This is because the automatic exposure control does not see the actual subject. In other words, it determines the radiographic condition regardless of the movement and geometric position of the object in a subject. Thus, the image is not necessarily an appropriate diagnostic image. The automatic exposure control and automatic gradation conversion processing are complementary technologies for radiological techniques.

Acknowledgements

The author would like to extend the sincerest appreciation to late Prof. Masaru Uchida for requesting the redevelopment of the imaging method, late Prof. Kazuya Yamashita for teaching me the weaknesses of the conventional method, and Prof. Hiroshi Inatsu who permitted the use of the copyright for the conventional method. The author also would like to thank Ulatus in manuscript translation.

Funding

No funding was received for the pursuit and completion of this study.

Conflicts of interest

The author has no conflict of interest to declare.

However, we secured a patent in Japan and the United States to ensure the novelty of the process of correcting the primary condition and creating the secondary condition.

Ethics statement

No humans or animals were involved in this study.

References

- 1) UCHIDA Masaru, et al.: HOUSHASEN GIJUTSUSHA NO TAMENO GAZOU KOGAKU (Imaging technology for radiologists). Tokyo: Tsusho sangyo kenkyu sha, co. 1978, in Japanese.
- 2) KOZUKA Takahiro, et al.: Textbook of clinico-radiological technology. Version 14. First volume. Tokyo: Nankodo Co., Ltd., P.13-72, 2019, in Japanese.
- 3) ASAHU Toshiharu: The first report on the study of correction coefficient for radiographic condition for each type of X-ray device. Correction coefficient: Photographic effect from film blackening. Japanese Journal of Radiological Technology, Vol.23, No.1, p 94, 1967, in Japanese.
- 4) ASAHU Toshiharu: Attempts with correction coefficient for radiographic conditions (with dosimeter method). Japanese Journal of Radiological Technology, Vol.24, No.1, p 95, 1968, in Japanese.
- 5) MORIKAWA Kaneo, et al.: Correction table for radiographic condition. Japanese Journal of Radiological Technology, Vol.37, No.3, p 385-386, 1981, in Japanese.
- 6) OHGA Yasufumi, et al.: Method of subjective evaluation on radiograph - Scaled experiment by Thurstone's method of paired comparisons. Japanese Journal of Radiological Technology, Vol.45, No.7, p 831-839, 1989, in Japanese.
- 7) NAKAMAE Mitsuhiro: Study of the reliability of visual evaluation by the ranking method - analysis of ordinal scale and psychological scaling using the normalized-rank approach. Japanese Journal of Radiological Technology, Vol.56, No.5, p 725-730, 2000, in Japanese.
- 8) ODA Nobuhiro, et al.: Evaluation of 90 kV beam with 0.15 mm Cu filter in chest radiography using CsI-flat panel detector. Japanese Journal of Radiological Technology, Vol.76, No. 5, p 463-473, 2020, in Japanese.

New challenges for SARS-CoV-2 -Infection control in Mobile X-ray-

MOCHIGI Kazuya¹⁾, SHINAGAWA Kazuki²⁾

1) National Center for Global Health and Medicine, Radiology department, Chief

2) National Center for Global Health and Medicine, Radiology department, Radiological Technologist

Note: This paper is secondary publication, the first paper was published in the JART, vol. 68 no. 821: 29-37, 2021.

Key words: COVID-19, Infection control, Mobile chest X-ray, Nosocomial infection

[Abstract]

Purpose

The purpose of this study is to examine the procedures in use related to portable chest radiography in COVID-19 patients and to prevent nosocomial infections as well as infections among Radiology Department staff.

Method

A dedicated mobile X-ray machine for COVID-19 patients was utilized, and the procedures related to the disinfection of the device, as well as attachment/detachment of infection protection equipment, was examined.

Result

From January 21, 2020 to April 28, 2020, the number of mobile X-ray cases for COVID-19 at this hospital was 1,439. As of May 15, 2020, COVID-19 positivity according to PCR testing was 0% among 50 medical radiologists. The information was shared via Microsoft Teams, with immediate distribution, and it was designed to enable browsing and access on mobile devices at any time.

Conclusion

By incorporating the portable X-ray imaging method into COVID-19 diagnosis and treatment, it was both effective and ensured the safety of the radiologic technologists and also prevented nosocomial infections.

Introduction

During the COVID-19 pandemic this hospital accepted numerous returnees from Wuhan, China, arriving both on charter flights and from ocean-going cruise ships.

Additionally, to evaluate infiltrating shadows in the lung fields for both suspected and confirmed COVID-19 cases, mobile chest X-ray examinations have been performed, including febrile outpatients and within the hospital emergency medicine department.

In portable chest radiography, a cassette (CR: Computed Radiography, or FPD: Flat Panel Detector) must be positioned on the patient's back and adjusted. As a result, many situations exist where direct physical contact between the radiologist or radiology technician, and the patient is required. Therefore, maintaining a specified minimum distance from the patient is impossible.

In recent years, a variety of devices have been introduced into portable X-ray systems. As a result, imaging is performed while touching various devices in addition to the portable X-ray system. Inevitably, the number of contaminated areas increases, resulting in an examination which demonstrates a heightened risk of infection for both patients and medical personnel.

A manual for the prevention of nosocomial infections was prepared by the hospital's Infection Control Team (ICT) with specific measures such as hand disinfection methods, procedures for donning and doffing personal protective equipment (PPE), and separation of linens and infectious waste. It is believed that if all staff members work together according to this manual, preventing nosocomial infections will be possible. However, specific infection-control methods for portable radiography have yet to be defined.

Radiologists must take the lead and examine what countermeasures must be taken in each situation while performing actual portable radiography and what measures must be taken according to the principles of infection control.

The purpose of this study is to review the procedures of portable chest radiography in the COVID-19 environment, evaluate the clinical diagnostic options, to ensure the safety of radiologists and radiology technicians and to prevent nosocomial infection.

1. Methods

1-1 Confirmation of the route of infection in COVID-19

The current evidence suggests that SARS-CoV-2, the pathogen which causes COVID-19, is isolated from airway secretions and feces and enters the body when it comes into contact with the mucous membranes of the eyes, nose, and mouth.

Based on this understanding, standard precautions, including respiratory hygiene and cough etiquette, as well as contact and droplet infection-control measures, should be taken for suspected and positive COVID-19 cases. Additionally, because procedures such as suctioning patients' airways, endotracheal intubation, and the collection of lower respiratory tract specimens may generate aerosols, N95 masks should be worn to reduce the possibility of airborne infection¹⁾. However, for safety reasons, all personnel conducting mobile chest X-rays at this hospital use N95 masks.

1-2 Confirmation of COVID-19 compliant wards

In addition to checking infection routes, understanding the location of infection-control items in COVID-19 outpatient clinics and in inpatient wards dedicated to COVID-19 is very important. The locations of PPE and designated clean and contaminated areas were confirmed, and the locations of infectious waste containers were identified in advance and

made known to the staff of the radiology department (Fig.1).

1-3 Infection-Control Measures for Equipment Used

1-3-1 Equipment used

The portable X-ray system utilized was a HITACHI Sirius 130H inverter-type cordless mobile X-ray system. Additionally, a KONICA wireless FPD Aero DR System was used as the cassette so that body movements and breathing, which can cause blurring and require re-imaging, can be checked in the contaminated area while wearing PPE.

In addition to the FPD, the Aero DR System includes the CS-7 (notebook PC) as a console, the Aero DR rounding unit (UF unit), and a barcode reader for patient authentication.

1-3-2 Equipment contact location

Since COVID-19 is a contact and droplet infection, researchers decided that points of contact are required to be limited in advance to prevent the spread of contamination. Therefore, red circular stickers were placed on the

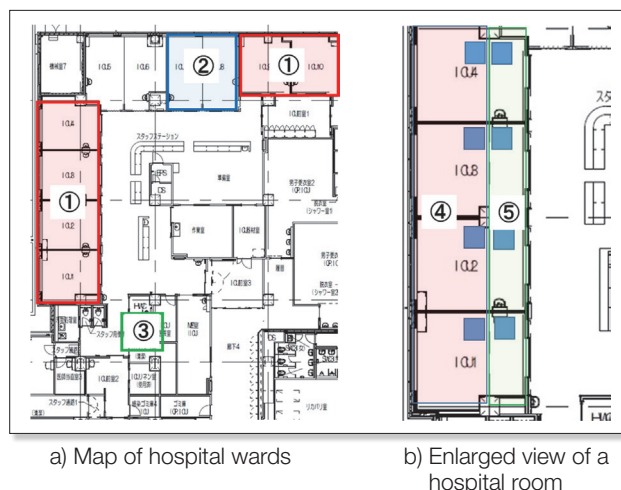


Fig.1 Layout of COVID-19 compliant wards (e.g., ICU wards)

- ① Hospital room
- ② Personal Protective Equipment article storage locations
- ③ Storage location for portable X-ray equipment
- ④ Contamination area
- ⑤ Clean area
- Trash can for infection

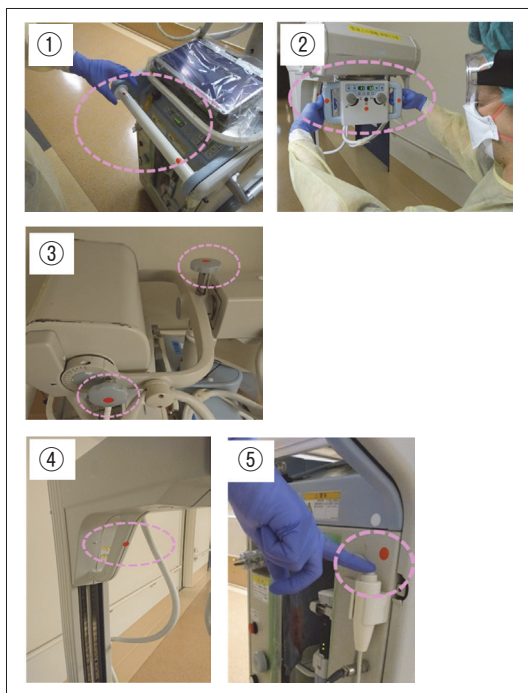


Fig.2 Equipment contact location

- ① Equipment actuating lever
- ② Both side handles of aperture handle, irradiation field aperture, irradiation field lamp, and shooting condition setting switch
- ③ Front/rear and left/right locking parts (2 locations)
- ④ Handle switch
- ⑤ exposure switch

minimum necessary areas to visually identify the points of contact (Fig.2).

1-3-3 Secure temporary clean areas for equipment

Since all imaging locations were within the contaminated area, a temporary clean area was required to keep the FPD clean. As a result, a temporary clean area was set up in the cassette folder of the portable device, and the FPD, CS-7, UF unit, physical grid, barcode reader, and disinfection items were placed there based on the assumption that this area would not be contaminated (Fig.3).

1-3-4 FPD

To prevent contamination, the FPD was covered prior to use with a 45 L plastic bag. When using the FPD, procedures (1) through (5) were followed (Fig.4).



Fig.3 Temporary clean area for equipment



Fig.4 FPD contamination prevention measures



Fig.5 Infection Prevention Measures for CS-7

1-3-5 CS-7

The CS-7 is a touch-panel type console. Therefore, it was covered with a standard plastic bag No. 15 (300 mm x 450 mm) when in use, to prevent contamination (Fig.5).

1-3-6 Items to be disinfected

SARS-CoV-2 exhibits an envelope protein, making alcohol disinfection effective ¹⁾.

Therefore, researchers decided to prepare alcohol or sodium hypochlorite in advance (Fig.6).

1-3-7 Infection protection devices

The infection related items required for COVID-19 are shown in Figure 7. In portable radi-



Fig.6 Preparation of disinfection supplies



Fig.8 N95 mask fit test

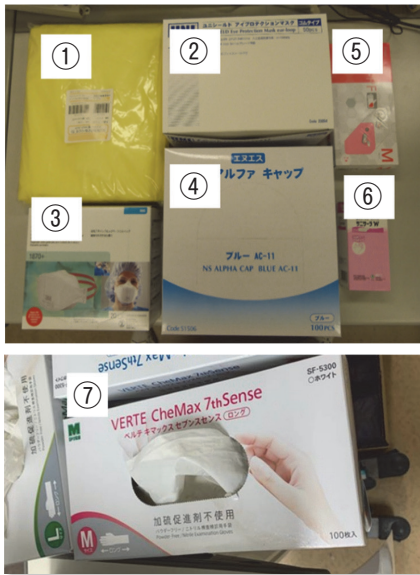


Fig.7 Infection protection devices

- ① Isolation gown
- ② Uni-Shield eye protection mask or goggles
- ③ N95 Mask
- ④ NS Alpha Cap
- ⑤ Outer glove
- ⑥ Alcohol disinfection
- ⑦ Inner glove

ography, the wrist may be exposed when the cassette is placed on the patient's back. To prevent exposure, an inner glove that can cover the wrist tightly is used. Confirming the appropriate glove size in advance is important (Fig.7).

1-4 Preparation before inspection

1-4-1 Wear of an N95 mask

The duration of SARS-CoV-2 in the environment is unknown at this time, and to respond to this situation, surgical masks may be used if aerosols are not generated¹⁾. However, how much virus is airborne as a result of the prolonged stays of hospitalized patients in their hospital rooms is not readily apparent. There-



- ① FPD
- ② CS-7
- ③ Items to be disinfected
- ④ UFユニット
- ⑤ bar code reader

Fig.9 Storage in temporary clean area

fore, for safety reasons, the radiology technician chose to wear an N95 mask beforehand. The N95 mask was fitted while looking in a mirror, and a fit test was conducted beforehand to ensure that no air leaks were found (Fig.8).

1-4-2 Preparation for Imaging

The FPD, CS-7, and disinfection supplies needed for imaging were covered with plastic bags and temporarily stored in the clean area. Since the barcode reader for patient authentication was used in advance in the clean area, researchers decided not to cover it with a plastic bag to simplify its operation. Additionally, the barcode reader was stored in the temporary clean area (Fig.9).

1-5 PPE Wear Procedures

1-5-1 Wear of PPE

When PPE was worn, the hands were first disinfected, and then, gowns were donned. In portable radiography, the FPD is attached to



a) Back b) Side

Fig.10 How to wear the gown



a) Poor example b) Good example

Fig.11 Checkpoints when installing caps

the patient’s back. This requires bending over in cramped hospital rooms, raising both hands to adjust the position, and slipping between the cables of the equipment. The use of open-backed plastic aprons was avoided in favor of isolation gowns that provide good back protection. Care was taken to ensure that the back of the gown was firmly aligned, and a mirror was used to confirm that the back was not exposed after the gown was put on. Although some literature suggests tying the gown strings at the back, we chose to tie the strings at the sides of the body because if the back side of the gown is exposed, it potentially could directly touch the clean area without being noticed when removing the gown (Fig.10).

1-5-2 Cap Mounting

When putting on the cap, researchers decided to use a mirror to ensure that hair was not sticking out of the cap. Also, we ensured that the ears were covered by the cap (Fig.11).

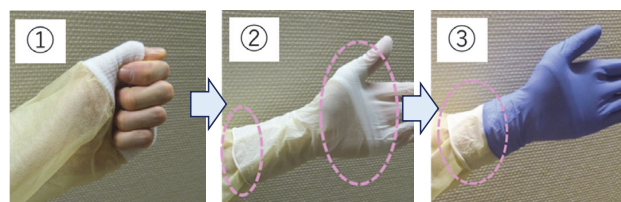


Fig.12 Procedure for fitting inner and outer gloves



a) How to bend the shield section b) When wearing eye protection mask c) When wearing goggles

Fig.13 Wearing an eye protection mask and goggles

1-5-3 Wearing gloves (inner and outer)

Gloves were worn over the sleeves of the gown, and subjects wore inner gloves of a type which allowed the grip of the sleeves with their fingers and covered the wrists tightly over the sleeves. For the outer gloves, different colors were selected, so that they could be distinguished from the inner gloves when the patients were undressing (Fig.12).

1-5-4 Eye Protection

An eye protection mask was worn to protect the eyes. Since it has become more difficult to secure supplies, arrangements were made so that personal goggles could be used in place of eye protection masks. The eye protection mask was utilized by bending both sides of the shield portion, and an eye protection mask was worn on top of the N95 mask (Fig.13).

1-6 Mobile X-ray Procedure

1-6-1 Patient Authentication

As part of the patient authentication procedure, Modality Worklist Management using barcode readers was performed in the clean area and deployed in the CS-7. To prevent contamination, the barcode readers were stored in



Fig.14 Barcode reader for patient authentication



a) FPD
b) CS-7
Fig.16 How to store FPD and CS-7



Fig.15 Curl cord suppression of exposure switches

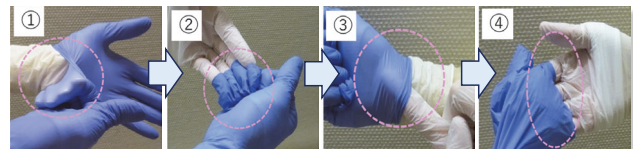


Fig.17 How to remove outer gloves

plastic bags were disposed of in an infectious waste container located in the contaminated area (Fig.16).

the clean area immediately after use (Fig.14).

1-6-2 Procedures from positioning to imaging

The portable device was moved to the contaminated area, and the plastic bag covered FPD was placed under the patient's back. The portable device was only allowed to contact the pre-designated area, its position was adjusted, and the imaging conditions were set appropriately (Fig.2). The hand switch cord was not extended, and it remained secured to the device to prevent contamination of the cord (Fig.15).

1-7 Procedures for removing PPE following imaging (in contaminated areas)

1-7-1 Storage of FPD and CS-7

After the imaging was completed, a 45 L plastic bag was removed from the outside of the FPD and temporarily stored in a clean area. In doing so, great care was taken, to ensure that the FPD was not contaminated.

Similarly, the standard bag No. 15 was removed from the outside of the CS-7, and only the CS-7 was stored in clean areas. The used

1-7-2 Outer gloves

Due to their contamination, outer gloves were discarded in the infectious waste container located in the contaminated area immediately after the FPD and CS-7 were stored. The outer gloves were removed with the inside of the gloves facing out so as not to contaminate the inner gloves, and the hand wearing the outer gloves was used to grip the removed gloves. To prevent contamination of the inner glove of the hand that removed the outer glove, the fingers were placed inside the outer glove on the opposite side and removed so that the inner side of the outer glove was facing out, as if covering the outer glove that was being held (Fig.17).

1-7-3 Equipment disinfection

After removing the outer gloves, the inner gloves were disinfected with alcohol, and then, the device was disinfected. The disinfection of the device was based on the disinfection of the entire device, with a focus on the previously determined points of contact (Fig.18). The gowns were donned and doffed before the temporary clean area was disinfected.



Fig.18 Equipment disinfection methods in contaminated areas



Fig.19 Isolation gown and inner glove removal procedure

1-7-4 Doffing gowns and inner gloves

After disinfection of the equipment, the inner gloves were disinfected. The isolation gown was untied, and the gown was peeled off by pulling the surface, so that the contaminated part of the surface was on the inside. The gown was removed slowly together with the inner gloves. The surfaces of the gowns and gloves were rolled up into a small ball so as not to touch them, and they were discarded in an infectious waste container in the contaminated area (Fig.19).

1-7-5 Removing eye protection mask and goggles

Hand sanitization was performed before removing the eye protection mask to protect the eyes. The mask was removed by holding the rubber part of the mask so as not to touch its surface, and then, it was discarded directly into the infectious waste container in the contaminated area. In case of shortage of supplies, personal goggles were used. The goggles were removed by holding the rubber part of the goggles, so as not to touch the surface of the goggles, and placed on the radiation-protection barrier of the equipment (Fig.20).



a) When using eye protection mask



b) When using goggles

Fig.20 How to remove eye protection mask and goggles



a) Goggle Disinfection b) Stored in goggle storage area c) Disinfecting impulse storage areas

Fig.21 Disinfection technique after goggle use

1-7-6 Goggles Disinfection

When goggles were used, an additional procedure for disinfecting the goggles had to be added. After putting on gloves, the goggles were disinfected and placed in the goggle storage area. During this process, the radiation-protection impulse was also contaminated, so researchers decided to disinfect it again (Fig.21).

1-7-7 Glove and cap removal

After disinfecting the gloves, they were removed. The removal was done so that the inside of the glove was on the outside, and the removed glove was held with the gloved hand. With the other hand, the glove was removed so that the inside of the glove was on the outside, and the glove being held was covered (the removed gloves were disposed of in an infectious waste container located in the contaminated area, and the procedure was the same as when the outer gloves were removed) (Fig.22).

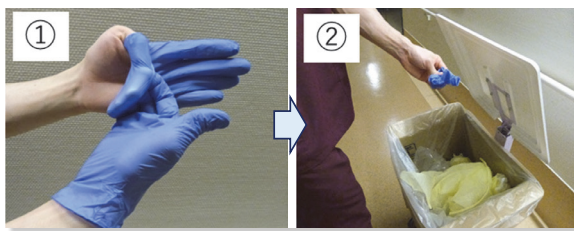


Fig.22 How to remove gloves

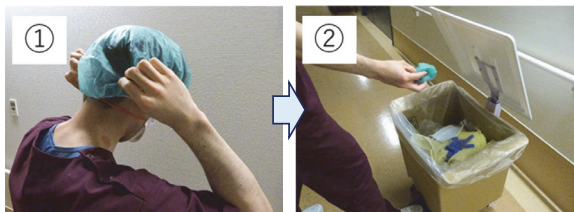


Fig.23 How to remove the cap



Fig.24 How to remove the N95 mask

Hand disinfection was performed before removal of the cap. Fingers were placed inside the cap so that the outside of the cap did not touch the hair or face, and the cap was removed and disposed of in an infectious waste container located in the contaminated area (Fig.23).

1-8 Disinfection of equipment (Responding within clean area)

After hand disinfection, the equipment was moved to a clean area. The equipment was moved to a location where space could be secured in advance, and disinfection was performed again. Although the basic policy was not to contaminate the temporary clean area, the area was disinfected again. Wearing gloves, the FPD, physical grid, CS-7, UF unit, and barcode reader were disinfected, and the exterior of the equipment was also disinfected again. Since the CS-7 exhibits a touch panel, researchers decided to disinfect the LCD surface with alcohol after shutting down the system. The

着	脱
①手指消毒	※迷ったら アルコール消毒を!
②アイソレーションガウン	①アウター手袋を外す
③N95マスク	②インナー手袋のアルコール消毒
④キャップ	③装置の消毒
⑤アイプロテクションマスク	④インナー手袋のアルコール消毒
⑥手袋2重 (インナー、アウター)	⑤ガウン、手袋を外す
	⑥手指消毒
	⑦アイプロテクションマスク
	⑧アルコール消毒
	⑨キャップ
	⑩N95マスク
	⑪アルコール消毒

Fig.25 Procedure notation

LCD screen can be disinfected by attaching a commercially available protective sheet to the screen, but due to the unavailability of this sheet, researchers decided not to spray alcohol directly onto the LCD surface. Instead, the surface was disinfected by spraying alcohol onto a soft gauze cleaning pad, using the pad to clean the LCD surface. In this case, sodium hypochlorite was not acceptable.

1-9 Removal of the N95 mask

Researchers decided not to remove the N95 mask in the dedicated COVID-19 ward. When removing the N95 mask, the rubber band under the mask was to be removed without touching the surface of the N95 mask, and then, the upper rubber band was to be removed without touching the surface and disposed of in the infection waste container (Fig.24).

1-10 Installation of simplified manuals

Simplified procedural documentation was posted on the mobile radiography equipment. By posting the simplified procedures, the radiology technician can perform the procedures with certainty and without hesitation (Fig.25).

1-11 Creation of a mobile radiography manual for COVID-19

The manual was revised three times to accommodate ever-changing circumstances and developments. A detailed manual was developed to disseminate procedures within the radiology department. The manual was distributed throughout the department using Microsoft Teams to avoid congestion and to prevent the spread of infection.

2. Results

The number of mobile X-ray imaging procedures for COVID-19 performed at the hospital from 21 January 2020 to 28 April 2020 are shown in Fig.26. There were 618 suspected COVID-19 cases with negative results, 67 suspected COVID-19 cases with positive results, and 739 positive confirmed COVID-19 cases (Table).

The hospital system was constantly changing, including an outpatient unit for patients with suspected COVID-19, a dedicated ward for COVID-19 patients, a COVID-19 intensive

care unit, a new infectious disease ward, an emergency room, and operating rooms.

Under these circumstances, the procedures were able to be confirmed, including the flow lines on each floor, as well as timely updates to the response manuals.

In mobile radiography, not only the donning and doffing of PPE, but also equipment operation and disinfection procedures can be complicated due to the large number of items used. Therefore, by posting simple procedures on the equipment, each on-site staff member could follow the COVID-19 infection-control procedures.

Among 50 radiology technologists within the radiology department as of May 15, 2020, the PCR test results showed a COVID-19 positivity rate of 0%.

In an environment where people cannot communicate with each other, Microsoft Teams delivery was immediate and could be viewed and checked at any time on portable devices, even in situations where procedures were required to be revised frequently.

Table COVID-19 Number of responded to cases

COVID-19 Suspicion (negative)	COVID-19 Suspicion (Positive)	COVID-19 (Positive)	COVID-19 Suspicion (Polymerase chain reaction: Waiting for results)	total
618	67	739	15	1439

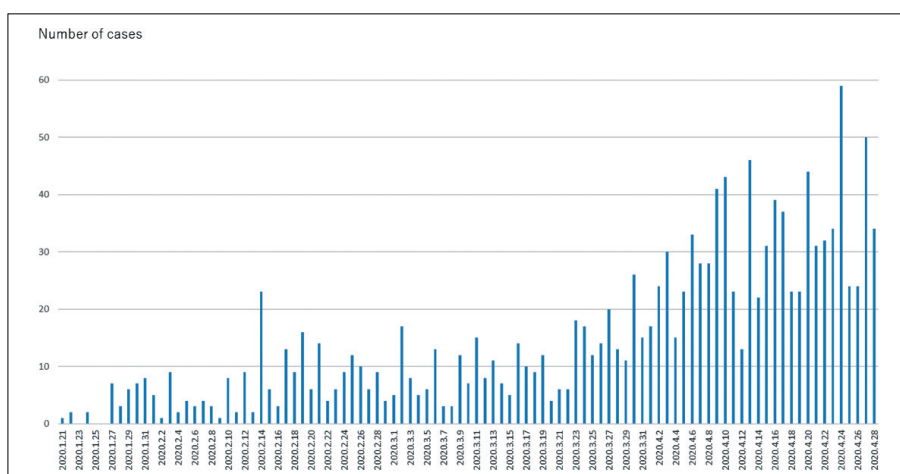


Fig.26 Number of mobile X-ray taken with COVID-19 at our hospital (from January 21, 2020 to April 28, 2020)

3. Consideration

The hospital involved in this study is a designated medical institution for specific infectious diseases and is well equipped to deal with new and unknown infectious diseases. In 2015, the hospital experienced a suspected case of Ebola hemorrhagic fever, so each staff member was well prepared for mobile radiography. However, the rapid increase in the number of patients made assigning the expected two radiologists per patient difficult. Additionally, the team was required to go through a trial-and-error process to address challenges, including the deployment of multiple mobile X-ray systems dedicated to COVID-19, systematic staffing issues, and coordination with each corresponding floor, such as when imaging outside the new infectious disease ward and when conducting emergency imaging to respond to rapid and severe cases of infection. As mentioned in the introduction, mobile radiography must be performed while operating not only the equipment but also various additional devices. Therefore, covering all devices with plastic bags (or similar) was necessary in order to sufficiently clear contact and droplet infection routes.

However, if plastic bags were installed to cover entire devices, the time required to set up the plastic bags and the increased risk of contact infection due to the bulkiness of the plastic bags had to be considered.

The examination time per patient in the COVID-19 environment was approximately 15 to 20 minutes, which is about three times longer than usual. Despite this additional challenge, we believed that the ability to identify contact infection sites and avoid the bulkiness of plastic bags, etc. as much as possible, rather than preparing to cover the equipment with plastic, etc., reduced the risk of infection.

Conversely, one problem with the protective clothing used in this study was that the neck area remained exposed. While the full PPE

used during the Ebola response protected the neck area, the PPE used during the current COVID-19 pandemic focused on preventing the pathogen SARS-CoV-2 from entering the body through contact with the mucous membranes of the eyes, nose, and mouth.

This resulted in potential limitations to the effectiveness of the procedures utilized. When beds were set relatively high, as in critical care wards, maintaining a sufficient distance from the patient was not possible when the FPD was placed on the patient's back. Therefore, the possibility of contamination of the unprotected neck cannot be ruled out.

Considering the possibility of a second or third wave occurring in the future, we believe considering measures to improve the protection of the neck area is necessary.

In order to reduce the complexity of the procedure for unknown contact and droplet infections, this hospital utilized a single device (Tirara-F) that integrated the console and device. However, the need to deploy several mobile devices dedicated to COVID-19 forced the use of a device composed of various components. Because of the complexity of the procedure, a sufficient risk of procedural violations existed, even if the procedures were written in the form of a manual. Therefore, posting simple procedures directly on the devices so that the procedures could be checked on the spot was considered more effective in preventing procedural errors and as a measure to prevent the spread of infection by each staff member.

However, if a dedicated general radiography system that takes into account the patient's line of flow could be introduced in the future, not only would image quality be improved, but the safe distance between the technician and the patient could be maintained, allowing the technician to image the patient more safely. Also, the risk of infection could be greatly reduced.

This hospital conducts PPE donning and doffing training under the guidance of the ICT and other infectious disease specialists, and al-



Fig.27 PPE Training for donning and doffing

though some procedures were different from what was expected due to COVID-19, the PPE donning and doffing went relatively smoothly thanks to the conducted training (Figure 27). Unfortunately, the training of how to share the mobile radiography procedures for COVID-19 could not be conducted as a group due to current national and local government outbreak prevention (cluster) requirements.

Under these circumstances, sharing procedures that corresponded to the ever-changing conditions in the department was necessary. Due to the limitations of using actual equipment, creating a procedure manual that was as detailed and easy to understand as possible for those parts that could not be explained using actual equipment was necessary. Microsoft Teams has been used since last year to share various information within the department, and the sharing of these procedure manuals through Teams has been very effective. Therefore, the expectation exists that Teams distribution will also be effective in sharing updates and new information, such as future improvements to the procedure manual.

4. Conclusion

The safety of healthcare workers must be guaranteed in order for the entire world to

work together to bring COVID-19 to an end. Mobile radiography requires various procedures from equipment handling to disinfection, in addition to donning and doffing of PPE. Mistakes in procedures not only increase the risk of infection among radiographers, but they can also lead to the spread of nosocomial infections.

The radiology department is a special medical service which cannot expect support from other medical professions. Therefore, the risk of infection to a single staff member in the radiology department is immeasurable, and this may lead to the illness of not only the individual radiographer, but also the shutdown of the entire radiology department, and may even make maintaining overall hospital functions difficult.

In this study, infection-control procedures for portable radiography, which were expected to exhibit a relatively high risk of infection among radiographic examinations, were examined. The results were shared in a manual within the department, which was considered effective in reducing individual infection risks and preventing nosocomial infections.

References

- 1) The Japanese Society of Environmental Infectious Diseases: A Guide for Responding to New Coronavirus Infections in Medical Institutions, 3rd Edition, May 7, 2020.

Portable chest X-ray examination procedures for COVID-19-positive patients: performance time necessary for radiological technologists

KOBAYASHI Tomoya, RT¹⁾, ISHIBASHI Tomomichi, RT²⁾, SOMEYA Satoka, RT²⁾, TASHIRO Kazuya, RT²⁾, ITO Yoshiyuki, RT²⁾, MIYAMOTO Katsumi, RT²⁾, YOKOKAWA Hiroshi, NS³⁾, SHIIGAI Masanari, MD⁴⁾, SHIOTANI Seiji, MD⁵⁾

1) Department of Radiological Sciences, Ibaraki Prefectural University of Health Science

2) Department of Radiological Technology, Tsukuba Medical Center Hospital

3) Department of Infection Control, Tsukuba Medical Center Hospital

4) Department of Radiology, Tsukuba Medical Center Hospital

5) Department of Radiology, Seirei Fuji Hospital

Note: This paper is secondary publication, the first paper was published in the JART, vol. 68 no. 824: 21-28, 2021.

Key words: corona virus disease 2019 (COVID-19), portable chest X-ray (CXR), examination time, infection prevention, personal protective equipment

[Abstract]

Purpose: To measure time needed to conduct portable chest X-ray (CXR) examinations for in-patients with the coronavirus disease 2019 (COVID-19) and to compare that for non-COVID-19 patients.

Material and Methods: Portable CXR examinations were conducted on three COVID-19-positive in-patients from March 1, 2020 to May 14, 2020 for follow-up evaluation of pneumonia by four radiological technologists with work experience of 2 to 14 years. As controls, data of five in-patients who had follow-up examinations of pneumonia in the same ward (from October 22, 2017 to February 29, 2020) but without COVID-19 infection were investigated. Times taken before and after portable CXR examination, as well as for the entire examination, were recorded in each case, and the mean times were calculated.

Results: Five portable CXR examinations of COVID-19-positive in-patients were done, consisting of two times each for two patients and once for one patient. Mean preparation time before portable CXR examination was 15.8 minutes, mean time spent after portable CXR examination was 28.3 minutes, and mean total examination time was 44.1 minutes. Whereas, in contrast, in the five portable CXR examinations for non-COVID-19 patients, mean preparation time was 2.5 minutes, mean time after portable CXR examinations was 9.4 minutes, and mean total examination time was 11.9 minutes.

Conclusion: Time spent for portable CXR examinations of COVID-19-positive patients was 3.7-fold greater than that of non-COVID-19 patients, due to infection prevention measures particularly after portable CXR examinations.

1. Introduction

A novel coronavirus, severe acute respiratory syndrome coronavirus 2 (SARS-CoV-2), was identified as the etiology for a cluster of pneumonia cases in Wuhan, a city in the Hubei Province of China¹⁾. It globally spread rapidly, and imaging features of patients with pneumonia induced by the coronavirus disease 2019 (COVID-19) were published^{2,3)}.

Fang et al. reported that sensitivity of un-enhanced computed tomography (CT) for detection of COVID-19 is higher than that of

real-time polymerase chain reaction (RT-PCR) test particularly when results of RT-PCR tests are negative⁴⁾. Also, radiography screening images can be used as an alternative to PCR examination, as they exhibit a higher sensitivity in some cases; even portable chest X-ray (CXR) examinations are effective in detecting the presence of pneumonia as well as for use in follow-up examinations after treatment for pneumonia^{4,5)}. Portable CXR examinations may be more useful and practical than CT for patients who are difficult to move from bed or room, especially in epidemic disease cases

such as COVID-19, due to a lower risk of spreading infection during an emergency referral, reducing the downtime for CT needed for other patients, and substantially reducing required numbers of personal protective equipment (PPE) per examination⁶⁻⁹.

When conducting portable CXR examinations especially in patients with COVID-19, radiological technologists (RTs) must undertake adequate infectious prevention measures, including PPE, to avoid spreading infection within the hospital and a potential collapse of the medical care system^{10,11}; therefore, infectious prevention measures for portable CXR examination are much more labor-intensive than for ordinary portable CXR situations. Zhao et al. reported their order of PPE fitting process as “putting on the 1st surgical cap, the respirator, the 2nd surgical cap, isolation gowns, the 1st surgical gloves, the 1st shoe covers, the protective glasses, the disposable gowns, the 2nd surgical gloves, the 2nd shoe covers, the surgical mask, and then checking for tightness of the outfit”; they also reported the entire PPE fitting time to be about 30 minutes for an RT¹². To our knowledge, there have been no reports quantitatively examining time taken for the entire process of portable CXR examination of COVID-19-positive patients from registration of the examination to completion of the examination. Herein we report our procedures for portable CXR examination of

in-patients at our institution, comparing those for COVID-19-positive and non-COVID-19 patients, to clarify the examination process and time necessitated for RTs.

2. Materials and Methods

2.1 Subjects:

Our subjects were three male in-patients with COVID-19-positive pneumonia (mean age: 64.3 years) who underwent follow-up examination using a portable CXR device from March 1, 2020 to May 14, 2020. Their symptoms ranged from mild to severe (Table 1). Portable CXR examination of the severe-symptom patient was done twice in supine position, and the other two patients were imaged twice and once, respectively, in a sitting-up position, for a total of 5 examinations. Control subjects were five in-patients with pneumonia without COVID-19 infection who underwent follow-up examinations using the same portable CXR unit in the same ward from August 1, 2019 to February 29, 2020 (Table 2). We excluded cases in which multiple sites were imaged for the same patient, or when multiple patients were imaged successively by the same RT. Our evaluation for the COVID-positive subjects and control subjects included portable CXR examinations by 9 RTs with working experience of from 2 to 17 years (mean 8.1 years) (Table 3). We measured time for each RT from their

Table 1 Clinical information of COVID-19-positive pneumonia patients

Case I.D.	Age (years)	Sex	Positioning at CXR	Severity of symptoms*	Number of CXR examinations during hospitalization
A	52	M	Supine position	Severe	2
B	80	M	Sitting-up position	Moderate	2
C	61	M	Sitting-up position	Mild	1

*Note: Definition of COVID-19 severity was as follows:

Severe: Necessitated extracorporeal membrane oxygenation (ECMO) and mechanical ventilation (ECMO was used only at the beginning, then removed)

Moderate: Having $SpO_2 \leq 93\%$

Mild: Having only fever

leaving the radiology department to returning to the department after completing a portable CXR examination.

This study was approved by the ethics committee of our institution (Approval No. 2020-009).

2.2 Specification of PPE and Disinfection of equipment:

The PPE in our institution includes 1) eye protection (face shield), 2) a filtering facepiece respirator (N95), 3) a surgical cap, 4) gloves, and 5) a fluid-resistant gown. Surface wiping disinfection was not necessary for the flat panel detector (FPD), portable X-ray unit, and its peripheral equipment, as those were dedicated solely for infected patients' use in the ward.

2.3 Scan parameters and protocols:

Portable CXR examinations (Portable X-ray unit: MobileArt Evolution, Shimadzu, Tokyo, Japan; FPD unit: CALNEO smart, Fujifilm Corp., Tokyo, Japan) were performed in the antero-posterior projection, and all were obtained by one RT using standard clinical acquisition parameters according to our institution's protocols. The layout map of the ward for infectious diseases is shown in Fig.1. Zoning was done in the ward for each COVID-19-positive patient, while the sites for wearing and removing the PPE and placement of the portable X-ray unit are fixed.

Examination procedures for COVID-19-positive patients are as follows:

- ① The RT registers reception of the patient using the Radiology Information Systems (RIS).

Table 2 Clinical information of non-COVID-19 patients

Case I.D.	Age (years)	Sex	Positioning at CXR	Reasons for hospitalization
D	91	M	Supine	Pneumonia
E	84	F	Sitting-up	Radius fracture
F	50	M	Sitting-up	Pelvic fracture
G	84	M	Sitting-up	Cervical fracture
H	91	M	Sitting-up	Pneumonia

Abbreviations: M = male, F = female

Table 3 Radiological technologists conducted portable CXR examination

I.D. number of Radiological technologist	Sex	Experience as a technologist (years)
I	M	14
II	F	2
III	M	4
IV	F	3
V	M	8
VI	F	3
VII	M	14
VIII	F	8
IX	F	17

- ②The RT confirms the patient’s body type and previous X-ray images on RIS or on electronic medical records.
- ③The RT moves from the radiology department to the infectious disease ward on the 3rd floor.
- ④The RT must put on specialized PPE at the specified location on the 3rd floor (“on” in Fig.1b) (Fig.2).
- ⑤The RT goes to the room where the portable X-ray unit is located (“Po” in Fig.1b).
- ⑥The RT goes to the ward with the portable X-ray unit where the patient is staying.
- ⑦The RT performs portable CXR examination.
- ⑧The RT transfers the image data to DICOM.
- ⑨The RT returns the portable X-ray unit to its usual location (“Po” in Fig.1b).
- ⑩The RT removes specialized PPE, and shoes must be disinfected at the specified location (“off” in Fig.1b) (Fig.3).
- ⑪The RT returns to the radiology department.
- ⑫The RT records the examination data on RIS.

RTs conducting imaging examinations for COVID-19-positive patients are required to record their own body temperature and health condition for two weeks after conducting a portable CXR examination of a suspected or COVID-19-positive patient. The possible route of an intra-hospital-acquired COVID-19 infection is quickly checked and evaluated for our hospital staff.

2.4 Time calculation:

Figure 4 shows portable CXR examination procedures from reception to completion of portable CXR examinations. Among them, time at reception (①), time at transfer the image data (⑧), and time at recording the data to RIS (⑫) could be confirmed from the Digital Imaging and Communications in Medicine (DICOM) data. Accordingly, time spent for each procedure was calculated by the following formula (Fig.4):

Time spent from the preparation to onset of

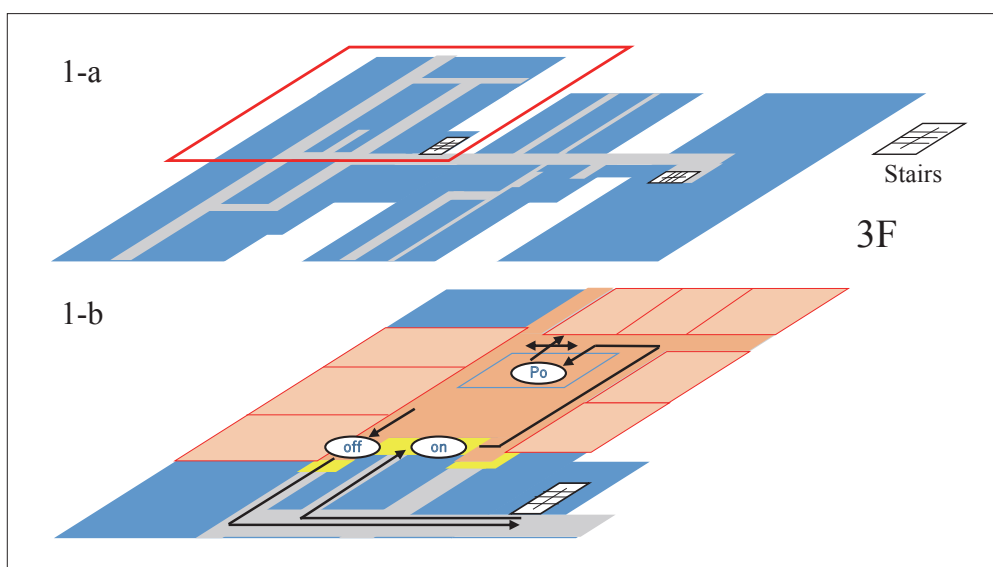


Fig.1 Locations of the specialized ward for infectious disease

1-a: Floor map of the third floor. Radiological technologists move from the radiology department on the first floor to the infectious disease-specialized ward on the third floor (outlined in red) going up the stairs for CXR examination of COVID-19-positive patients.
 1-b: Enlarged view of the infectious disease-specialized ward on the third floor (outlined in red in Fig.1a). Zoning is done for the infectious disease-specialized ward as shown in yellow (border portion), orange (ward floor hall), and pale orange (each ward room, outlined in red). Places are specified for the portable radiography unit (Po), putting PPE (on), and removing the PPE (off).

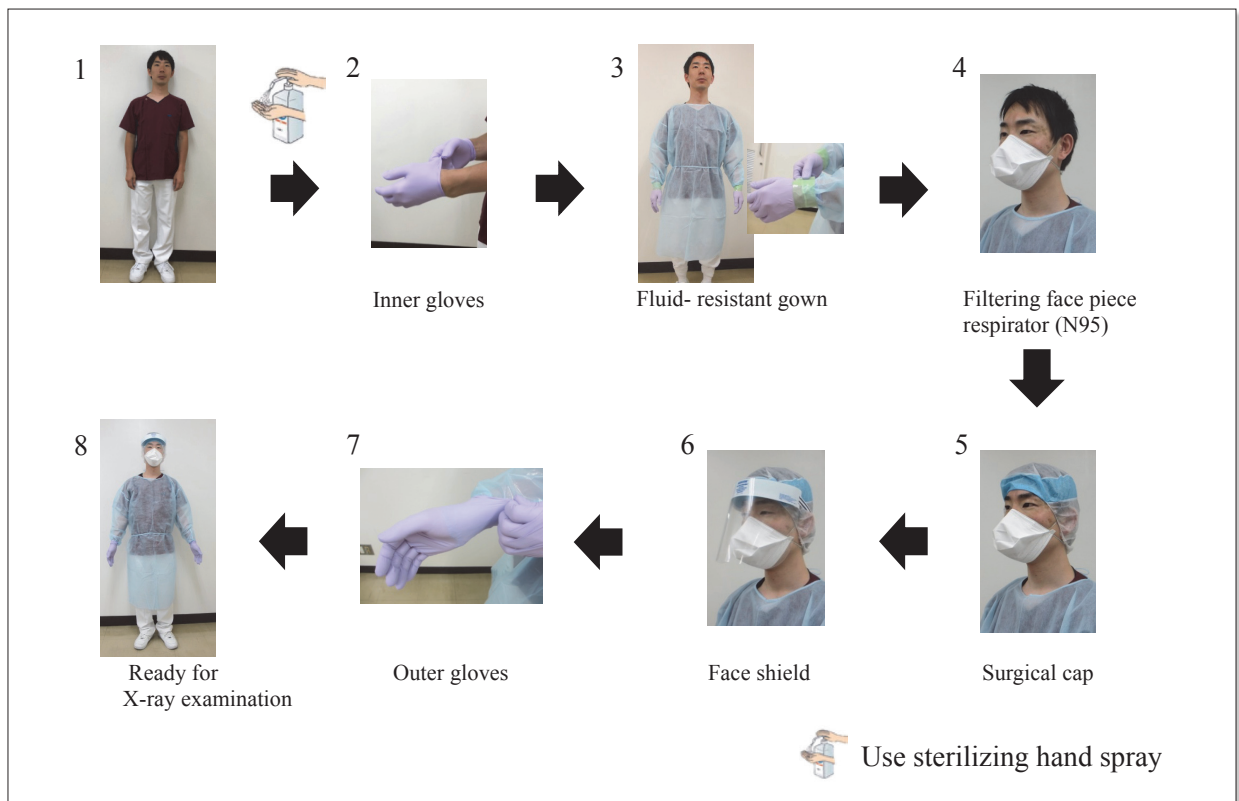


Fig.2 Process for wearing personal protective equipment (PPE)

PPE is put on starting with inner gloves, a fluid-resistant gown, a filtering facepiece respirator (N95), a surgical cap, a face shield, and outer gloves, in that order.

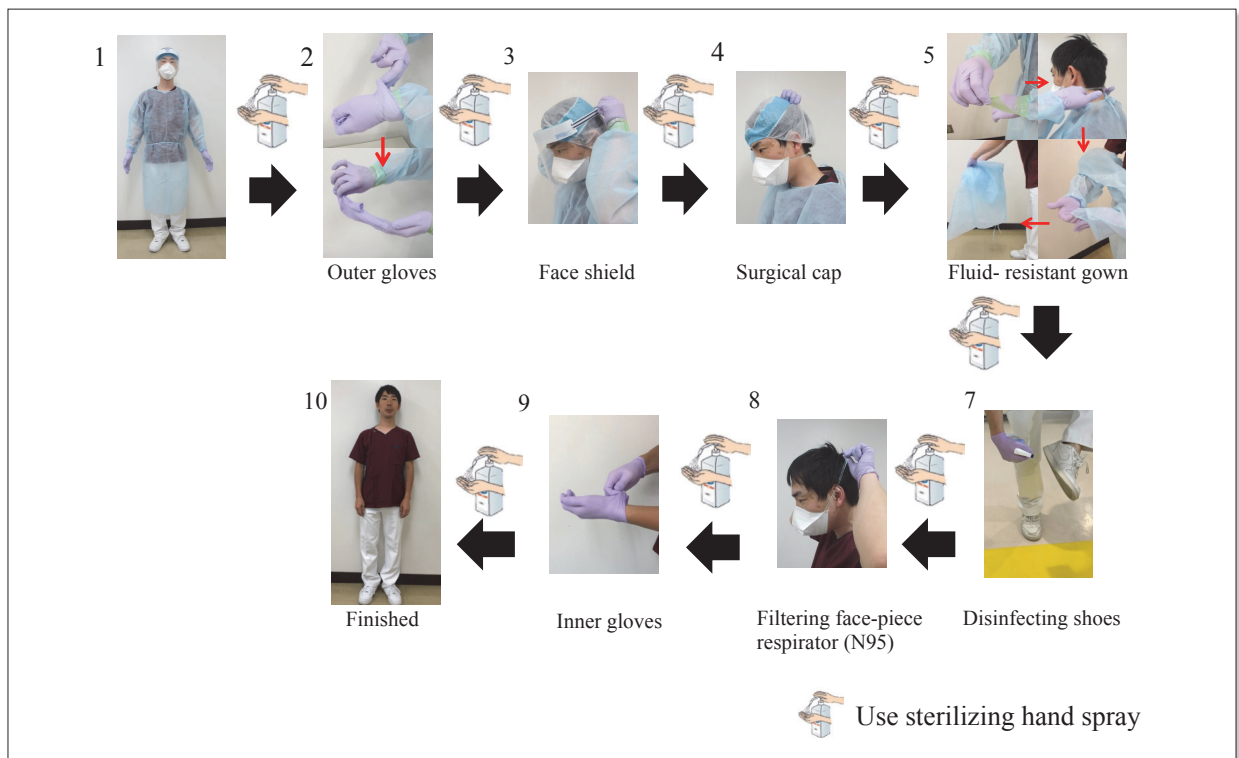


Fig.3 Process of removing personal protective equipment (PPE)

PPE is taken off starting with the outer gloves, the face shield, surgical cap, fluid-resistant gown; then, disinfecting of shoes, followed by removal of the filtering facepiece respirator (N95) and outer gloves, in that order. Radiological technologists should use sterilizing hand spray before each procedure step.

portable CXR examination (Preparation time) = ⑧-①.

Time spent after completion of portable CXR examination (Time after portable CXR) = ⑫-⑧.

Entire time from the reception to completion of portable CXR examination (Total examination time) = ⑫-①.

2.5 Statistical analysis:

Preparation time, time after portable CXR, and total examination time were measured for each portable CXR examination, and all data were shown as mean.

3. Results

COVID-19-positive patients had a total of five portable CXR examinations, including two times for two patients and one time for one patient by RT ID No. I, II, II, and IV (Table 3). Mean preparation time was 15.8 minutes, mean time after portable CXR examination was 28.3 minutes, and mean total examination time was 44.1 minutes (Table 4).

By comparison, the five portable CXR examinations for five patients without COVID-19 infection were conducted by RT ID No. V to IV (Table 3). Mean preparation time was 2.5 minutes, mean time after portable CXR exami-

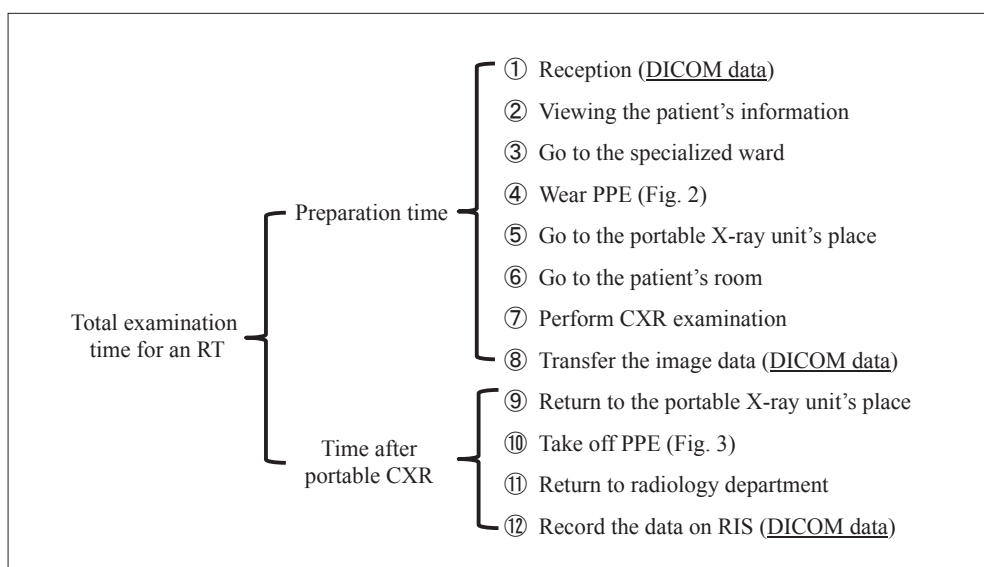


Fig.4 Portable CXR examination procedures

Note: ①, ⑧, and ⑫ were automatically recorded as DICOM data. Therefore, we could define ⑧-① =Preparation time, ⑫-⑧ =Time after CXR, and ⑫-① =Total examination time.

Table 4 Time spent regarding portable chest X-ray (CXR) examination in COVID-19-positive patients

Examination order number	Case ID	ID of Radiological technologist	Preparation time (minutes)	Time after CXR (minutes)	Total examination time (minutes)
1	A	I	11.0	32.1	43.1
2	A	II	18.2	25.3	43.5
3	B	III	17.8	27.0	44.8
4	C	III	13.0	31.7	44.7
5	B	IV	18.8	25.6	44.4
Mean			15.8	28.3	44.1

Table 5 Time spent regarding portable chest X-ray (CXR) examination in non-COVID-19 patients

Examination order number	Case ID	ID of Radiological technologist	Preparation time (minutes)	Time after CXR (minutes)	Total examination time (minutes)
6	D	V	4.0	8.7	12.7
7	E	VI	1.6	8.6	10.2
8	F	VII	3.5	9.5	13.0
9	G	VIII	1.2	8.8	10.0
10	H	IX	2.3	11.4	13.7
Mean			2.5	9.4	11.9

nation was 9.4 minutes, and mean total examination time was 11.9 minutes (Table 5).

As of May 31, 2020, the five RTs had no COVID-19 symptoms, had been tested as COVID-19-negative, and there had been no hospital-acquired COVID-19 infection cases in our institution.

4. Discussion

In this study, mean total examination time for non-COVID-19 patients was 11.9 minutes and that for COVID-19-positive patients was 44.1 minutes, a 3.7-fold greater time for the COVID-19-positive cases. This is mainly attributable to time spent for prevention of infection (namely, putting on and taking off the specialized PPE). In COVID-19-positive cases, the mean time after portable CXR examination (28.3 minutes) was much longer than the mean preparation time (15.8 minutes) due to the need for carefully disinfecting the hands after removing each PPE item. Zhao et al. reported fitting time of PPE was about 30 minutes, probably due to a greater number of procedural steps than ours and their higher stage of infection prevention level¹²⁾.

SARS-CoV-2 remains detectable in aerosols for up to 3 hours, up to 24 hours on cardboard, and up to 2-3 days on plastic and stainless steel¹³⁾. RTs are among the first-line health care workers who might be exposed to COVID-19; thus, sufficient preventive measures should be taken to avoid infection. There have been

no COVID-19-infected RTs or other staff at our institution, indicating that the measures for COVID-19 prevention have been effective. Since the portable CXR unit used in our institution is dedicated solely for use in the infectious disease ward and zoning is done for patients within that ward, time spent disinfecting the portable CXR unit is substantially less, contributing to a shorter overall examination time while preventing hospital-acquired infection.

Our study has several limitations. The first limitation is the small number of our study subjects, insufficient for statistical verification of possible effects of the environmental factors. The second limitation is that performing time (6–7) was including in the preparation time in our study, because time to perform portable CXR examination was not recorded as DICOM data. The X-ray examination time differs depending on the pathological condition of each patient. Portable CXR examination time for patients with very severe COVID-19 symptoms is considered to be longer than that for our study subjects. Therefore, further study including very severe symptom cases is necessary. The third limitation is the lack of inclusion of cases in which one RT conducted several portable CXR examinations sequentially, although one RT did perform two examinations in our study. An greater number of portable CXR examinations by each RT may subsequently reduce the entire examination time, due to more experience, skill, and improved technique at putting on and removing PPE. The fourth limitation is

that the RTs were different for COVID-19-positive and non-COVID-19 patients; therefore, the time spent to conduct a portable CXR examination could not be easily compared for inter-operator variation. Further time measurement studies with the same RT members on COVID-19-positive and non-COVID-19 patients are necessary to eliminate such a bias.

5. Conclusion

From our findings on the entire procedure and time spent for each portable CXR examination for COVID-19-positive patients in our institution, a 3.7-fold increase in time was needed compared with that for non-COVID-19 patients due to infection prevention measures, particularly after a portable CXR examination, requiring a mean total of 44.1 minutes per case.

Acknowledgement: The authors thank Ms. Yumiko Moriyama for her help with manuscript preparation.

Compliance with ethical standards

Conflict of interest: The authors declare that they have no conflict of interest regarding the present study.

Ethical approval: The present study was approved by the ethics committee of our institution (Approval No. 2020-009).

Informed consent: Informed consent was obtained from all RTs included in the study.

References

- 1) Wang D, et al.: Clinical characteristics of 138 hospitalized patients with 2019 novel coronavirus-infected pneumonia in Wuhan, China. *JAMA*, 323(11), 1061-1069, 2020.
- 2) Pan Y, et al.: Initial CT findings and temporal changes in patients with the novel corona-virus pneumonia (2019-nCoV): a study of 63 patients in Wuhan, China. *Eur Radiol*, 1-4, 2020.
- 3) Pan F, et al.: Time course of lung changes on chest CT during recovery from 2019 novel coronavirus (COVID-19) pneumonia. *Radiology*, 295, 715-721, 2020.
- 4) Fang Y, et al.: Sensitivity of chest CT for COVID-19: comparison to RT-PCR. *Radiology*, 296(2), E115-E117, 2020.
- 5) Wong HYF, et al.: Frequency and distribution of chest radiographic findings in COVID-19 positive patients. *Radiology*, 296(2), E72-E78, 2020.
- 6) Ai T, et al.: Correlation of Chest CT and RT-PCR Testing in Coronavirus Disease 2019 (COVID-19) in China: A Report of 1014 Cases. *Radiology*, 296(2), E32-E40, 2020.
- 7) Rubin GD, et al.: The Role of Chest Imaging in Patient Management during the COVID-19 Pandemic: A Multinational Consensus Statement from the Fleischner Society. *Radiology*, 296(1), 172-180, 2020.
- 8) American College of Radiology: ACR Recommendations for the use of Chest Radiography and Computed Tomography (CT) for Suspected COVID-19 Infection. Accessed 1st Apr 2020. <https://www.acr.org/Advocacy-and-Economics/ACR-Position-Statements/Recommendations-for-Chest-Radiography-and-CT-for-Suspected-COVID19-Infection>
- 9) Kooraki S, et al.: Coronavirus (COVID-19) outbreak: What the Department of Radiology should know. *J. Am. Coll. Radio*, 17, 447-451, 2020.
- 10) Wang J, et al.: Exploring the reasons for healthcare workers infected with novel coronavirus disease 2019 (COVID-19) in China. *J Hosp Infect*, 105(1), 100-101, 2020.
- 11) Cavallo JJ, et al.: Hospital capacity and operations in the coronavirus disease 2019 (COVID-19) pandemic: planning for the Nth patient. *JAMA Health Forum*, 1(3): e200345, 2020.
- 12) Zhao Y, et al.: Radiology department strategies to protect Radiologic Technologists against COVID19: experience from Wuhan. *Eur J Radiol*, 108996, 2020.
- 13) Van Doremalen N, et al.: Aerosol and surface stability of SARS-CoV-2 as compared with SARS-CoV-1. *N Engl J Med*, 382(16), 1564-1567, 2020.

Regulations and Requirements for Submissions to the Journal of the Japan Association of Radiological Technologists

Submission Regulations

Revised: April 1, 2013
October 30, 2013
February 20, 2016
April 20, 2019
October 3, 2020

Objective

Article 1. These regulations are based on the operations defined in Article 4 of the articles on the incorporation of the Japan Association of Radiological Technologists (hereafter “the Association”). They stipulate the criteria for submissions to the Journal and informational magazines published by the Association (hereafter “the Journal, etc.”).

Eligibility

Article 2. Only members of the Association may submit to the Journal, etc., unless the author is not a radiographer, in which case this condition does not apply.

Copyright

Article 3. The copyright of the published manuscript is based on rules regarding the management of the works of the Society.

Obligations

Article 4.

- 4-1. The topic of submitted manuscripts must belong to a relevant domain to technologies for prevention, diagnosis, and treatment related to radiation therapy, and manuscripts must be unpublished.
- 4-2. Submitted papers, whether for fundamental or applied research, must sufficiently consider bioethics, and authors must bear the ultimate responsibility for their content.
- 4-3. Fabrication, forgery, plagiarism, violation of the law, and other forms of wrongdoing are not allowed in submissions.
- 4-4. If the author has already reported similar content to that of the published manuscript or submitted it to another journal, the author is required to explain the difference from the manuscript in a separate document.
- 4-5. The author must disclose all information regarding conflicts of interest.
- 4-6. The author shall be held accountable for any misconduct regarding the content of the publication, and the Society shall not be involved at all.

Submissions

Article 5. The types of accepted submissions are categorized as follows:

- (1) Original articles
Highly original research papers with clear objectives and conclusions.
- (2) Review articles
Articles systematically summarizing a specific research domain from a particular perspective.
- (3) Rapid communications
Reports of original research that must be published rapidly.
- (4) Reports
Surveys of significance to the study of radiological technology or reports of interesting and important cases.
- (5) Notes
Articles on the development or evaluation of new equipment, techniques, products, etc.
- (6) Technical material
Compilations of survey data or technical aspects, or anything that can serve as a reference for research and technology.
- (7) Overview articles
A compilation of technologies, principles, or basic elements with reference to the literature. However, what was explained in the development and use of equipment and software constitutes a technical explanation.
- (8) Miscellaneous
Other items approved by the editorial committee for publication, such as lecture transcripts, courses published as journal articles, and newspaper/magazine articles that were not published in Issues 1–7.

How to submit

Article 6.

- 6-1. Use the online posting system.
- 6-2. The author shall save the duplicate data of the submitted manuscript until the publication decision.

Formatting

Article 7. The explanation of the manuscript shall be provided according to the submission procedure specified separately.

Reception of submissions

Article 8. The reception date shall be the date on which the editorial board has determined to comply with this regulation.

Review

Article 9.

- 9-1. Received manuscripts will be reviewed carefully and impartially by peer-reviewers selected by the editorial committee.
- 9-2. Peer reviews are limited to two times. However, in the case of Article 5, items 7 and 8, in principle, peer review is not performed.
- 9-3. The acceptance or rejection of the manuscript will be decided by the editorial committee in consideration of the opinions of the reviewers, and the date will be the final acceptance date.

Corrections

Article 10.

- 10-1. In principle, the author must proofread the manuscript up to twice and return it by the designated date. If the deadline is breached, the school will be completed with the proofreading of the editorial board.
- 10-2. The correction of words and plates that were not included in the manuscript is not allowed.

Printing

Article 11.

- 11-1. 20 copies of the papers published in the Journal, etc., will be presented to their authors as an offprint.
- 11-2. The authors must bear the expenses of any additional offprints. If additional offprints are required, they must be requested by the time corrections are submitted.

Revision or repeal of regulations

Article 12.

- 12-1. This regulation will come into effect on April 1, 2012.
- 12-2. This regulation will come into effect on April 1, 2016.
- 12-3. This regulation will come into effect on April 20, 2019.
- 12-4. This regulation will come into effect on October 3, 2020.

Requirements for Submissions to the Journal of the Japan Association of Radiological Technologists

Revised: February 20, 2016
April 20, 2019
October 3, 2020

The formatting requirements for manuscripts specified in Article 7 of the submission regulations of the Journal of the Japan Association of Radiological Technologists are as follows:

1. How to write original articles, reviews, breaking news, reports, notes, materials, and explanations.
 - 1) Title and abstract
Enter the following items in the online posting system.
 - ① Enter the author's name, facility name, affiliation, occupation, and contact information, and select the specialized field.
 - ② Select the type of post.
 - ③ Enter the title and co-author information in Japanese and English. Co-authors are limited to members of the Society. However, this does not apply if the co-author is not a radiological technologist.
 - ④ Summarize the abstract in Japanese and English within 300 characters (words).
 - ⑤ Enter the keywords in English. Keywords should be in noun forms and should be limited to five.
 - 2) Text and figures/tables
For the text and figures/tables, create and post both a separate file and a file containing figures and tables within the text.
 - ① The manuscript should be written in Japanese or English.
Create the manuscript using Word with a paper size set to the A4 size. The type and size of the fonts should be 12 points for both Japanese and English fonts, Mincho font, and Times. The line spacing should be 18 points. Leave a margin of 2 cm or more on the top, bottom, left, and right.
 - ② The specified number of pages and excess page costs of the manuscript are as shown in the following table.

Type of submission	Number of pages (as published)	Fee for additional pages
Original articles	8	¥10,000 per page
Review articles	8	
Rapid communications	3	
Reports	3	
Notes	8	
Technical material	8	
Overview articles	8	
Technical overview articles	4–6	None
Miscellaneous	2 (strictly enforced)	

- ③As a general rule, academic terms should conform to Cabinet Notification No. 2 and JIS.
- ④The unit of quantity is the International System of Units (SI).
- ⑤Indicate the insertion position of the figure/table in red in the text created as a separate file from the figure/table.
- ⑥The figures and tables created as separate files from the main text are of higher resolution and can be subjected to secondary processing in production.
- ⑦For academic treatises, write the title and characters in the table in English.
- ⑧When reprinting figures/tables, specify the source and obtain permission.
- ⑨Attach the explanation of the figures and tables in Japanese in a separate file.

3) References

References should be listed in the order in which they appear, with the numbers in parentheses at the end of the referenced text.

The notation format is as follows.

①For magazines

Author names: Title (article title) Magazine name (abbreviation), volume, first-last page, year of publication.

②For a book

Author names: Book title, First-last page, publisher, year of publication.

③If there are two or more authors, enter only the first author and enter “other” and “et al.”

4) Trademark name

If a trademark name is required, write the trademark name in both parentheses after the common name and add ®.

2. Submission of copyright transfer agreement

- (1) The first author and co-authors must agree with the contents of the copyright transfer agreement stipulated in the copyright management regulations.
- (2) The copyright transfer agreement shall be stipulated by the rules regarding copyright management, and the format specified on the Society’s website should be used.
- (3) The copyright transfer agreement must be signed by the first author and co-authors, and provided when the manuscript is submitted.

3. About secondary publication

- (1) Obtain approval from the editorial departments of both the first and second journals.
- (2) The period until the secondary publication should be decided through discussions between the editorial departments of both parties and the author.
- (3) Secondary publications of treatises are intended for different types of readerships.
- (4) The secondary publication of a treatise should faithfully reflect the content of the first treatise.
- (5) Specify the source of the original treatise.
- (6) Specify in the title that it is a secondary publication.

4. About technical commentary requested by the editorial board.

The composition of the text is as follows (1) to (9).

- (1) Abstract (100-150 words in Japanese and English)
- (2) Keywords (3 words)
- (3) Introduction:
- (4) Purpose of explanation (overview)
- (5) Main paper
- (6) Comparison and consideration with previous research (development technology)
- (7) Clinical usefulness
- (8) Conclusion
- (9) References

Journal of JART
-English edition 2022-

June 1, 2022

Issuer: Ueda Katsuhiko

Publisher: The Japan Association of Radiological Technologists

22F Mita Kokusai Building. 1-4-28,

Mita, Minato-ku, Tokyo. 108-0073

TEL: +81-3-4226-2211 FAX: +81-50-3153-1519

<http://www.jart.jp>

• Published by The Japan Association of Radiological Technologists
©2022, Printed in Japan.



The Japan Association of Radiological Technologists
<http://www.jart.jp>